Laboratory Modelling of Volcano Plumbing Systems: A Review

Olivier Galland, Eoghan Holohan,
Benjamin van Wyk de Vries and Steffi Burchardt

Abstract

We review the numerous experimental studies dedicated to unravelling the physics and dynamics of various parts of a volcanic plumbing system. Section 1 lists the model materials commonly used for model magmas or model rocks. We describe these materials' mechanical properties and discuss their suitability for modelling sub-volcanic processes. Section 2 examines the fundamental concepts of dimensional analysis and similarity in laboratory modelling. We provide a step-by-step explanation of how to apply dimensional analysis to laboratory models in order to identify fundamental physical laws that govern the modelled processes in dimensionless (i.e. scale independent) form. Section 3 summarises and discusses the past applications of laboratory models to understand numerous features of volcanic plumbing systems. These include: dykes, cone sheets, sills, laccoliths, caldera-related structures, ground deformation, magma/fault interactions, and explosive vents. We outline how laboratory models have yielded insights into the main geometric and mechanical controls on the development of each part of the volcanic

O. Galland (✉)
Physics of Geological Processes (PGP), Department of Geosciences, University of Oslo, Oslo, Norway
e-mail: olivier.galland@fys.uio.no

E. Holohan
German Research Centre for Geosciences (GFZ), Helmholtz Zentrum Potsdam, Potsdam, Germany

B. van Wyk de Vries
Observatoire de Physique du Globe de Clermont-Ferrand, Blaise Pascal University, Clermont-Ferrand, France

S. Burchardt
Department of Earth Sciences, Center for Experimental Mineralogy, Petrology and Geochemistry, University of Uppsala, Uppsala, Sweden

Advs in Volcanology (2018) 147–214
DOI 10.1007/11157_2015_9

Published Online: 13 July 2015

plumbing system. We conclude with some perspectives on the limitations of past and current analogue modelling approaches, and on challenges to be addressed by future research.

1 Introduction

Volcanic plumbing systems set the stage for volcanic eruptions, by controlling the flow of magma into the vent. The term 'volcano plumbing system' is here broadly defined as the structural framework of pathways and storage regions through which magma travels on its journey from its source region to the Earth's surface. As the metaphor of a plumbing system suggests, the focus here is primarily on the transport and storage of magma within relatively solid or brittle Earth materials that characterise the upper part of the Earth's lithosphere.

The huge scale ranges that characterise volcano plumbing systems represent a challenge for unravelling the complexity of underlying processes. These processes act at length scales of microns to thousands of kilometres, and over time scales of milliseconds to millions of years. Our observational range is limited, e.g. to the human life (and working) time and the geological processes are often hidden under ground (Fig. 1). Earth scientists try to overcome these obstacles by studying geological systems as observed in the field. However, field examples are commonly the compound result of a series of past and/or on-going geological events and processes. This aggregation of effects can make it difficult to grasp clearly the roles of individual physical processes in the geological system's evolution as a whole.

One way to tackle these obstacles is to replicate geological processes in controlled laboratory experiments. Hall (1815) conducted one of the first such experiments to provide a qualitative physical explanation (horizontal shortening) for folded rock strata observed in Scotland. By designing experiments to study the formation of

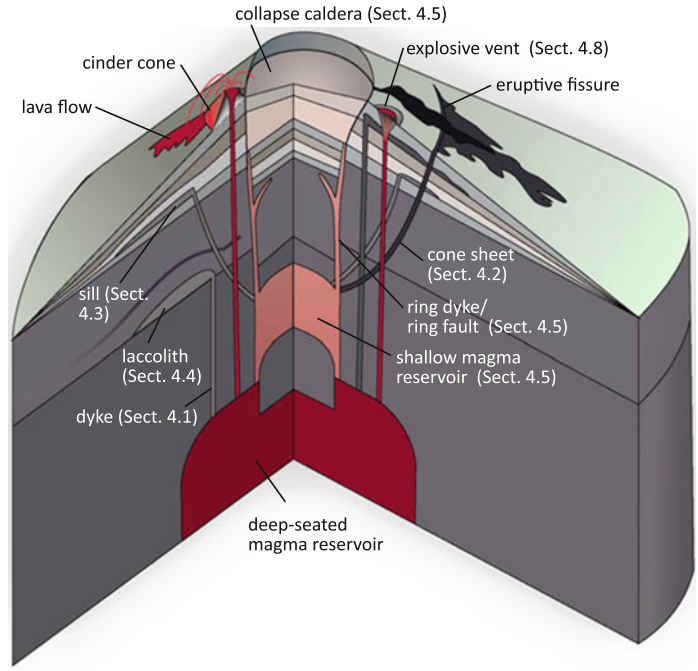

Fig. 1 Schematic drawing illustrating the main characteristics of volcano plumbing systems. These include dykes (Sect. 4.1), cone sheets (Sect. 4.2), sills (Sect. 4.3), laccoliths (Sect. 4.4), caldera-related structures and intrusions (Sect. 4.5), magma-fault interactions (Sect. 4.7), and explosive volcanic vents (Sect. 4.8). See text for details

diatremes, Daubrée (1891) first simulated processes underlying the development of volcano plumbing systems. Since then, laboratory models have been a key tool for scientists seeking to unravel the physical processes that control the development and behaviour of volcanic and magmatic systems (Fig. 2).

In this chapter, we provide a review of how laboratory models, also called analogue models, have been designed and adapted to unravel the dynamics of shallow magmatic systems. We also describe and discuss the application of the laboratory results to various features and stages in these systems' evolution. As with other disciplines in Earth Sciences, laboratory modelling has evolved to become increasingly quantitative in recent years. As we highlight below, this has drastically increased the capacity of analogue models to aid the interpretation of not only intrusive and structural relationships in 'fossilised' field examples, but also geodetic and geophysical data from active volcanoes.

2 Model Materials

An important technical aspect of laboratory models of volcanic plumbing systems is a relevant choice of model materials. Before starting an experimental project, it is very important to know exactly the mechanical properties of the model materials to be used. This step is crucial for: (i) designing the experimental apparatus, (ii) setting the initial and boundary conditions of the models, and (iii) quantitatively interpreting the model results. A wide range of materials with known mechanical properties is available from the literature, both for model magmas and model host rocks (Figs. 3 and 4; Tables 1, 2, 3 and 4).

2.1 Model Magma

In nature, magma viscosity depends on many factors, such as chemical composition, temperature, dissolved volatile content (e.g. water), and total crystal content. Magma viscosity hence has a wide range, within which a lowest viscosity end member would be a high temperature, crystal-poor, 'wet' mafic magma ($\eta \sim$ 10–100 Pa s) (Dingwell et al. 1993), and a highest viscosity end member be a low-temperature, crystal-rich, 'dry' granite magma (η up to 10^{17-18} Pa s) (Scaillet et al. 1997). Such wide range means that different materials are required to simulate magmas of high or low viscosity (Table 2).

2.1.1 "High" Viscosity Magma

The most commonly used material for simulating high viscosity magma is a silicone polymer or putty called Polydimethylsiloxane (PDMS; Figs. 3 and 4a). The advantage of PDMS is that it is a Newtonian fluid at typical laboratory strain rates and temperatures (Weijermars 1986; ten Grotenhuis et al. 2002; Boutelier et al. 2008). This means that the relationship of the applied shear stress to resultant shear strain rate follows a power law of exponent of 1 (i.e. is linea). Its viscosity is hence a constant at a given temperature and has been measured at $\sim 1–3 \times 10^4$ Pa s at room temperature (Table 2; e.g. Weijermars 1986; Corti et al. 2005). As temperature varies, the viscosity of PDMS follows an Arrhenius law (Hailemariam and Mulugeta 1998; Cagnard et al. 2006), i.e., it decreases exponentially with increasing temperature. The viscosity of PDMS can be easily measured by using a cylindrical viscometer, as described by e.g. Cobbold and Jackson (1992) and Reber et al. (2013), or a capillary (extrusion) viscometer, as described by e.g. Hailemariam and Mulugeta (1998).

According to experimental requirements, the viscosity of PDMS can also be increased or decreased by the addition of other materials. Increasing PDMS viscosity is achieved by mixing it with different proportions of small mineral particles (inert fillers). The resulting mixture is a suspension of particles within a viscous matrix, the viscosity of which follows the Einstein-Roscoe law (Einstein 1906; Weijermars 1986). Depending on the specific gravity of the particles used, the bulk density of such a mixture can be increased or decreased with respect to pure PDMS. For example, addition of $BaSO_4$ increases the bulk density (ten Grotenhuis et al. 2002), whereas addition of fine hollow glass

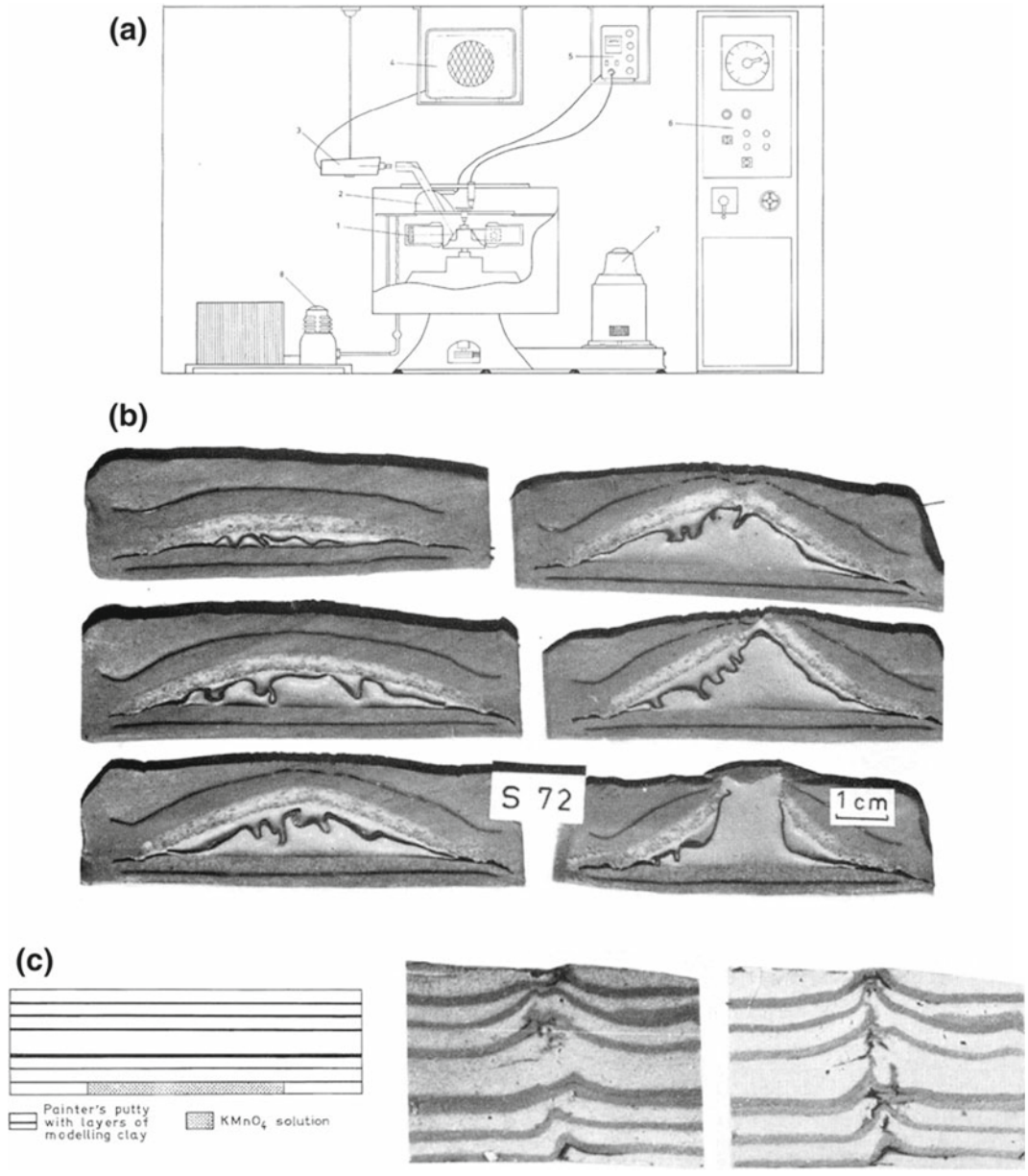

Fig. 2 **a** Drawing of the pioneering experimental apparatus designed by Hans Ramberg, at the University of Uppsala, Sweden. *1* model in centrifuge cup; *2* stroboscopic light reflector; *3* TV camera; *4* TV receiver; *5* stroboscope; *6* temperature and speed control cabinet; *7* motor; *8* refrigerator unit. **b** Sections through Ramberg's centrifuged model of silicone putty with powdered-wax layer above, embedded in painter's putty with sheets of modelling clay. Run 10 min at 1300 g, the experiment was intended to model diapir rise. Nevertheless, the similarity between the model outcome and igneous laccoliths suggests that such models can be applied to these igneous features. **c** Ramberg's model of magma rise due to buoyant forces. *Left* Initial arrangement of model. *Centre* and *right* Cross-sections through vent of a $KMnO_4$ solution through overburden in model shown in left. The vent runs vertically from one edge of the collapsed original "magma" chamber. Run less than 1 min at some 1000 g. After Ramberg (1967)

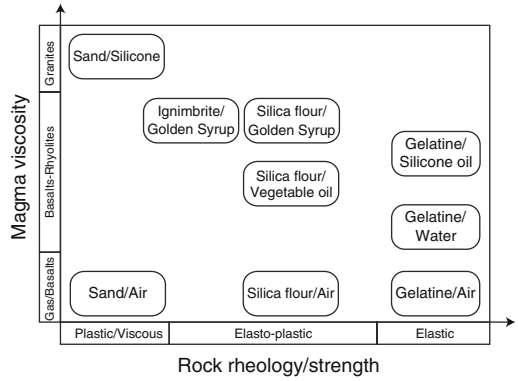

Fig. 3 Qualitative diagram representing the mechanical properties of the main model materials that have been used in laboratory models of volcano plumbing systems (see Tables 1, 2, 3 and 4). Note that for model rocks, the elastic, elasto-plastic and viscous/plastic rheologies correspond to the dominant behaviours of the corresponding model materials. See Sect. 2.2 for explanations

beads (Boutelier et al. 2008) decreases it. For large contents of inert fillers, however, the mixture becomes non-Newtonian and its stress to strain relationship may instead follow a power law with an exponent greater than 1. At very large contents of fillers, the mixture may become visco-elastic (i.e. display substantial elastic or recoverable strains). Decreasing the viscosity of PDMS is achieved by mixing it with oleic acid, such as described by e.g. Corti et al. (2005) and Reber et al. (2013), although the PDMS-oleic acid mixture becomes sticky and challenging to handle. These two procedures provide an enlarged analogue magma viscosity range of between $\sim 7 \times 10^3$ and $\sim 5 \times 10^5$ Pa s, i.e. almost two orders of magnitude.

In addition, the commonly-used stiff PDMS putty is an end member of a suite of silicone oil products of variable, controlled viscosities (Takada 1990, 1994b; de Bremond d'Ars et al. 2001; Watanabe et al. 2002). Those used by these authors range between 0.8×10^{-3} and 1.337 Pa s, but products with a still-broader viscosity range are available on the market. Given their wide range of viscosities, silicone oils can hence be used to simulate both high viscosity and low viscosity magmas without the need for adding other materials (cf. Table 2).

2.1.2 "Low" Viscosity Magma

During the last two decades, several experimental techniques have been developed to simulate low-viscosity magmas. The simplest model magma is water; it has been mostly used for simulating dyke and sill emplacement in gelatine (Tables 1 and 2; Hyndman and Alt 1987; McLeod and Tait 1999; Menand and Tait 2002; Walter and Troll 2003; Kavanagh et al. 2006; Menand 2008; Kervyn et al. 2009; Le Corvec et al. 2013). Water is an incompressible Newton fluid of viscosity $\sim 10^{-3}$ Pa s. It is often dyed, such that an intruding dyke can be optically tracked through models made of transparent gelatine. In these models, the density of the intruding water is very similar to that of the hosting gelatine. Consequently, an internal fluid pressure imposed by the experimentalist is required to trigger the propagation of the neutrally buoyant intrusion.

To study buoyancy-driven fracturing, air is used as the intruding fluid (Table 2; Figs. 3 and 4d–e). Air has a density of 1.2×10^{-3} kg m^{-3} and a viscosity of $\sim 2 \times 10^{-6}$ Pa s at room temperature (e.g. Rivalta et al. 2005; Rivalta and Dahm 2006). In addition to being much less dense than the host materials, air is compressible, such that a rising experimental dyke is subject to pressure decrease, and so to volume increase. In nature, magma compressibility (Rivalta 2010) and fluid exsolution (Menand and Tait 2001; Rivalta and Dahm 2006; Taisne and Jaupart 2011) are expected to lead to volume increase of propagating dykes, which is likely to affect their propagation dynamics. At the scale of the experiments, however, Rivalta and Dahm (2006) estimated that this effect is negligible.

Air has also been used to study the formation of shallow magma conduits resulting from explosive processes due to rapid gas exsolution of the rising magma (Haug et al. 2013; Galland et al. 2014b), with applications to maar-diatremes (e.g. Woolsey et al. 1975) (see also Table 1; Figs. 3 and 4e), kimberlite pipes (e.g. Gernon et al. 2009), hydrothermal vent complexes (Nermoen et al. 2010a), and mud volcanoes (e.g. Mazzini et al. 2009).

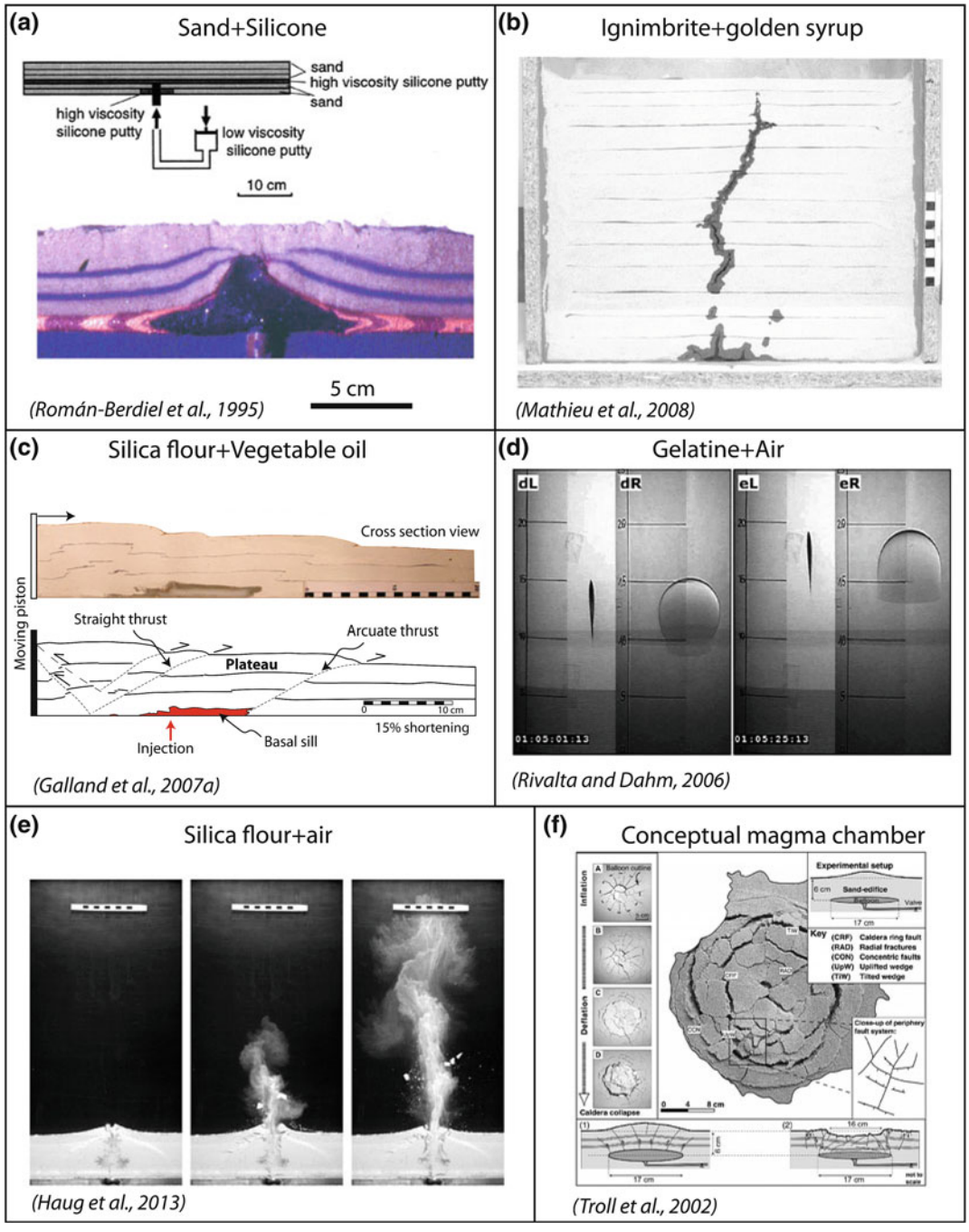
(a)
Sand+Silicone
sand
high viscosity silicone putty
sand
high viscosity
silicone putty
low viscosity
silicone putty
10 cm
5 cm
(Román-Berdiel et al., 1995)
(b)
Ignimbrite+golden syrup
(Mathieu et al., 2008)
(c)
Silica flour+Vegetable oil
Cross section view
Moving piston
Straight thrust
Arcuate thrust
Plateau
0
10 cm
15% shortening
Injection
Basal sill
(Galland et al., 2007a)
(d)
Gelatine+Air
dL
dR
eL
eR
01:05:01:13
01:05:25:13
(Rivalta and Dahm, 2006)
(e)
Silica flour+air
(Haug et al., 2013)
(f)
Conceptual magma chamber
Inflation
Deflation
Caldera collapse
Experimental setup
6 cm
Sand-edifice
Valve
17 cm
Key
(CRF) Caldera ring fault
(RAD) Radial fractures
(CON) Concentric faults
(UpW) Uplifted wedge
(TiW) Tilted wedge
Close-up of periphery fault system:
0 4 8 cm
16 cm
17 cm
(Troll et al., 2002)

◀**Fig. 4** Characteristic examples of laboratory models of volcano plumbing systems made by using various model materials. **a** Schematic drawing of experimental setup (*top*) and photograph of model cross section (*bottom*) of the sand + silicone experiments of Román-Berdiel et al. (1995). **b** Side view photograph of ignimbrite + Golden Syrup experiment (Mathieu et al. 2008). Ignimbrite powder simulates elasto-plastic rocks, whereas Golden Syrup simulates magma of intermediate viscosity. **c** Photograph and corresponding drawing of a cross-section of silica-flour + vegetable oil model (Galland et al. 2007a). The silica flour simulates the behaviour of the brittle crust, and exhibits faults, whereas the oil simulates magma of typical viscosity. The cohesion of the silica flour allows the oil to form sheet intrusion. Note that the oil solidifies, such that it becomes possible to make cross-sections through the models. **d** Time series of side- and front-view photographs of gelatine + air experiments (Rivalta and Dahm 2006). The gelatine simulates elastic rock, whereas the air simulates low viscosity magma. These experiments only simulate sheet intrusions (dyke and sills). **e** Time series of side-view photographs of silica flour + air 2D experiments (Haug et al. 2013). The silica flour represents brittle cohesive rock, and the air represents rapidly degasing magma or phreatomagmatically-generated water vapour. **f** Surface view photograph of model using conceptual magma chamber (Troll et al. 2002). The inflation/deflation of a balloon represents the replenishment and draining of a magma chamber, and the deformation induced in the overburden is observed at the surface of the models

Model rocks in some models are made of granular media (see below and Table 4). In these models, very low viscosity fluids like air and water are unsuitable for the simulation of magma intrusion, because they flow through the pores between the grains in addition to intruding the model. Moreover, the most commonly used granular media are made of silica, which is hydrophilic, such that the percolation of water through the pores is enhanced by surface tension. Therefore, other fluids such as oil (Grout 1945), honey, or Golden Syrup, have been used in this case (Table 2; Figs. 3 and 4b). The latter's viscosity is 50 Pa s at room temperature, and its density is 1400 kg m^{-3} (Mathieu et al. 2008; Kervyn et al. 2009; Abdelmalak et al. 2012).

Limiting the percolation of model magma in its host granular medium requires the use of a fluid that is chemically incompatible with its host, i.e. high surface tension. Good examples are greases (Johnson and Pollard 1973; Pollard and Johnson 1973), which are hydrophobic, such as the vegetable oil sold in France under the name Végétaline (Table 2; Figs. 3 and 4c) (Galland et al. 2006, 2009; Galland 2012). This fluid offers several advantages:

- its viscosity is low ($\eta = 2 \times 10^{-2}$ Pa s at 50 °C), such that it is suitable for simulating low viscosity magmas (Galland et al. 2006);
- it is solid at room temperature, and its melting temperature is 31 °C. It hence can be injected at molten state at a relatively low temperature (50 °C), that is technically easy to handle;
- it percolates very little into a very fine-grained granular host medium;
- at the end of the experiments, it solidifies after 15–30 min such that (i) the intrusions can be excavated and their shapes analysed in 3D (Galland et al. 2009; Galland 2012), or (ii) the models can be cut to reveal how intrusions relate to surrounding structures and overlying surface morphology (Galland et al. 2003, 2007a, 2008).

The vegetable oil's viscosity was measured via a rotary viscometer (Galland et al. 2006), which is a standard device to measure fluids of relatively low viscosities.

Finally, room temperature vulcanization (RTV) silicone (Gressier et al. 2010) has also been used as a model magma (Table 2). Its viscosity is 25 Pa s. RTV silicone solidifies after approximately five hours, such that the simulated intrusions can be excavated.

2.1.3 Conceptual Magma Chambers

Some experimental studies of volcanic plumbing systems do not focus on the magma emplacement mechanisms, but on the deformation patterns induced by inflating or deflating magma bodies (Table 1). In these cases, an inflating/deflating magma chamber is conceptually simulated with a balloon (Martí et al. 1994; Walter and Troll 2001; Troll et al. 2002; Geyer et al. 2006) or a moving piston (Acocella et al. 2001; Burchardt and Walter 2010). Although these experiments do not

Table 1 List of analog 'rock'-'magma' combinations used in the experimental studies referenced in this chapter

Rock analogue	Magma analogue	Part of plumbing system and dynamic regime modelled	References
Gels			
Gelatin	Air	Ascent of low viscosity dykes (buoyancy driven)	Takada (1990), Bons et al. (2001), Menand and Tait (2001), Muller et al. (2001), Ito and Martel (2002), Rivalta et al. (2005), Rivalta and Dahm (2006), Le Corvec et al. (2013)
	Hexane	Interactions between two ascending dykes	Ito and Martel (2002)
	Water	Propagation or ascent of intermediate viscosity dykes and sills (internal pressure driven)	Fiske and Jackson (1972), McGuire and Pullen (1989), Takada (1990), McLeod and Tait (1999), Menand and Tait (2001, 2002), Walter and Troll (2003), Kavanagh et al. (2006), Menand (2008); Kervyn et al. (2009), Tibaldi et al. (2014), Daniels and Menand (2015)
	Water-gelatin solution	Dyke, sill and laccolith emplacement under volcanic cone	Hyndman and Alt (1987)
	Mud	Hydraulic fracturing in different stress fields	Hubbert and Willis (1957)
	Water-Natrosol solution	Dyke nucleation from model magma reservoir	McLeod and Tait (1999)
	Water-Sugar solutions	Propagation and arrest of buoyancy-driven dyke	Taisne and Tait (2009), Taisne et al. (2011)
	Water-Glycerin	Dyke propagation and nucleation, and composite dyke emplacement	Koyaguchi and Takada (1994), McLeod and Tait (1999), Takada (1999)
	Molten wax	Cooling effects on dyke propagation	Taisne and Tait (2011)
	Vegetable oil	Cooling effects on dyke and sill emplacement	Chanceaux and Menand (2014)
	Silicone oils	Dyke propagation and nucleation	Takada (1990, 1994b), McLeod and Tait 1999), Watanabe et al. (2002)
	Grease	Sill and laccolith emplacement	Johnson and Pollard (1973), Pollard and Johnson 1973)
	Silicone putty	Dyke nucleation	Cañón-Tapia and Merle (2006)
Acryl gel	Air	Dyke propagation driven by magma pulses	Maaløe (1987)
	Oil	Dyke propagation	Maaløe (1987)
Agar-sugar gel	Water-glycerol solution	Dyke propagation along level of neutral buoyancy	Lister and Kerr (1991)

(continued)

Table 1 (continued)

Rock analogue	Magma analogue	Part of plumbing system and dynamic regime modelled	References
Granular materials			
Sand or sand with silicone layers	Silicone putty	Inflating or deflating laccoliths or stock-like intrusions, driven by internal overpressures or underpressures	Merle and Vendeville (1995), Román-Berdiel et al. (1995, 1997), Benn et al. (1998, 2000), Román-Berdiel (1999), Acocella et al. (2000, 2001, 2004), Roche et al. (2000, 2001), Girard and van Wyk de Vries (2005)
	Rigid piston	Deflating stock-like or sill-like intrusions	Burchardt and Walter (2010)
	Balloon	Deflating sill-like or laccolithic intrusions	Walter and Troll (2001), Lavallée et al. (2004), Geyer et al. (2006)
	Silicone-Oleic acid mix	Magma emplacement in deforming crust	Corti et al. (2005), Musumeci et al. (2005), Mazzarini et al. (2010), Montanari et al. (2010a, b), Ferré et al. (2012)
	Glycerol	Magma emplacement in tectonic extension	Bonini et al. (2001), Corti et al. (2001)
	Air	Explosive fragmentation of near vent region	Walters et al. (2006)
Wheat flour	Balloon	Deflating and/or inflating (cyclic) sill-like or laccolithic intrusions	Walter and Troll (2001)
Glass beads	Air	Formation of hydrothermal vent complex	Nermoen et al. (2010a)
	Air + glass beads	Diatreme formation	Ross et al. (2008a, b)
Crushed cohesive sand	Sleeve + plates	Opening of dyke and associated surface deformation	Trippanera et al. (2014)
Sand-plaster mix	Golden syrup	Caldera collapse and dyke propagation	Roche et al. (2001), Kervyn et al. (2009), Delcamp et al. (2012b)
	"Creamed" honey	Deflating sill-like intrusions	Holohan et al. (2008a, b, 2013)
Ignimbrite powder	Golden Syrup	Propagation and inflation of dykes, sills, and saucer-shaped intrusions driven by internal pressure	Mathieu et al. (2008), Mathieu and van Wyk de Vries (2009)
Sand-flour mix	Silicone putty	Inflating intra-edifice stock-like intrusions (cryptodomes), driven by internal overpressures. Deflating sill or stock-like magma chambers	Donnadieu and Merle (1998), Roche et al. (2000), Merle and Donnadieu (2000)
	Balloon	Deflating laccolithic magma chambers	Holohan et al. (2005)
Fused alumina powder	Balloon	Deflating and/or inflating laccolithic magma chambers	Martí et al. (1994)
Diatomite powder	RTV silicone	Dyke and sill propagation in the presence of pore fluid overpressure	Gressier et al. (2010)

(continued)

Table 1 (continued)

Rock analogue	Magma analogue	Part of plumbing system and dynamic regime modelled	References
Silica powder	Air	Explosive fragmentation of near vent region	Haug et al. (2013), Galland et al. (2014b)
	Vegetable oil	Propagation and inflation of dykes, sills, and saucer-shaped intrusions driven by internal pressure	Galland (2005, 2012), Galland et al. (2003, 2006, 2007a, 2008, 2009, 2011, 2014a), Ferré et al. (2012)
	Golden Syrup	Propagation and inflation of dykes driven by internal pressure	Abdelmalak et al. (2012)
Sand-Powdered clay mix	Rigid body	Deflating or inflating intrusions (idealised as sphere)	Komuro et al. (1984), Komuro (1987)
	Balloon	Deflating and/or inflating (cyclic) sill-like or laccolithic intrusions	Walter and Troll (2001), Troll et al. (2002)
Clay	Aqueous $KMnO_4$	Buoyancy-driven dyke ascent through brittle crust	Ramberg (1970, 1981)
Others			
Rigid walls	Air + glass beads	Mixing of materials in vents and conduits by gas-driven fluidization	Gernon et al. (2008, 2009)
	Wet plaster	AMS analysis on analogue intrusion	Závada et al. (2006, 2009, 2011)
Rigid piston	Aqueous corn-syrup solutions	Ring dyke intrusion and internal flow synchronous with a deflating sill-like intrusion	Kennedy et al. (2008)
Plasticine-wax	Silicone putty	Laccolith formation	Dixon and Simpson (1987)
Wet clay	Air	Diatreme formation	Grout (1945)
Water-corn syrup mix	Air	Diatreme formation	Grout (1945)

simulate the complexity of volcanic plumbing systems, the phenomenological results can be very inspiring for understanding geological structures observed in the field (Figs. 3 and 4f).

2.2 Model Rocks

Like magmas, rocks exhibit various mechanical behaviours depending on their lithology and on the scales (both length and time) of the simulated processes (Tables 3 and 4). Natural rocks exhibit complex rheologies, which combine elastic, viscous and plastic properties. Elastic deformation is reversible and usually occurs at low stresses/strains. If the stress/strain exceeds the rocks' elastic limit, they deform in an irreversible manner. They can do so by viscous behaviour, where the strain rate is a linear or power law function of the applied stress, or by plastic behaviour where the strain is a function of the applied stress. Various rheological laws describing these end member behaviours exist (Turcotte and Schubert 2002; Jaeger et al. 2009). In nature, rock rheology combines these different end members in a non-trivial manner, such that the complete rock behaviour is extremely challenging to characterise. Nevertheless, under given pressure and temperature conditions, length-scales and time-scales (strain rates), rock behaviour is dominated by one or the other end member. Different laboratory materials are available to simulate these dominant rock-mechanical behaviours.

Table 2 Types and mechanical properties of analogue 'magmas' used in laboratory models of volcanic plumbing systems

Model magma	Macroscopic behaviour	Viscosity	Density	References
Silicone polymers				
PDMS (silicone putty)	Stiff Newtonian fluid at low strain rates (power law fluid at high strain rates) Rigidity (shear) modulus $G = 2.6 \times 10^5$ Pa	1–3 × 10^4 Pa s (at room temperature)	965–1140 kg m^{-3}	Weijermars (1986), Acocella et al. (2001); ten Grotenhuis et al. (2002), Corti et al. (2005)
PDMS + inert fillers	Stiff Newtonian fluid if low filler content Stiff non-Newtonian fluid if high filler content	3×10^4 to 5×10^5 Pa s	Variable	Weijermars (1986), Boutelier et al. (2008), Reber et al. (2013)
PDMS + oleic acid	Sticky Newtonian fluid	7×10^2 to 1×10^4 Pa s	1060 kg m^{-3}	Corti et al. (2003, 2005), Reber et al. (2013)
RTV silicone	Viscous fluid Solidifies in contact with air	25 Pa s	1500 kg m^{-3}	Gressier et al. (2010)
Silicone oil	Viscous Newtonian fluid Incompressible	Used: 0.8×10^{-3} to 1.337 Pa s (can cover broader range of viscosities)	800–965 kg m^{-3}	Takada (1990, 1994a, b), de Bremond d'Ars et al. (2001), Watanabe et al. (2002)
Water-sugar solutions				
Corn-syrup	Viscous Newtonian fluid	81 Pa s at 26 °C	1425 kg m^{-3}	Kennedy et al. (2008)
"Creamed" honey	Intermediate viscosity, non-Newtonian (thixotropic) fluid	150–400 Pa s at 20 °C, decreasing with increased rotary shear rate	1350 kg m^{-3}	Holohan et al. (2008a, b)
Golden syrup	Sticky viscous fluid Incompressible Near Newtonian fluid	30–500 Pa s	1400 kg m^{-3}	Mathieu et al. (2008), Kervyn et al. (2009), Beckett et al. (2011), Schellart (2011), Abdelmalak et al. (2012), Delcamp et al. (2012b)
Aqueous corn-syrup solutions	Low viscosity Newtonian fluid	0.0155–0.127 Pa s	1211–1305 kg m^{-3}	Kennedy et al. (2008)
Glycerin–water solutions	Low viscosity Newtonian fluid	10^{-3} to 10 Pa s	1000–1260 kg m^{-3}	Takada (1990), Koyaguchi and Takada (1994), Bonini et al. (2001)
Concentrated sugar-water solutions	Low viscosity Newtonian fluid Incompressible	–	1102–1373 kg m^{-3}	Taisne and Tait (2009)
Water	Low viscosity Newtonian fluid Incompressible	10^{-3} Pa s	1000 kg m^{-3}	Hyndman and Alt (1987), Takada (1990), Menand and Tait (2002), Kavanagh et al. (2006)

(continued)

Table 2 (continued)

Model magma	Macroscopic behaviour	Viscosity	Density	References
Oils and waxes				
Grease	Viscous fluid	–	–	Johnson and Pollard (1973)
Molten vegetable oil	Low viscosity Newtonian fluid Solid at room temperature Incompressible	2×10^{-2} Pa s at 50 °C	890 kg m^{-3}	Galland et al. (2006)
Molten wax	Low viscosity Newtonian fluid Solid at room temperature Incompressible	4×10^{-4} to 7×10^{-2} Pa s	1100–1335 kg m^{-3}	Taisne and Tait (2011)
Others				
Mud	Viscous fluid, non Newtonian	–	–	Hubbert and Willis (1957)
Wet plaster	Bingham pseudoplastic fluid	0.8–6 Pa s	–	Závada et al. (2009)
Water–Natrosol solution	Low viscosity fluid	0.001–0.5 Pa s	–	McLeod and Tait (1999)
Aqueous $KMnO_4$ solution	Low viscosity dyed Newtonian fluid Incompressible	10^{-3} Pa s	–	Ramberg (1970, 1981)
Aqueous methylene blue-sodium polytungstate solution	Low viscosity dyed Newtonian fluid, Incompressible, adjustable density	10^{-3} Pa s	996–1010 kg m^{-3}	Hallot et al. (1994, 1996)
Hexane	Low viscosity Newtonian fluid (toxic for long-term exposure)	3×10^{-4} Pa s	1330 kg m^{-3}	Ito and Martel (2002)
Air	Low viscosity gas Compressible Low density	2×10^{-6} Pa s	1.2×10^{-3} kg m^{-3}	Takada (1990), Rivalta et al. (2005)

2.2.1 Plasticity-Dominated Materials (Weak Materials)

The most commonly used material for simulating model rocks is dry, loose, quartz sand (Tables 3 and 4; Figs. 3 and 4). Its cohesion is negligible (Schellart 2000; Mourgues and Cobbold 2003), such that (i) it fails along shear zones (mode II fractures), thereby simulating faults, and (ii) it does not allow open fractures (mode I fractures) to form. Failure of cohesion-less dry sand occurs according to a Mohr-Coulomb criterion that is defined, in theory, only by the angle of internal friction (ϕ). Dry sand is most applicable for simulating: (i) relatively low cohesion host materials in nature, such as unconsolidated or weakly lithified sediments or tuffs, and/or (ii) large-scale (several to 100s of km) processes involving regional-tectonic deformation (Corti et al. 2001, 2003, 2005; Musumeci et al. 2005; Mazzarini et al. 2010; Montanari et al. 2010a, b), whereby the material strength is assumed to decrease relative to the increasing length-scale (Schultz 1996).

Table 3 Types and mechanical properties of non-granular viscoelastic and viscoplastic materials used as analogue 'rock' in laboratory models of volcanic plumbing systems

Rock analogue	Macroscopic behaviour	Elastic properties	Fracture toughness	Density	Viscosity	References
Gels						
Gelatin	Viscoelastic solid Properties depend on: temperature, gelatin concentration, strain rate, and age (time elapsed after setting)	E = 390–16,000 Pa ν = 0.5	28–200 Pa $m^{1/2}$	1000–1010 kg m^{-3}	Complex viscosity at concentration of 2.5 wt%, temperature of 10 °C (gel-state), and strain rate of 10^{-2} s^{-1} is c. 50 Pa s. At 30–40 °C (sol-state), the viscosity lies between 0.36–0.0015 Pa s, decreasing with increased strain rate in the range 0.01–12 s^{-1}	Djabourov et al. (1988b),Takada (1990), Rivalta and Dahm (2006), Di Giuseppe et al. (2009), Kavanagh et al. (2013)
Acryl amid gel	Gel of variable rheology from nearly liquid to nearly brittle material (poisonous)	–	–	–	–	Maaløe (1987)
Aqueous sugar-agar gels	Viscoelastic solid Properties depend on: temperature, gel and sugar concentrations, waiting time	E = 1000 Pa	20 Pa $m^{1/2}$	1066–1310 kg m^{-3}	–	Lister and Kerr (1991)
Water	Newton viscous fluid	–	–	1000 kg m^{-3}	10^{-3} Pa s	Grout (1945)
Others						
Silicone putty	Newton viscous fluid	G = 3 × 10^4 to 2.6 × 10^5 Pa	–		10^4 Pa s	Ramberg (1981), Román-Berdiel et al. (1995), Corti et al. (2003), Boutelier et al. (2008)
Plasticine	Power law material (exponent n = 6–9.5)	–	–	1770 kg m^{-3}	–	McClay (1976), Weijermars (1986), Dixon and Simpson (1987)
Wax	Power law material (exponent n = 2)	E = 2 × 10^6 to 10^7 Pa	–	950 kg m^{-3}	–	Dixon and Simpson (1987)
Water-Corn syrup mix	Viscous fluid Temperature-dependent viscosity	–	–	1211–1305 kg m^{-3}	0.3–20 Pa s	Grout (1945), Kennedy et al. 2008)
Wet clay	Visco-elasto-plastic material	–	–	–	–	Grout (1945)

Table 4 Types and mechanical properties of granular materials used as analogue 'rock' in laboratory models of volcanic plumbing systems

Rock analogue	Macroscopic behaviour	Cohesion (estimated)	Friction angle	Density	References
Sand	Loose Coulomb material	12–123 Pa	25–35°	1300–1700 kg m^{-3}	Schellart (2000), Lohrmann et al. (2003), Mourgues and Cobbold (2003)
Wheat flour	Slightly cohesive Coulomb material	40–50 Pa (likely underestimated)	33°	570 kg m^{-3}	Walter and Troll (2001), Holohan et al. (2008a)
Sand-Plaster mix	Slightly cohesive Coulomb material	40–100 Pa (likely underestimated)	36°	1360–1560 kg m^{-3}	Roche et al. (2001), Kervyn et al. (2009, 2010)
Glass beads	Loose Coulomb material	64–137 Pa	20°	1547–1905 kg m^{-3}	Schellart (2000), Nermoen et al. (2010a, b)
Ignimbrite powder	Cohesive Coulomb material	100–230 Pa	38°	1400 kg m^{-3}	Mathieu et al. (2008)
Sand-flour mix	Cohesive Coulomb material	200 Pa	40°	1200–1400 kg m^{-3}	Donnadieu and Merle (1998), Holohan et al. (2005)
Fused alumina powder	Cohesive Coulomb material	200 Pa	38°	–	Martí et al. (1994)
Diatomite powder	Low density cohesive Coulomb material	300 Pa	–	400 kg m^{-3}	Gressier et al. (2010)
Silica flour	Cohesive fine-grained Coulomb material	300–400 Pa	40°	1050–1700 kg m^{-3}	Galland et al. (2006, 2009), Abdelmalak et al. (2012)
Sand-powdered clay	Cohesive Coulomb material Likely anisotropic	500–1300 Pa (likely overestimated)	26–31°	1500–1700 kg m^{-3}	Komuro (1987), Walter and Troll (2001)

Note that although dry sand is very weak, it does not exhibit a purely or ideally plastic behaviour. At low stresses and strains, it holds some reversible, elastic deformation, as demonstrated by the measurements of, e.g. Lohrmann et al. (2003) and Panien et al. (2006). Moreover, under loading conditions typical of laboratory experiments, dry sand fails in a semi-brittle fashion characterised by a stress drop that reflects a difference in static and dynamic friction coefficients. Such properties can become important in, e.g. models made of dry rice, which intend to simulate stick-slip faulting (Rosenau et al. 2010).

2.2.2 Elasticity-Dominated Materials (Strong Materials)

While sand is a weak end member of model rocks, the strong end member is gelatine (Table 3; Figs. 3 and 4d). At the scales of laboratory models, gelatine fails through the formation of open cracks (mode I fractures). In these models, gelatine behaves elastically, except locally at the tips, where complex viscoelastic processes occur. Hence gelatine is suitable for simulating: (i) natural host rocks of relatively high cohesion, such as well-consolidated sedimentary rocks or crystalline igneous or metamorphic basement rocks, and/or (ii) relatively small-scale processes (10s of m to a few km). Another advantage of gelatine, and gels in general, is that they become birefringent when strained (e.g. Dupré and Lagarde 1997; Dupré et al. 2010). When the models are placed between crossed polarizers, the strained domains of the models appear as coloured fringes, whereas unstrained domains appear dark (Richards and Mark 1966; Pollard and Johnson 1973; Taisne and Tait 2009, 2011).

The stiffness (Young's modulus, E) and the strength (fracture toughness, K_c) of gelatine can be jointly tuned by varying the gelatine concentration (Di Giuseppe et al. 2009; Kavanagh et al. 2013), while the Poisson's ratio is constant at $\nu = 0.5$ (Djabourov et al. 1988a, b). K_c can be calculated by measuring the fluid pressure required to propagate an existing crack (Menand and Tait 2002; Kavanagh et al. 2013). Systematic measurements show that E is a linear function of the gelatine concentration (Kavanagh et al. 2013). Nevertheless, for a given gelatine concentration, E is also time-dependent (Kavanagh et al. 2013), as the gelification process continues long time after the gelatine becomes solid. The value of K_c is a function of $\sqrt{E}$, and therefore of the gelatine concentration also (Kavanagh et al. 2013). This means that the preparation of gelatine models must follow a rigorous procedure, during which the waiting time between the preparation of the model and the experimental run is constant to ensure repeatable mechanical properties of the models.

2.2.3 Elasto-Plastic (Intermediate Strength) Materials

Dry sand and gelatine are the end members of rock mechanical behaviours, being plasticity- and elasticity-dominated, respectively. Nevertheless, it is known that complex processes, in which elastic and plastic behaviours are balanced, can govern natural rock deformation. Therefore, other model materials are needed to explore the effects of such complex rock rheology on magma emplacement in the Earth's crust. Good examples are cohesive granular materials (Table 4; Fig. 4b, c, e, f), such as ignimbrite powder (Mathieu et al. 2008, 2011; Mathieu and van Wyk de Vries 2011), fine-grained silica flour (Galland et al. 2006, 2009; Galland 2012), diatomite powder (Gressier et al. 2010), or sand-plaster mixtures (Roche et al. 2001), among others. When deformed, these materials typically exhibit both open (mode I) and shear (mode II) fractures at shallow and deep levels, respectively (Holland et al. 2006; Ketterman and Urai, 2015). Although their elastic properties remain challenging to estimate, these granular materials thus appear to be most suitable for reproducing the complex elasto-plastic mechanical behaviour of natural rocks.

Such cohesive granular materials also fail according to a Mohr-Coulomb criterion, but one that is defined by the material's tensile strength (T), cohesion (C) and its angle of internal friction (ϕ). These parameters control the depth of the transition from Mode 1 to Mode 2 fracturing. The cohesion and the angle of internal friction are properties that are measured indirectly. Firstly, a Mohr-Coulomb failure envelope is constructed via numerous shear tests conducted by using either a Hubbert-type shear box (Hubbert 1937; Mourgues and Cobbold 2003; Galland et al. 2006) or a Casagrande shear box (Rossi and Storti 2003). These apparatuses measure the shear strength τ of the tested material for variable normal stress σ_n. In a diagram displaying τ as a function of σ_n, many measurements exhibit a positive correlation. By fitting a function or 'failure envelope' to the data, it is possible to calculate C as being the intercept of the fitting function with the shear stress axis (typically the

y-axis in such a diagram; e.g. Schellart 2000; Mourgues and Cobbold 2003). The slope of the envelope, which is typically linear for most of its length, is the tangent of Φ. The tensile strength can be measured directly (Schweiger and Zimmermann 1999), but this requires specific devices, such that tensile strengths are rarely reported (Galland et al. 2006; Holland et al. 2006).

The degree of compaction (or closeness of packing) of a granular material strongly influences its mechanical properties (Lohrmann et al. 2003; Galland et al. 2006; Schreurs et al. 2006). Increased compaction leads to an increased density, cohesion and friction coefficient. The degree of compaction is controlled by the procedure of emplacing the material in the experimental apparatus. Compaction can be increased by shaking the model before running it, especially if the material is cohesive (Galland et al. 2009; Galland 2012), or by sifting the material if it is cohesionless (Lohrmann et al. 2003; Maillot 2013). Simply pouring the granular material in the experimental box is to be avoided as it leads to inhomogeneity in initial packing and hence in mechanical properties (Lohrmann et al. 2003).

2.2.4 Other Materials

Some of the first experiments of magma emplacement considered the whole crust as a viscous fluid. Grout (1945) injected air into media of various viscosities, such as wet clay, corn syrups and water-diluted syrups in order to simulate structures related to batholith emplacement. The rheologies of these pioneering model materials were not accurately measured, however. Silicone putty (Fig. 4a) is commonly used to simulate viscously deforming rock strata or formations, such as evaporite and shale (Román-Berdiel et al. 1995, 1997; Román-Berdiel 1999; Corti et al. 2001, 2003). Nevertheless, it becomes technically challenging to simulate both viscous host rock and the injection of viscous magma in the same experiments.

2.2.5 Summary

Most existing experimental studies of volcanic plumbing systems have used end member model rock materials with rheologies that are elasticity-dominated, plasticity-dominated, or viscous. Recently, the introduction of cohesive granular materials has allowed for exploring the effect of complex elasto-plastic behaviour of host rock on magma transport and emplacement. Moreover, although highly concentrated gels are elasticity-dominated, low-concentration gels (e.g. laponite, gelatine, agarose) exhibit viscoelastic behaviour at the length and time scales of laboratory experiments (e.g. Hallot et al. 1996; Di Giuseppe et al. 2009; Ruzicka and Zaccarelli 2011) and offer the possibility to explore experimentally the emplacement mechanism of magma into viscoelastic rocks, which is an essential step toward more geologically realistic models.

3 A Crucial Starting Point: The Model "Scaling"

The main advantage of laboratory modelling, i.e. that geological processes are simulated within the limits of a laboratory and the working time of the researcher, at the same time represents the method's biggest problem: the difference in scale between natural and laboratory volcanic plumbing systems. It is the scale gap between small models and huge intrusions that often leads to scepticism among Earth scientists regarding the applicability of laboratory models. Following the pioneering 19th century work that impressively reproduced natural structures, however, the 20th century saw a breakthrough with the development of the concept of scaling, with particular application to experimental models.

In 1937, Marion King Hubbert introduced the "theory of scale models" to the geological community and thereby shifted phenomenological analogue experiments from a qualitative to a quantitative approach. According to Hubbert (1937) and his followers (e.g. Ramberg 1970, 1981), laboratory models should be geometrically, kinematically, and dynamically similar to the natural system under investigation. Scaling is therefore an essential part for any laboratory study and needs to be considered to justify the applicability of the model results. Nevertheless,

there is a lot of confusion among Earth scientists about correct scaling of laboratory models to geological systems, and first of all about the meaning of "scaling".

The main confusion is related to the misunderstanding of the goals of laboratory models. They are not designed to exactly mimic a given geological system, as many Earth scientists think, but to understand underlying generic processes, either individually or in combination, and to identify or demonstrate physical laws governing these processes. In order to prove that any physical laws identified in laboratory experiments apply to geological systems, these laws should be dimensionless, i.e. they are independent of the length scale, time scale, etc., which is why they are often called scaling laws.

The procedure for establishing dimensionless scaling laws involves two steps: (i) a *dimensional analysis* of the considered physical problem, to identify the dimensionless governing parameters, and (ii) a *comparison of laboratory and geological values of these dimensionless parameters* to test the geological relevance of the experimentally-derived physical laws.

3.1 Dimensional Analysis

The principles of dimensional analysis are described in detail by e.g. Barenblatt (2003). The first applications of such an approach in laboratory experiments of volcanic processes has been conducted by Tibaldi (1995) and Merle and Borgia (1996). The approach consists of identifying the dimensionless physical parameters that govern the processes to be addressed.

The first step is to list the n parameters *with dimensions* that are relevant for the processes to be studied. In mechanical systems, usual dimensions are those of length [L], mass [M] and time [T]. An analysis of thermo-mechanical systems requires the addition of the dimension of temperature [K].

Let us consider a simple conceptual example: the stability of a volcanic edifice. The aim of the following paragraphs is only to provide an illustrative example of dimensional analysis. In the case of edifice stability, the effect of the coefficient of friction is obvious, however it is not suitable for illustrating the implementation of dimensional analysis. Instead, we will consider the effect of material cohesion on edifice stability, which has not been considered. In the following sections, we will thus assume that the coefficient of friction is taken as a constant, and it will be ignored despite its established relevance. The dimensional analysis developed in the following sections thus only aim at assessing the effects cohesion on edifice stability.

The edifice has a height h ($[h]$ = L), diameter D ($[D]$ = L), a density ρ ($[\rho]$ = M L^{-3}), and the material making the edifice has a cohesion C ($[C]$ = M L^{-1} T^{-2}). The square brackets here represent the dimension, not the unit, of each parameter. The volcano is exposed to gravitational acceleration g ($[g]$ = L T^{-2}). Again for illustrative purpose, we consider the coefficient of friction to be a dimensionless constant and we will ignore it during the following analysis, despite its established relevance. From this list of parameters, the experimentalist should separate the governing parameters, i.e. those known and controlled, from the parameters to measure. To study the stability of a volcanic edifice in the laboratory, two approaches can be developed. A first approach (example 1) consists of controlling both the height and diameter of the edifice, such that h, D, ρ, g and C are governing parameters. The experimentalist builds volcanic edifices of controlled sizes using model materials of varying cohesions, and observes whether they are stable or not. A second approach (example 2) consists of controlling the height of the edifice only, and measuring the diameter, such that h, ρ, g and C are the governing parameters and D the measured quantity. The experimentalist gradually builds the cone with model materials of varying cohesions at a critically stable slope to a given height h, and measures the diameter D of the cone, as in the experiments of Ramos et al. (2009). We base the following sections on these examples.

The second step is to identify the number k of the governing parameters with *independent dimensions*. A set of parameters has independent dimensions if their dimensions cannot be

expressed as a function of each other's (Barenblatt 2003). For instance, the height of a volcanic edifice and the density of the rock have independent dimensions, because the dimension of the density ($[\rho] = \mathrm{M\,L^{-3}}$) cannot be expressed as a function of the dimension of the depth ($[h] = \mathrm{L}$) only. In contrast, the rock cohesion ($[C] = \mathrm{M\,L^{-1}\,T^{-2}}$), the density ($[\rho] = \mathrm{M\,L^{-3}}$), the gravity ($[g] = \mathrm{L\,T^{-2}}$) and the height of a volcanic edifice ($[h] = \mathrm{L}$) do not have independent dimensions, given that the dimension of C is a function of the dimensions of ρ, g and h:

$$\begin{aligned}[C] &= \mathrm{M\,L^{-1}\,T^{-2}} = [\rho] \times [g] \times [h] \\ &= \left(\mathrm{M\,L^{-3}}\right) \times \left(\mathrm{L\,T^{-2}}\right) \times (\mathrm{L}) \end{aligned} \quad (1)$$

In example 1, it is thus possible to show that ρ, g, h are governing parameters with independent dimensions, whereas the dimensions of C and D can be expressed as functions of those of ρ, g, and h. Note that the selection of the governing parameters with independent dimensions is not unique. For instance, one can choose ρ, g, and D as governing parameters with independent dimensions, C and h being the others. But in both cases, among the set of $n = 5$ governing parameters, $k = 3$ parameters have independent dimensions. In example 2, there is only one possibility: ρ, g, and h are the governing parameters with independent dimensions, C is the other governing parameter, and D is the measured quantity. Therefore, among $n = 4$ governing parameters, $k = 3$ parameters have independent dimensions.

The third step is to calculate the number m of dimensionless parameters that characterise the physical system to be simulated in the experiments. This number is easily calculated by using the Π-theorem (or Buckingham Π-theorem), which is the central theorem in dimensional analysis. It states that "*a physical relationship between some dimensional (generally speaking) quantity and several dimensional governing parameters can be rewritten as a relationship between a dimensionless parameter and several dimensionless products of the governing parameters; the number of dimensionless products is equal to the total number of governing parameters minus the number of governing parameters with independent dimensions*" (Barenblatt 2003). This means that the number m of dimensionless parameters to be defined is given by $m = n - k$.

In example 1, ignoring the coefficient of friction, the total number of governing parameters being $n = 5$, and the number of governing parameters with independent dimensions being $k = 3$, the number of dimensionless parameters governing the physics of a volcanic edifice is $m = n - k = 2$. If ρ, g and h are chosen as the governing parameters with independent dimensions, the two dimensionless parameters are:

$$\Pi_1 = \frac{C}{\rho \times g \times h} \quad (2)$$

$$\Pi_2 = \frac{h}{D} \quad (3)$$

In example 2, again ignoring the coefficient of friction, $n = 4$ and $k = 3$, therefore the number of dimensionless parameters governing the defined physical system is $m = 1$. A clear choice for this parameter is simply:

$$\Pi_1 = \frac{C}{\rho \times g \times h} \quad (4)$$

In order to test the relevance of the dimensional analysis, the defined dimensionless numbers should have a physical meaning. In example 1, the physical meanings of Π_1 and Π_2 are straightforward. Π_2 expresses the slope of the volcanic edifice. Π_1 expresses whether the volcanic edifice is gravity-controlled ($\Pi_1 \rightarrow 0$) or strength-controlled ($\Pi_1 \rightarrow \infty$). In the first case, the material that composes the edifice is macroscopically loose, such as sand, and the edifice is expected to collapse under its own weight along shear planes (i.e. faults). Conversely, in the second case the material is macroscopically cohesive, and the edifice is expected to be stable.

Several widely used dimensionless numbers are called by the name of their discoverer. A good example is the Reynolds number (Re), which quantifies the ratio between the inertial

forces in a flowing fluid and the viscous forces. A critical value of the Reynolds number sets the boundary between the laminar flow regime and the turbulent flow regime. This number is thus highly relevant for magma flow. Another example is the Rayleigh number (*Ra*), which quantifies the ratio between the buoyancy forces of a heated fluid and the viscous forces (i.e. those forces resisting flow). A critical value of the Rayleigh number sets the boundary between a convective system and a non-convective system: this has high relevance for mantle convection and the dynamics of magma chambers.

In example 2, we note that the measured quantity D has not been used in the definition of the dimensionless parameter Π_1. At this stage, we can define a dimensionless parameter Π, which is defined as a ratio between the measured quantity D and a function of the governing parameters with independent dimensions. Here a definition is given by $\Pi = D/h$. The Π-theorem implies that a dimensionless quantity Π to be measured in the experimental study can be rewritten as a function of the other m Π-numbers, such as:

$$\Pi = F(\Pi_1, \Pi_2, \ldots, \Pi_m) \tag{5}$$

The function F is the physical law that governs the simulated processes. This relationship between the dimensionless output and the dimensionless input parameters should dictate the experimental strategy. In order to test the effects of each dimensionless parameter Π_i during an experimental project, the dimensional experimental parameters should be varied such that Π_i is systematically varied, while the others are kept constant. Applied to each Π_i-number and so by constraining the function F, the experimental results will contribute to deriving the physical laws that govern the investigated processes.

This strategy can be adapted to two different approaches depending on the nature of the model outputs.

If the model output is not a measured quantity, but contrasting physical behaviours, the aim of the experimental procedure will be to explore the parameter space, i.e. to vary systematically the values of the dimensionless parameters Π_i, to map under which conditions these contrasting physical behaviours occur (Fig. 5a). This procedure is equivalent to building a phase diagram, the contrasting physical behaviours being physical phases. Let us illustrate this approach with our example 1. An experimental procedure would

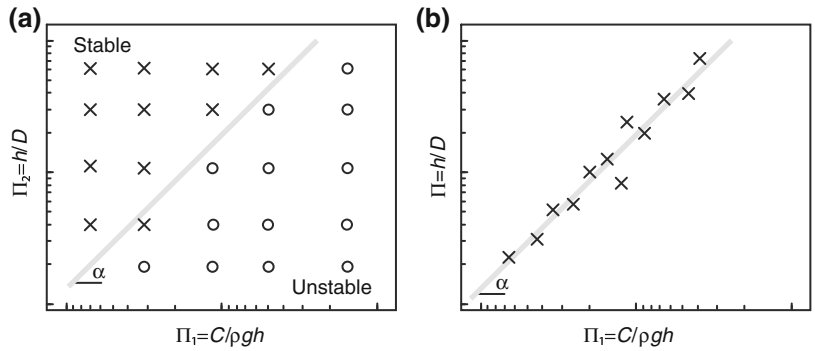

Fig. 5 Qualitative diagrams illustrating the two main experimental strategies defined from dimensional analysis. **a** Example 1, when the model output is not a measured quantity but a number of physical behaviours, each behaviour (here stability or collapse of a volcanic edifice; see Sect. 3.1 for explanation) is plotted in a diagram with the dimensionless input parameters as x- and y-axes. This so-called phase diagram maps the physical fields, in which the observed behaviours are expected. The field transitions are commonly described by power laws of the form $\Pi_2 \propto \Pi_1^{\alpha}$. **b** Example 2, i.e. when the model output is a measured quantity Π (here the slope $\Pi = h/D$ of a volcanic edifice at stability criterion; see text for explanation), it is plotted as a function of the dimensionless input parameters (here $\Pi_1 = C/\rho g h$, see text for explanation). The correlation between Π and Π_1 is usually a power law of the form $\Pi \propto \Pi_1^{\alpha}$

consist of building a model volcanic edifice of given and controlled height h and width D, with materials of given cohesions C (and a constant coefficient of friction). Once the edifice is built, one can see if it is stable or unstable (collapses). The experimental strategy would be to run many experiments by varying systematically and independently Π_1 and Π_2 to explore how these parameters control the stability of a volcanic edifice. By plotting all the experiments in a diagram of Π_1 against Π_2, and by indicating the corresponding physical behaviour with e.g. different data point symbols, it is possible to identify physical fields, or phases, separated by transitions. The transitions between the fields are mostly expected to be power laws of the form: $\Pi_2 \propto \Pi_1^{\alpha}$.

If the model output is a measured quantity, the aim of the experimental procedure will be to establish a correlation between the measured dimensionless parameter Π and the dimensionless input parameters Π_i (Fig. 5b). In our example 2, an experimental procedure would consist of gradually building model volcanic edifices of given height h with materials of given cohesions C, and measure the final diameter D of the edifices. The experimental strategy would be to run many experiments by systematically varying Π_1 to explore how these parameters control the output parameter Π. If the parameters Π and Π_i are well defined, they are expected to correlate, and most likely following a power law. Hence the correlation should appear as a straight line of slope α in a log-log plot, showing that the physical law linking Π and Π_i is a power law of the form: $\Pi \propto \Pi_1^{\alpha}$.

3.2 Similarity to Geological Systems

After performing the dimensional analysis, identifying the Π-numbers, and obtaining the experimental results, the geological relevance of the experimentally-defined scaling laws needs to be tested. In other words, we need to test whether the processes simulated in the laboratory are physically similar to the geological processes. This concept of *physically similar phenomena* is central to geological laboratory modelling. "*Two systems are considered similar if the values of the dimensionless parameters are identical, even if the values of the governing dimensional parameters differ greatly*" (Barenblatt 2003). It means that although the scales of the laboratory models are drastically different to the scales of the geological systems they aim to simulate, the laboratory models will be physically similar to their geological equivalents if their respective Π-numbers have the same values. Therefore, the experimentalist must compare the values of each Π-number in the laboratory with the values of these numbers in the geological system: if the ranges of values overlap, the two systems are similar, and the experimental results are relevant to the geological system.

The principle of similarity can be also less strictly applied if we consider the physical meaning of the Π-numbers. Let us consider the height-to-diameter ratio of a volcanic edifice $\Pi = h/D$. In geological settings, Π is typically 0.12–0.6 (Grosse et al. 2012). In laboratory experiments, the resulting values of Π will be larger or smaller than the geological values of Π, if the model material is too cohesive or too loose, respectively. In this case, the laboratory volcanic edifices are not rigorously similar to the geological edifices. Nevertheless, in our example 2 if a plot of the laboratory and geological values of Π against $\Pi_1 = C/\rho gh$ shows an alignment along the same scaling law (Fig. 6), it would mean that both edifice types are governed by the same physical law. Consequently, in both the laboratory and geological systems, the physical regimes are the same, and the law identified in the laboratory model of volcano edifice can be considered physically relevant to geological edifices. In our example 1, it is also important to consider the physical regime (i.e. the physical 'phase' in the phase diagram): if the geological edifice and the laboratory edifices have different values of Π_1 and Π_2, but if both are in the stable field, they can be considered physically equivalent, without being similar sensu stricto. Likewise, the Reynolds numbers related to magma flow in the laboratory and its geological prototype can be different, but if both are way below the critical value, the flow regimes are both laminar (see discussion in, e.g. Galland et al. 2009).

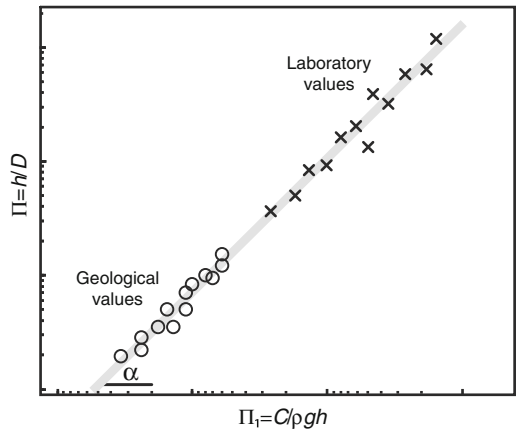

Fig. 6 Schematic diagram illustrating a potential mismatch between laboratory and geological values of the slope h/D against $C/\rho gh$ for a volcanic edifice (see text for explanation). The model and geological edifices exhibit different values, implying that they are not strictly similar. Nevertheless, they plot on the same scaling law, showing that they result from the same physical processes. Therefore, such diagram shows that the laboratory models are physically equivalent to the geological systems, without being strictly similar

4 Geological Applications

There is an extensive literature on laboratory experiments of volcanic plumbing systems. We structure our review of these past studies according to the simulated geological structures or processes, which include: (1) dykes, (2) cone sheets, (3) sills, (4) laccoliths, (5) caldera-related structures and intrusion, (6) ground deformation associated with shallow intrusions, (7) magma/fault interactions and (8) explosive volcanic vents.

4.1 Dyke Formation

Dykes are the most common magma conduits in the Earth. They are steeply inclined sheet-like intrusive bodies that are discordant to any mechanical stratigraphy in their host rocks, and that usually exhibit a very small thickness-to-length ratio (between 10^{-4} and 10^{-2}, Rubin 1995). The latter characteristic means that model dykes in experiment set-ups of a few decimetres in length should theoretically be very thin (between 1 and 10^{-3} mm). This is very challenging to achieve.

Magmatic dykes are commonly assumed to be emplaced by hydraulic fracturing (Pollard 1987; Lister and Kerr 1991). One of the first experiments that intended to simulate hydraulic fracturing consisted of elastic gelatine as the model rock, and mud as the model magma (Fig. 7) (Hubbert and Willis 1957). Although the motivation of these experiments was to simulate hydraulic fracturing in boreholes, the experimental results are relevant for igneous dykes and sills. These experiments demonstrated that the stress field applied to the model controlled the orientation of hydraulic fractures nucleating from a vertical pipe: the fracture planes were always perpendicular to the least principal stress σ_3, and parallel to the (σ_1-σ_2) plane (Sibson 2003). In addition, these experiments demonstrated qualitatively the strong effect of mechanically layered host rocks on dyke propagation.

Experiments with gels have since been used extensively to unravel various aspects of dyke propagation through the Earth's crust. Gels are transparent, so it is possible to track the evolution of growing intrusions. This has proven very practical for unravelling the physical processes governing dyke nucleation and propagation. The following provides a short summary of our understanding of the physics of dykes from gel experiments.

4.1.1 Dyke Nucleation from a Magma Reservoir

An important aspect of dyke formation is their nucleation from a magma reservoir. Using gel +silicone experiments, Cañón-Tapia and Merle (2006) simulated dyke nucleation from an overpressurised magma reservoir made of silicone putty. The silicone putty was injected at a constant flow rate via a computer-controlled piston. The results suggest that dykes nucleate in response to the overpressure in the reservoir, rather than because of buoyancy forces arising from the density difference between the silicone and the gel. Interestingly, these experiments highlight the discontinuous behaviour of dyke propagation from a magma reservoir, which results from a competition between the strain energy accumulated in the gel and the pressure evolution in the reservoir.

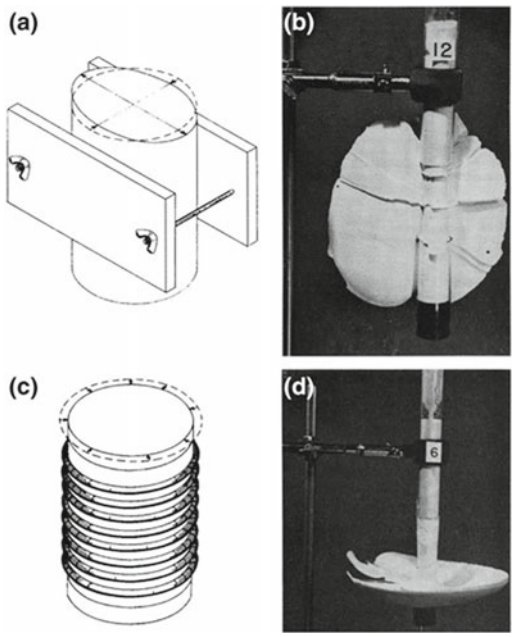

Fig. 7 Characteristic results of pioneering experiments of Hubbert and Willis (1957) to address the mechanics of hydraulic fracturing. **a** Drawing of experimental setup with anisotropic horizontal stress. A cylinder of gelatine is compressed in one direction between two plates. Mud is injected in the gelatine, and form hydraulic fractures. **b** Photograph of vertical hydraulic fracture obtained from experimental setup displayed in a. The fracture is perpendicular to the least principal stress, which is horizontal and parallel to the plates. **c** Drawing of experimental setup with isotropic horizontal stress. A cylinder of gelatine is compressed horizontally in every direction by a series of elastic strings. **d** Photograph of horizontal hydraulic fracture obtained from experimental setup displayed in c. The fracture is perpendicular to the least principal stress, which is vertical

Further to the above experiments, McLeod and Tait (1999) investigated the effects of magma viscosity on dyke nucleation (Fig. 8a). By controlling the injection pressure rather than the injection flow rate, McLeod and Tait (1999) showed that for an instantaneous increase in model magma pressure, the time delay required to nucleate a dyke from a reservoir in a gelatine host increases with increased fluid viscosity (Fig. 8a). In addition, for gradually increasing pressure in the reservoir, the critical pressure required to nucleate a dyke is larger when the magma is more viscous. These results suggest that the pressures required to form felsic dykes are much higher than for mafic dykes.

4.1.2 Dyke Propagation in a Homogeneous and Isotropic Medium—The Effects of Buoyancy

Fundamental mechanisms controlling the propagation of dykes have also been studied by using simple gel experiments that take advantage of the gel's isotropic and homogeneous nature. This nature means that effects on propagation that are related solely to buoyancy, i.e. the force arising from the difference in density between the magma and its host rock, can be isolated and understood.

Takada (1990) concluded that the shapes and velocities of propagating dykes depend largely on the density difference between the intruding fluid and the gel—i.e. that they are buoyancy-controlled (Fig. 8b). In Takada's (1990) experiments, the liquid was injected with a needle, either from the side or the bottom of the models. Thus, the dykes were of controlled volumes, and neither the applied overpressure nor the injection flow rate was controlled. Takada (1990) concluded that: (i) Intrusion shapes are governed by the balance between the buoyancy forces and the strength of the gel. If buoyancy is small, the dykes are symmetrical penny-shaped, whereas if the buoyancy is large, the dykes are vertically asymmetrical in transverse section where they exhibit a tear drop shape with a fat curved upper tip and a sharp straight lower tip. (ii) The propagation direction is governed by the balance between the buoyancy forces and the strength of the gel: if buoyancy is small, the dyke propagates in all directions, whereas if the buoyancy is large, the dyke propagates dominantly upward. (iii) A buoyant crack of constant volume propagates itself only if it is larger than a critical length (see also Algar et al. 2011). (iv) The propagation velocity of the dyke is correlated to the density difference between the gel and the injected fluid. (v) When buoyancy forces are higher, the leading edge of the intrusion becomes broad, leading to the splitting of the dyke tip.

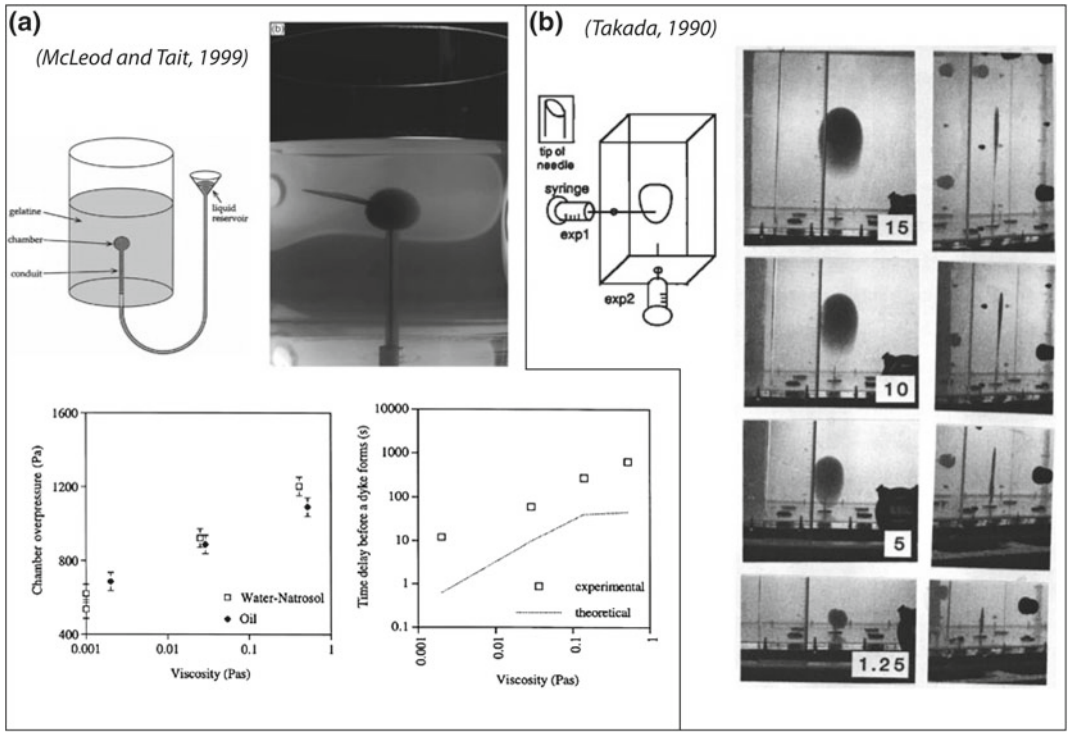

Fig. 8 **a** Schematic drawing of experimental setup (*upper left*) and photograph of a characteristic experiments of dyke nucleation from a magma reservoir (*upper right*; McLeod and Tait 1999), in which fluids of various viscosities are injected at controlled pressures in a gelatine model from a cavity. The *lower left graph* shows how the viscosity controls the fluid pressure required to nucleate a dyke, whereas the lower right graph shows how the viscosity of the injected fluid controls the time scale of dyke nucleation from a reservoir. **b** Experimental setup (*left*) of Takada's (1990) experimental study of dyke propagation. Liquids of various densities and viscosities were injected via a syringe, and their subsequent propagation was monitored with photographs. The series of photographs show profile (*left*) and front (*right*) views of the time evolution of a propagating dyke during a characteristic experiment

In addition to examining buoyancy on dyke propagation, Menand and Tait (2002) investigated the effect of overpressure in a magma reservoir. They imposed an overpressure by placing a water reservoir at given vertical distances above the model. They show that dyke propagation exhibits two regimes: (i) an initial overpressure-dominated regime during which the dyke propagates both vertically and laterally, and (ii) a subsequent buoyancy-dominated regime during which the dyke propagates mostly vertically. The transition between both regimes is controlled by a critical size of the dyke, in agreement with Takada's (1990) experiments.

Finally, buoyancy-driven cracks of constant volume in gelatine experiments accelerate as they approach the free surface (Rivalta and Dahm 2006). Such a phenomenon has also been observed in volcanoes, such as Piton de la Fournaise, Réunion Island (Battaglia 2001), and appears crucial for forecasting the timing of volcanic eruptions by means of dyke-induced seismicity (Rivalta and Dahm 2006). Interestingly, the experiments show that the free surface effects are larger when the fracture is ascending more slowly (i.e. when the buoyancy forces are smaller).

4.1.3 Effects of Contrasting Magma Viscosities on Composite Dyke Propagation

Magma batches of different compositions, and so of different viscosities, can lead to the formation

of composite dykes, the cores of which are felsic and the rims are mafic (Walker and Skelhorn 1966). A spectacular example is the Streitishorn dyke, Eastern Iceland (Paquet et al. 2007). Koyaguchi and Takada (1994) simulated the propagation of a dyke from a magma reservoir containing two fluids of contrasting viscosities within an isotropic gelatine medium. They show that low viscosity fluid (mafic magma) at the dyke tip controls the tip's propagation. This lower viscosity fluid in the dyke tip lubricates the subsequent flow of the higher viscosity fluid (felsic magma) into the middle of the dyke. Such process may considerably enhance the drainage of a silicic magma chamber and the flow of viscous felsic magmas over large distances.

4.1.4 Effects of Mechanical Heterogeneity (Prexisting Dykes or Layering) on Dyke Propagation

The medium through which dykes propagate in nature, the Earth's lithosphere, is neither isotropic nor homogeneous. Two first-order planar heterogeneities that can greatly influence dyke propagation include pre-existing dykes and sedimentary layering. Experiments investigating the effects of such heterogeneities (Maaløe 1987; Bons et al. 2001; Rivalta et al. 2005; Kavanagh et al. 2006) show that they represent fundamental features controlling the average dyke propagation velocity, the propagation direction, and possibly also dyke geometry.

Maaløe (1987) and Bons et al. (2001) conducted gelatin and air/water model experiments that suggest that dykes propagate in a stepwise manner due to successive magma batches. Maaløe (1987) showed that an initial magma batch forms a dyke, which stops after some distance. This initial dyke only propagates further if a new magma batch reaches it. Bons et al. (2001) simulated dyke propagation in heterogeneous gelatine, and showed that the path of an initial dyke greatly controls the propagation of subsequent dykes. In addition, Bons et al. (2001) show that local heterogeneities stopped a propagating dyke, which only continues propagating if it is fed by a new magma batch.

Rivalta et al. (2005) and Kavanagh et al. (2006) addressed the mechanisms of dyke propagation through mechanically-layered media, which are common in sedimentary basins and lava piles. They show that the velocity of the propagating dyke is correlated with the strength and Young's modulus of the host: a dyke decelerates when it reaches a stronger layer, and vice versa. In addition, the nature of the layer interface can considerably affect the 3-dimensional shape of a dyke (Fig. 9). For instance, if a dyke reaches a very strong layer interface, its vertical propagation is arrested and it propagates laterally. If the driving pressure in the dyke is large enough, the dykes can turn into horizontal sills at such interfaces (see also the Sect. 4.3 below).

4.1.5 Effects of Anisotropic Stress Fields (From Regional Tectonics or Local Topography) on Dyke Propagation

It has been long hypothesised from field relationships that dyke emplacement is greatly controlled by the regional stress field (Hubbert and Willis 1957; Sibson 2003; Takada 1999). If the stress field is homogeneous but anisotropic (i.e., the magnitudes of the principal stresses differ), dykes are expected to be parallel to each other, and perpendicular to the least principal stress, σ_3 (Anderson 1936). In addition, topographic features, such as volcanic edifices, are thought to produce local anomalous stress fields that can greatly affect the propagation of dykes (Odé 1957; Johnson 1970; Nakamura 1977). This effect of gravitational stresses related to topography on dyke geometry and propagation has been subject of numerous experimental studies.

Gelatine experiments have been used to investigate how the stress generated by the load of a volcanic edifice affects dyke propagation in the region around the edifice. Muller et al. (2001) and Watanabe et al. (2002) used injected dykes at varying distances from a load, and observed that dykes close to the load were attracted toward it, whereas dykes far away from the load were not (Fig. 10). They show that the critical distance at which a dyke is affected by the load is correlated

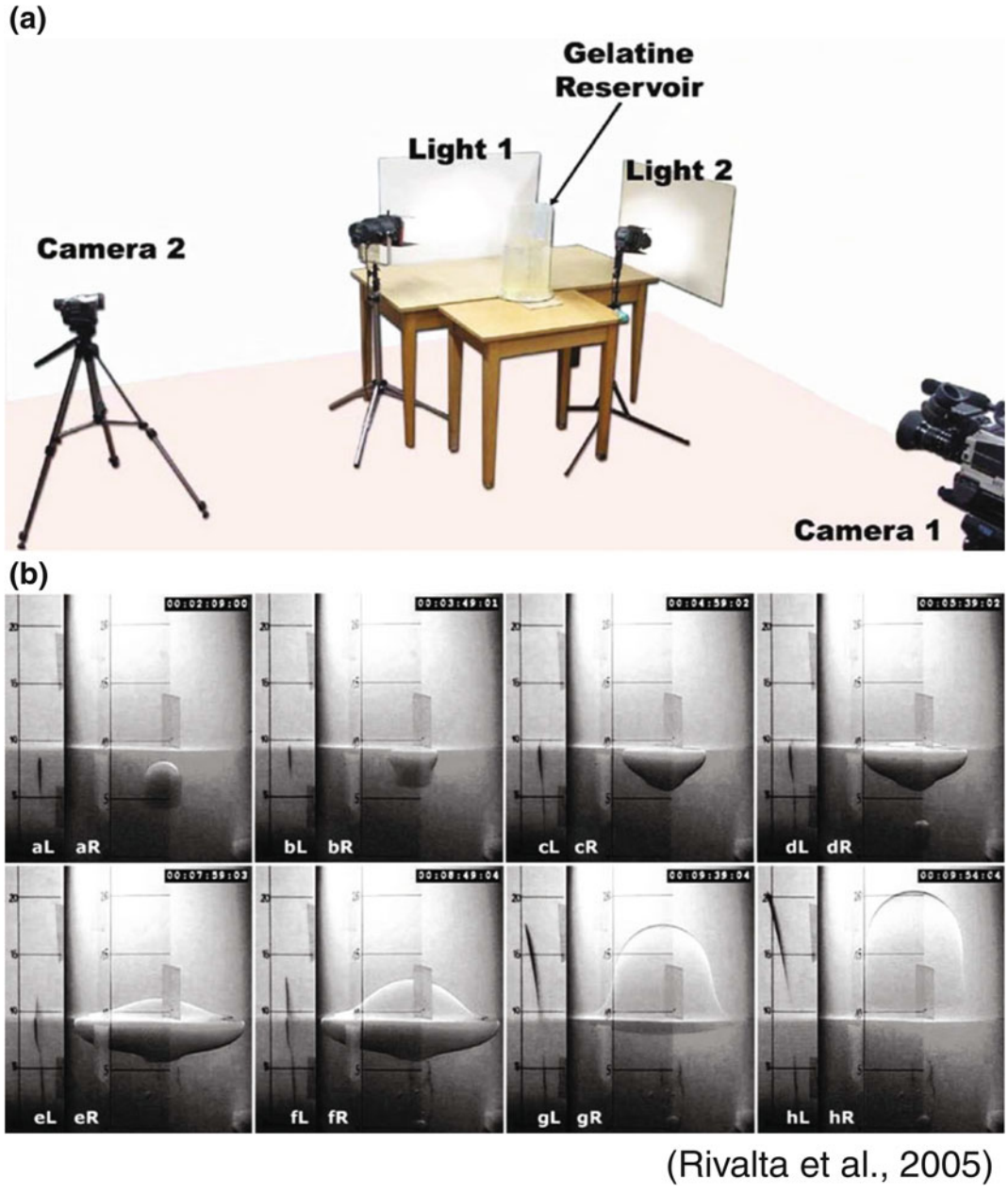

Fig. 9 **a** Experimental apparatus designed by Rivalta et al. (2005) to study dyke propagation through layered media. The model magma is air, and the model rock consists of two layers of gelatine of different concentrations. **b** Time series of photographs of a characteristic experiment of dyke propagation in a layered medium. Here the upper layer is more resistant than the lower layer. When the rising dyke reaches the interface between the layers, it is temporarily stopped upward but propagates laterally (*photographs* bR, cR, dR), until the dyke tip starts piercing through the upper, tougher layer (*photograph* eR). Interestingly, the dyke is wider in the upper layer than in the lower layer, although it has the same volume

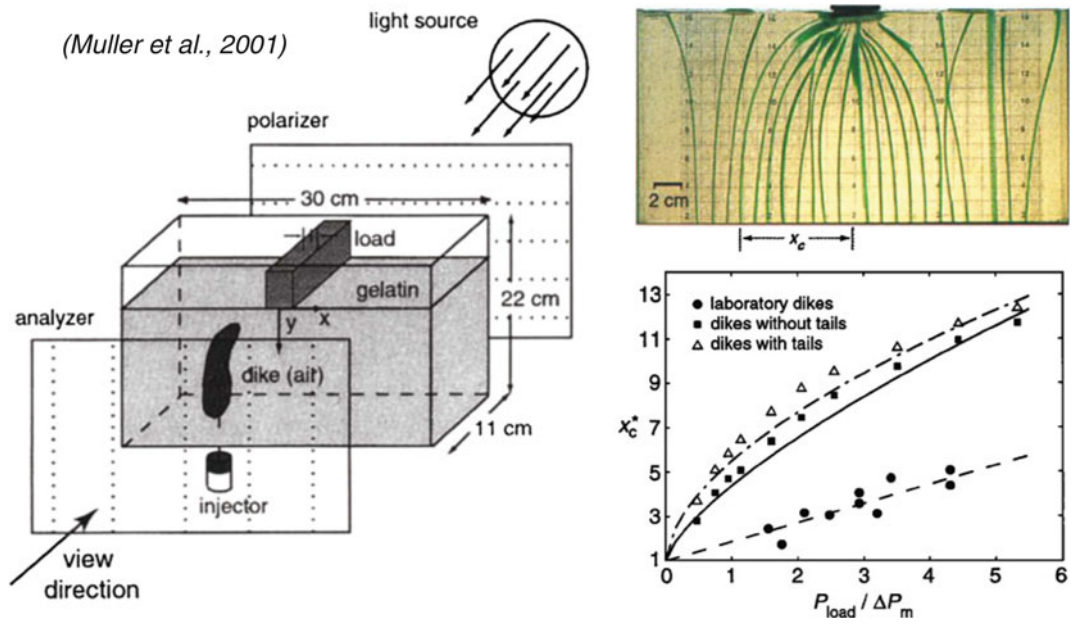

Fig. 10 Experimental study of Muller et al. (2001), in which air-filled dykes are injected in a gelatine model, at the surface of which a load is placed. Dyke injection is successively performed at an increased lateral distance x from the position of the load. The *upper right* photograph shows dyke trajectories during an experiment: the dyke closer to a critical distance x_c are attracted toward the load, whereas the other dykes are not attracted by the load. The *lower right* diagram shows that the critical distance x_c in the experiments (*black discs*) is a linear function of the ratio between the pressure induced by the load (P_{load}) and the excess pressure in the dyke (ΔP_m). Muller et al. (2001) also performed numerical modelling, and obtained different behaviours of x_c as a function of $P_{load}/\Delta P_m$ (see results in *lower right* graph.)

with the ratio of average pressure at the base of the load (i.e. the height of the edifice) to the dyke driving pressure: larger loads attract more distanced dykes. The particular trajectories taken by attracted dykes are also affected by this ratio. This attraction of dykes rising through the crust by volcanic loads may help to explain the absence of volcanism between large volcanoes.

Laboratory experiments of dyke emplacement also show that topography-derived stresses can greatly control the orientation of dykes *within* volcanic edifices (Fiske and Jackson 1972). Gelatine experiments by Hyndman and Alt (1987), McGuire and Pullen (1989), Delcamp et al. (2012b), for instance, show that dykes orientate along the long axis of an elongated volcanic edifice, albeit with some divergence at the edifice periphery (Tibaldi et al. 2014). In addition, the experiments of McGuire and Pullen (1989) show that: (i) shallow dykes below edifices stop propagating upward, and start propagating laterally to give rise to a lateral fissure eruption, and (ii) the behaviours of intruding dykes differ according to their initial position with respect to the summit of the edifice. Kervyn et al. (2009) show a similar deflection of the dyke away from the summit of an edifice standing on a brittle substratum of controlled thickness (Fig. 11a); deflection depends on the thickness of the substratum, on the edifice slope, and on the overpressure within the dyke. These experimental results are consistent with lateral dyke propagation observed in many volcanoes, and corroborate well the theoretical analyses of Pinel and Jaupart (2000, 2004).

Rapidly constructed topographic loads like volcanoes can be unstable and sectors of an edifice can tend toward collapse. Walter and Troll (2003) used gelatine experiments to investigate the effect of a volcano sector instability on the formation of dyke swarms (Fig. 11b). At the base of a gelatine edifice, they simulated a

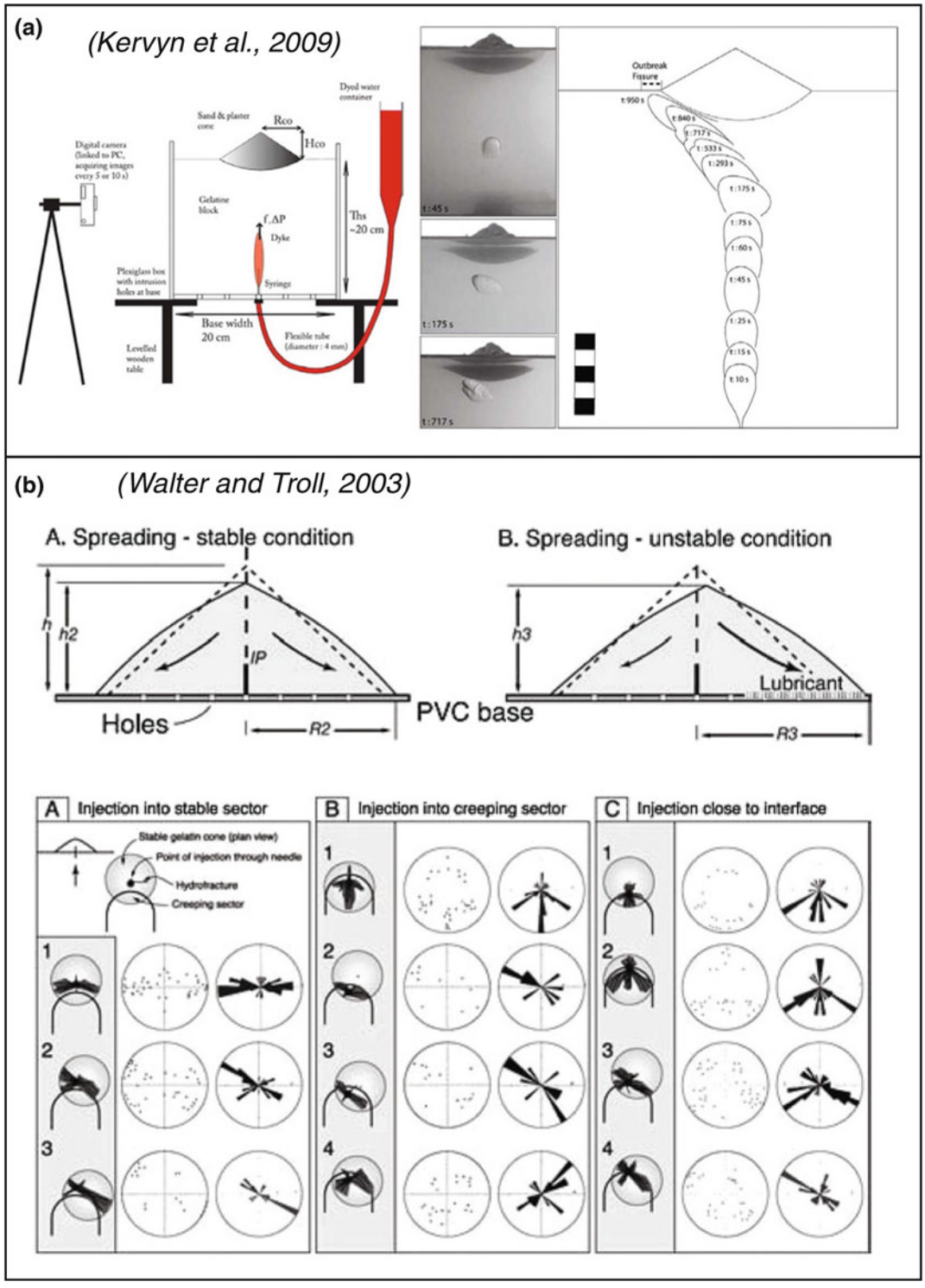
(a)
(Kervyn et al., 2009)
Dyed water container
Sand & plaster cone
Rco
Hco
Digital camera (linked to PC, acquiring images every 5 or 10 s)
Gelatine block
f, ΔP
Dyke
Ths ~20 cm
Plexiglass box with intrusion holes at base
Syringe
Base width 20 cm
Flexible tube (diameter : 4 mm)
Levelled wooden table
t : 45 s
t : 175 s
t : 717 s
Outbreak Fissure
t : 950 s
t : 840 s
t : 717 s
t : 533 s
t : 293 s
t : 175 s
t : 75 s
t : 60 s
t : 45 s
t : 25 s
t : 15 s
t : 10 s
(b)
(Walter and Troll, 2003)
A. Spreading - stable condition
B. Spreading - unstable condition
h
h2
IP
Holes
R2
h3
1
Lubricant
PVC base
R3
A Injection into stable sector
Stable gelatin cone (plan view)
Point of injection through needle
Hydrofracture
Creeping sector
B Injection into creeping sector
C Injection close to interface

◀ **Fig. 11** **a** Experimental study of Kervyn et al. (2009), in which an water-filled or an air-filled dyke was injected into a gelatine model, at the surface of which was a volcanic edifice made of sand. *Left* Drawing of experimental setup. *Centre* Time series photographs of a characteristic experiment of dyke rising under a volcanic edifice. *Right* Evolution of the dyke outline illustrating that the dyke rise velocity decreases when approaching the cone base. **b** Experimental study of Walter and Troll (2003), in which dyed water was injected into a volcanic edifice made of gelatine. *Top* Geometry of experimental cones in stable situation (*A*) and unstable situation (*B*). Due to gravity, the cones spread outward, partially sliding on a basal lubricant. In the unstable situation, only one flank was lubricated. *IP* injection point (10 mm above base), basal radii $R_3 > R_2 > R_1$; cone height $h > h_2 > h_3$. Through small holes drilled in the basal plate, injection was possible at various positions. *Bottom* Summarized arrangement of hydro-fractures propagating in locally destabilized edifices relative to injection point and eccentricity of a creeping sector. *A* Injection into stable sector. *B* Injection into creeping sector. *C* Injection close to the interface stable/unstable sector. Stereoplots illustrate the statistic orientation of fractures: each black dot in pole plots refers to the distal locality of an experimental fracture, measured in azimuth and distance from the point of injection. In frequency–azimuth (rose) diagrams (polar lines, sector size = 8°), the length of each rose sector is proportional to the frequency of orientation that lies within that sector (Walter and Troll 2003)

localised décollement, above which the sector of the edifice was considered unstable. They showed that: (i) injection into the stable sector of the edifice results in two main radial dyke swarms, (ii) injection into the unstable sector of the edifice results in swarms reflecting the extent of the unstable sector, and (iii) injection close to the transition between the stable and the unstable sectors mainly produce three swarms, two of which follow the stable/unstable discontinuity. These results corroborate geological observations from volcanic centres exhibiting triaxial rift zones, such as Tenerife, Canary Islands (e.g. Delcamp et al. 2012a).

Sector instability and sliding have been linked with active intrusion or the presence of intrusive complexes at several volcanoes. Models studying the interaction between gravitational instability and intrusions have been conducted by Mathieu and van Wyk de Vries (2009), Delcamp et al. (2012b), and by Norini and Acocella (2011). Mathieu and van Wyk de Vries (2009) modelled the development of the Mull centre in Scotland, showing how large intrusions could develop dykes along gravity slides. Delcamp et al. (2012b) found that dykes would propagate out of a central intrusion into rift zones and applied their models to the distribution of inclined dykes and intrusive bodies on La Reunion Island, France. Norini and Acocella (2011) used a combination of high viscosity silicone and low viscosity oils to study the relationship between magma intrusion, gravity sliding and tectonic extension at Mt. Etna, Italy. They conclude that the magmatic forcing and gravity effects greatly outweigh the regional tectonics in controlling intrusion and instability on Mt. Etna.

4.1.6 Interaction of Coevally Propagating Dykes

Laboratory experiments enable the emplacement of several coeval dykes to see how they interact. It is expected that the stress field induced by propagation of one dyke would influence the propagation of another (Delaney and Pollard 1981). Takada (1994a, b) carried out gelatine experiments, in which he injected two coeval dykes. The experiments show that: (i) two propagating liquid-filled cracks are likely to coalesce; (ii) a propagating liquid-filled crack is unlikely to coalesce with a nearby solidified crack; (iii) large regional differential stresses impede the coalescence of magma-filled cracks, and control the formation of parallel dykes; (iv) a large magma supply rate can produce a complete stress field rearrangement that overcomes the regional stress field, leading to the formation of radial dykes, as observed in many exhumed volcano plumbing systems (Odé 1957; Nakamura 1977).

In other gelatine experiments, Ito and Martel (2002) tested the effect of the critical dyke spacing x_c on dyke interaction: if the distance x between the dykes is smaller than x_c, the dykes coalesce, whereas if $x > x_c$, the dykes do not coalesce (Fig. 12). Also, increasing the regional differential stress reduces the value of x_c. The experiments show that when regional differential stresses are small, x_c scales with only a few times

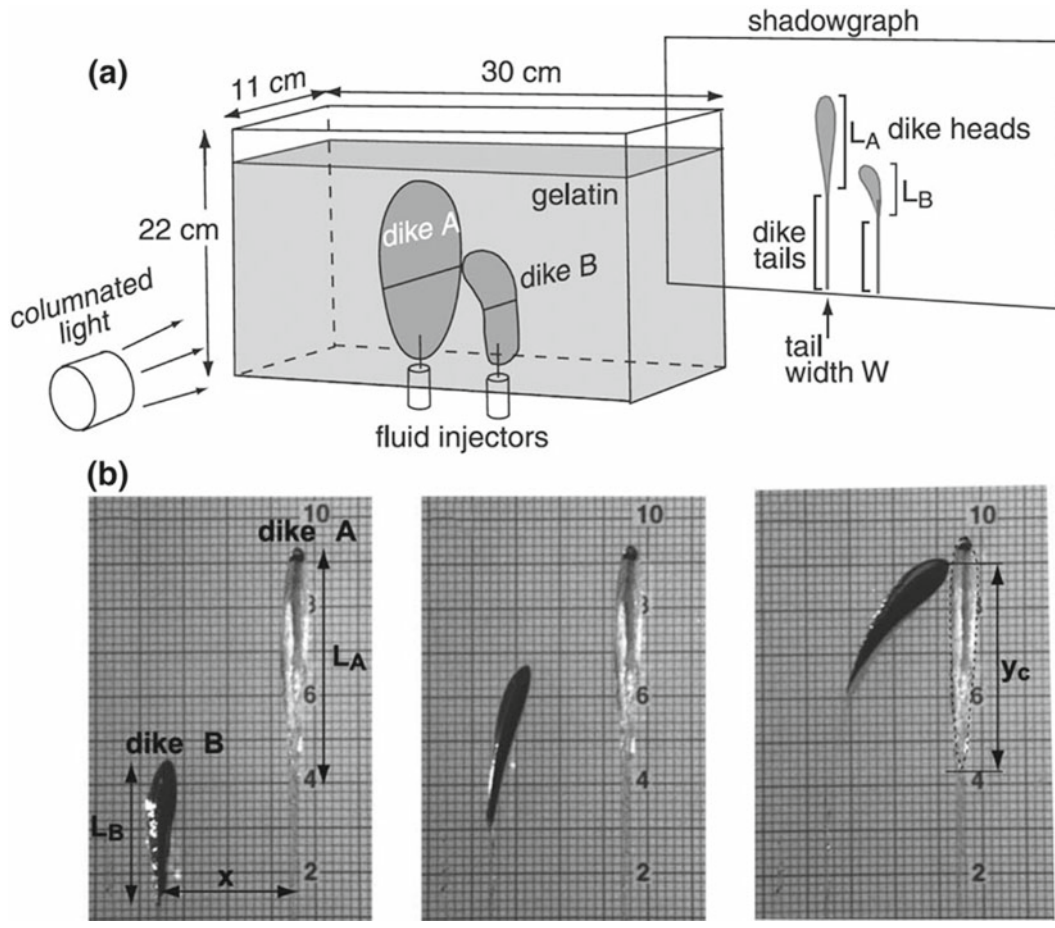

Fig. 12 **a** Schematic drawing of the experimental setup of Ito and Martel (2002) for studying dyke interactions. **b** Time series of photographs of a characteristic experiment illustrating the interaction and coalescence of two propagating parallel dykes

the dyke height, i.e. dyke interaction can potentially focus magma transport over large vertical distances. Such a process can help explain the critical distance observed between volcanoes at the Earth's surface, even though these volcanoes are fed from broad melting zones in the mantle.

4.1.7 Inelastic Processes Associated with Dyke Propagation

With gelatine experiments, one assumes that the model host rock behaves as a nearly purely elastic solid, and that dykes propagate according to the Linear Elastic Fracture Mechanics (LEFM) theory. Nevertheless, field observations (Mathieu et al. 2008; Kavanagh and Sparks 2011; Daniels et al. 2012) suggest that host rock behaviour during dyke emplacement is substantially inelastic. Such inelastic processes can be addressed in laboratory models made of cohesive granular materials.

The experiments of Mathieu et al. (2008) and Kervyn et al. (2009), which use ignimbrite powder and Golden Syrup, show qualitatively that shear bands form at the tips of propagating dykes, leading to the splitting of the dyke tips to form V-shaped (cup-shaped) intrusions. Such dyke tip splitting has also been observed in the 3D experiments of Galland et al. (2009) and Galland (2012), which used silica flour and vegetable oil. These results suggest that dykes may propagate as viscous indenters, where the

viscous material penetrates the cohesive granular material like a chisel pushed into plaster or a spade pushed into the ground (Donnadieu and Merle 1998), rather than as a simple mode I fracture, particularly if the host rock cohesion is relatively low. Quantitative 2D experimental results of Abdelmalak et al. (2012) (Fig. 13a) further show that: (i) small-scale reverse shear bands form at the vicinity of the propagating dyke tip, and (ii) the model surface lifts up due to dyke emplacement (Fig. 13b). These two observations are incompatible with the LEFM theory, and the results suggest that models made of cohesive granular materials may provide important insights into the complex mechanics governing dyke emplacement in low strength rock masses. Given that these models have been designed only recently, they offer broad possibilities for future experimental studies of dyke emplacement.

4.1.8 Effects of Cooling on Dyke Propagation

A critical aspect of magma intrusion is the effect of cooling, which is usually neglected in laboratory experiments (e.g., Galland et al. 2009), because it is technically challenging to control. Taisne and Tait (2011) performed experiments in which they injected a wax into a model made of gelatine; the gelatine temperature was lower than the solidus temperature of the wax. The temperature difference between the injected wax and the host gelatine was varied, as was the balance between the heat injected into the system and the heat diffusing from the wax into the gelatine host. Three main behaviours were observed: (i) when the injected wax temperature was large compared to its solidus temperature, and when the heat influx was large compared to the diffusive heat loss, the dyke propagated continuously, like a non-solidifying dyke; (ii) when the injected wax temperature was close to its solidus temperature, and when the heat influx was small compared to the diffusive heat loss, the dyke did not propagate; (iii) when the wax temperature and the heat fluxes lay between the above end members, the dyke propagates in a stepwise, intermittent, manner due to local clogging of the dyke tip. This intermittent behaviour may help explain the occurrence of seismic bursts recorded during dyke emplacement in volcanoes (Hayashi and Morita 2003; White et al. 2011) as a consequence of the thermo-mechanical interaction of the dyke and its host rocks.

4.2 Cone Sheet Emplacement

Cone sheets are prominent features in many volcanoes on Earth. In eroded volcanoes, these sheet-like intrusions strike concentrically about and dip in toward the volcano centre, and they commonly occur as dense swarms. Like dykes, they are typically discordant to any mechanical stratigraphy in their host rocks. A classic example of a cone sheet swarm is found in the Ardnamurchan intrusive complex, NW Scotland (Richey et al. 1930; O'Driscoll et al. 2006; Burchardt et al. 2013). Other good examples are found in the Canary Islands (Ancochea et al. 2003), Galápagos Islands (Chadwick and Howard 1991; Chadwick and Dieterich 1995), and Iceland (e.g. Schirnick et al. 1999; Walker 1999; Klausen 2004; Burchardt et al. 2011).

Despite the prominence of cone sheets, little is known about their much-debated emplacement mechanisms (e.g. Phillips 1974; Klausen 2004; Burchardt et al. 2013). One reason is that laboratory cone sheets rarely occur in gelatine experiments, which mostly simulate either dykes (Takada 1990; Lister and Kerr 1991; Dahm 2000; Rivalta and Dahm 2006; Le Corvec et al. 2013) or sills (Kavanagh et al. 2006; Menand 2008). To our knowledge, the only cone sheet-like intrusions recorded in gelatine models developed from a pressurised cavity simulating a magma reservoir (McLeod and Tait 1999) (Fig. 8a; see Sect. 4.1). Theoretical studies suggest that shear failure, absent in gelatine experiments, might be important for cone sheet formation (Phillips 1974). Indeed, experiments using cohesive granular materials, which undergo shear failure, have produced dykes and/or cone sheets (Mathieu et al. 2008; Galland et al. 2009) (Fig. 14).

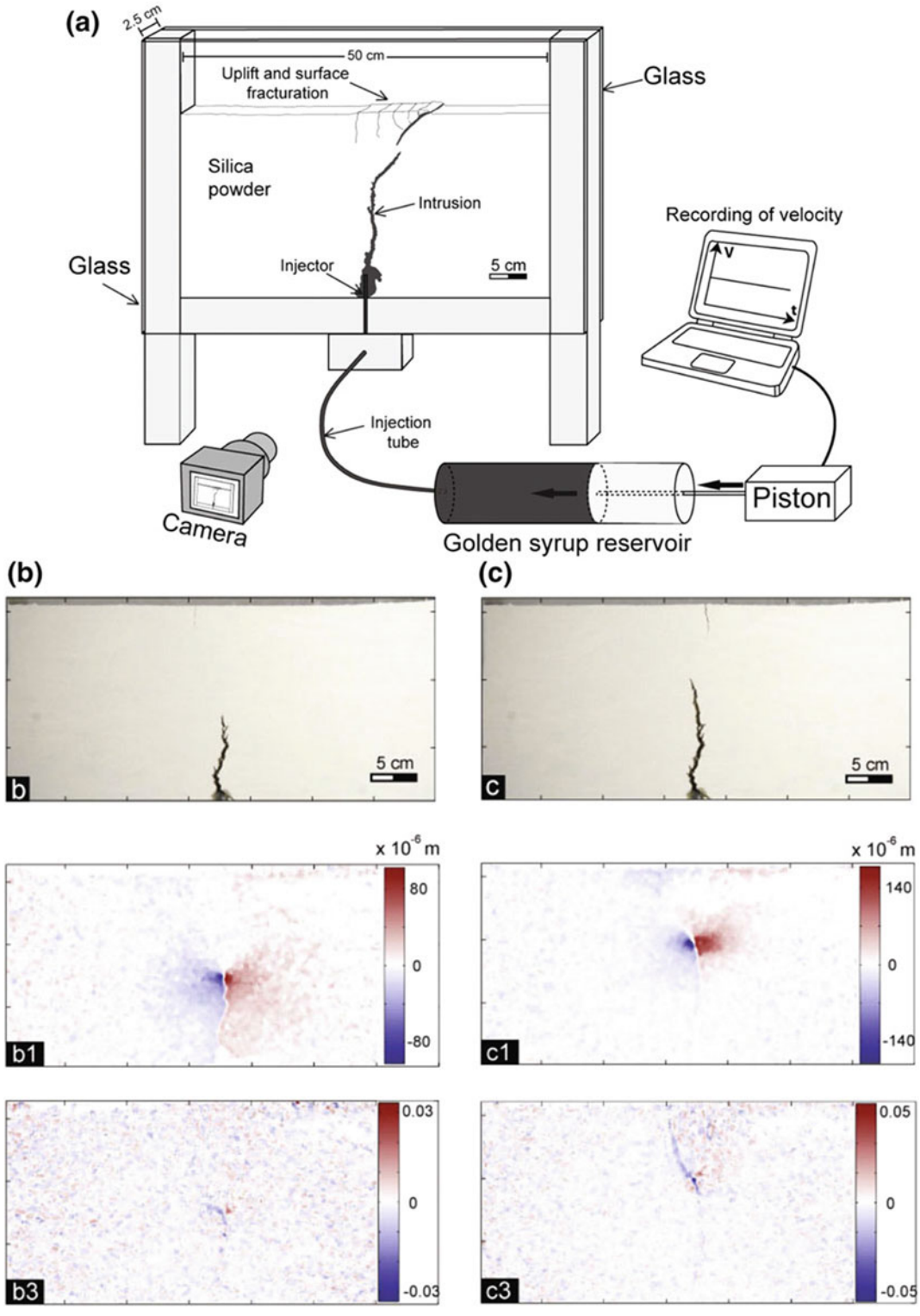
(a)
2.5 cm
50 cm
Uplift and surface fracturation
Glass
Silica powder
Intrusion
Recording of velocity
Glass
Injector
5 cm
v
t
Injection tube
Camera
Piston
Golden syrup reservoir
(b)
(c)
5 cm
b
5 cm
c
x 10-6 m
80
0
-80
b1
x 10-6 m
140
0
-140
c1
0.03
0
-0.03
b3
0.05
0
-0.05
c3

◀ **Fig. 13** **a** Experimental setup of Abdelmalak et al. (2012) designed to study the small-scale deformation induced by dyke emplacement. The experiments are 2D, such that the propagation of the dyke was monitored from the side of the box with digital camera. The resulting images were processed using Digital Image Correlation algorithm to compute the displacement field associated with dyke emplacement. **b** Photograph (*top*), horizontal displacement field (*middle*) and strain field (*bottom*) of an experimental dyke during experiment. The strain field highlights small-scale shear bands rooted at the tip of the dyke. **c** Photograph (*top*), horizontal displacement field (*middle*) and strain field (*bottom*) of an experimental dyke during the same experiment than in **b**, but later. The strain field showed that substantial shear bands connected the dyke tip to the model surface. These experimental results suggest that dykes propagate as a viscous indenter, not as linear elastic hydraulic fracture

Galland et al. (2014a) recently identified two dimensionless numbers that control the formation of either cone sheets or dykes in such cohesive granular materials (Fig. 14a). The first number Π_1 is a geometric ratio between the depth of emplacement and the width of the magmatic source. The second number Π_2 is a dynamic ratio between the viscous stresses within the flowing magma and the strength (cohesion) of the host rock. Plotted in a dimensionless phase diagram with Π_1 and Π_2 as the vertical and horizontal axes, respectively, the experimental data define dyke and cone sheet regimes in a phase diagram, separated by a transition that fits a power law (Fig. 14a). This result shows that cone sheets preferentially form (i) from shallow magma feeders (small value of Π_1), in agreement with the results of Mathieu et al. (2008), and (ii) when magma is viscous, or when the injection velocity is high, and/or when the host rock is weak (large value of Π_2).

This experimental phase diagram (Fig. 14a) also explains why gelatine experiments rarely simulate cone sheets: the large cohesion of the gelatine generally leads to small values of Π_2, i.e. in the dyke field of the phase diagram. In the exceptional gelatine experiments of McLeod and Tait (1999), the cavity from which cone sheets formed was large and shallow (Fig. 8a), corresponding to small values of Π_1, i.e. to the cone sheet field of the phase diagram.

These 3D experiments with cohesive granular materials did not allow for imaging the small-scale processes controlling the formation of dykes versus cone sheets, given that processes at work are buried and thus invisible. Such a limitation is overcome by using '2D' experiments, whereby the intrusion propagates upward against a glass plate (Fig. 14b) (Mathieu et al. 2008; Abdelmalak et al. 2012; Mourgues et al. 2012). This allows the growth of sheet intrusions to be monitored directly. Boundary effects from the glass plate are found to be minimal. Abdelmalak et al. (2012) and Mourgues et al. (2012) applied Digital Image Correlation (DIC) to photographs of their experiments to quantitatively map the small-scale 2D deformation field induced by intrusion (Fig. 13). In good agreement with the conclusions of Mathieu et al. (2008) and Kervyn et al. (2009) (Fig. 14b), their results show that dykes propagating towards the model surface can trigger the formation of shear fractures, which control the formation of V-shaped sheet intrusions. This supports the hypothesis of Phillips (1974) that cone sheet emplacement is mainly controlled by shear failure in the host rocks.

4.3 Sill Formation

Igneous sills are another form of sheet intrusion that is very common in the Earth. Unlike dykes or cone sheets, to which they are nonetheless closely related, sills are typically concordant with the mechanical stratigraphy in their host rocks. Igneous sills represent substantial volumes of volcanically-influenced sedimentary basins, good examples being the Karoo Basin, South Africa (Chevallier and Woodford 1999; Svensen et al. 2012), and the North Atlantic volcanic margins (e.g. Vøring and Møre Basins, off Norway; Berndt et al. 2000; Planke et al. 2005). Their emplacement likely triggered the release of gigantic volumes of greenhouse and poisonous gases in the atmosphere, leading to mass extinctions (Svensen et al. 2004, 2007). In addition, sills have a large impact on petroleum systems as (i) they provide heat that enhances the

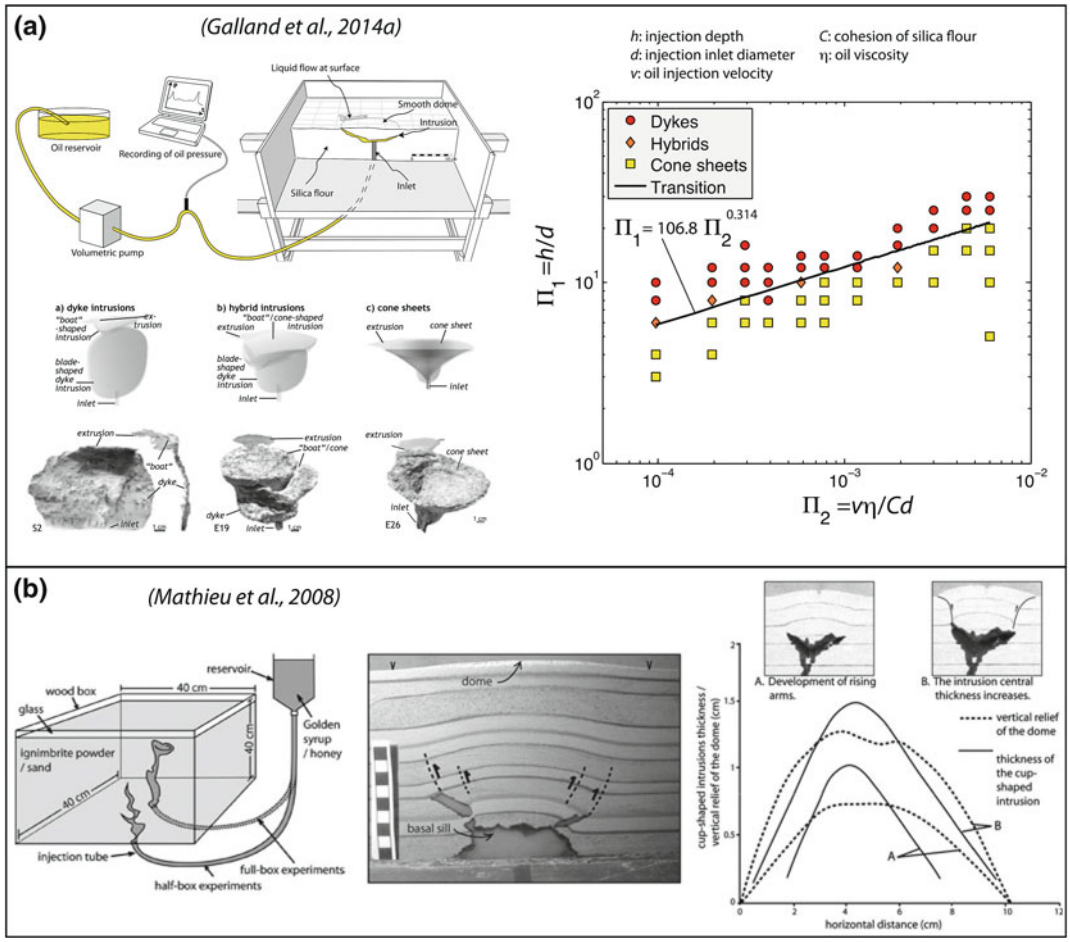

Fig. 14 Characteristic experimental studies of cone sheet emplacement. **a** Experimental setup (*upper left*), typical modelled intrusions (*lower left*) and experimental phase diagram (*right*) of the experimental study of Galland et al. (2014a), which used fine-grained silica flour and molten vegetable oil. The apparatus allows flow rate-controlled injection of the oil, and pressure measurements. Varying systematically the depth of injection (h), the diameter of the injection inlet (d) and the injection fluid velocity (v), the models produced dykes, cone sheets or hybrid intrusions. Plotting the experiments in a phase diagram with $\Pi_1 = h/d$ and $\Pi_2 = v\eta/Cd$ as y- and x-axes, respectively, the dykes and cone sheets group in two fields, separated by a transition that fits a power law. Notice that the hybrid intrusions always plot between the dyke and cone sheet fields. Here, η and C are the oil viscosity and flour cohesion, respectively. **b** Experimental setup (*left*), cross section of a typical model (*centre*) and measurements (*right*) of the experimental study of Mathieu et al. (2008) using ignimbrite powder and Golden Syrup. This experimental apparatus allows pressure-controlled injection of Golden Syrup. The cross section exhibits the main features obtained in the models of Mathieu et al. (2008), which are V-shaped conduits connected to shear bands, these later being at the edges of a dome structure in the intrusion's overburden. The graph on the *right* exhibits comparison between the along-strike thickness of the V-shaped intrusions and the amplitude of the overlying dome, showing a non-simple relationship between them

maturation of organic matter in surrounding rocks (e.g. Aarnes et al. 2011a, b), (ii) they generate dome structures (also called forced folds) in their overburden strata (e.g. Trude et al. 2003; Hansen and Cartwright 2006b; Jackson et al. 2013; van Wyk de Vries et al. 2014, Magee et al. 2014) that can be hydrocarbon traps (Polteau et al. 2008b), and (iii) cooling and solidification of the magma triggers intense fracturing of the solidified sills, which can be excellent

hydrocarbon reservoirs (Rossello et al. 2002; Rodriguez Monreal et al. 2009; Witte et al. 2012).

4.3.1 Formation of Sills from Vertically-Propagating Dykes

For many decades, it had been assumed that sills were emplaced from dykes that stalled in their ascent and intruded along a level of neutral buoyancy (LNB) (e.g. Francis 1982; Lister and Kerr 1991). However, no laboratory models have managed to simulate sill emplacement as fed from a dyke along a LNB; instead, a feeder dyke reaching a LNB stops propagating upwards and starts propagating laterally with dip unchanged (Lister and Kerr 1991). All laboratory experiments that simulated the emplacement of sills required the presence of mechanical layering of the host, i.e. layers of different strengths, such as is commonly observed in sedimentary basins and volcanic sequences.

In pioneering gelatine experiments by Pollard and Johnson (1973) and Hyndman and Alt (1987), sills formed from a dyke either (i) along a weak interface between two gelatine layers of similar strength (Pollard and Johnson 1973), or (ii) at the base of a gelatine layer that is stronger than the underlying layer (Hyndman and Alt 1987). Kavanagh et al. (2006) and Menand (2008) later conducted more quantitative experiments with water injected at constant pressure (Fig. 15a). These authors systematically varied: (i) the input pressure scaled by the resisting pressure (i.e. the pressure required to propagate a crack of given size) and (ii) the rigidity contrast between upper and lower gelatine layers.

All experiments started with a vertical dyke propagating upward to the interface between the two gelatine layers. Several behaviours were then observed (Fig. 15a).

With a more rigid lower layer, the dyke always simply propagated through the upper layer and never turned into a sill. With a more rigid upper layer and a strong interface, the dyke was arrested. With a more rigid upper layer and a weak interface, two varieties of sills were obtained. First, with a high rigidity contrast between the layers and with a high driving pressure, the dyke completely turned into a sill. Second, with a low rigidity contrast between the layers and with a low driving pressure, a hybrid intrusion formed that comprised a dyke in the upper layer and a sill along the interface. These experiments therefore can explain the transition of dykes into sills at layers in the host rock as a consequence of particular combinations of rigidity or strength contrasts between layers, of the strength of the interface between the layers, and of the driving pressure in the magma.

4.3.2 Formation of Saucer-Shaped Sills

Seismic data (Thomson and Hutton 2004; Planke et al. 2005; Hansen and Cartwright 2006a; Thomson 2007; Hansen et al. 2008) and geological observations (Chevallier and Woodford 1999; Polteau et al. 2008a, b), show that from their initiation point at a flat layer interface, sills can develop segments that cut up at an angle through the layering and then flatten again. This gives the sheet-intrusion a peculiar saucer-like shape. A correlation between their diameters and depths led Malthe-Sørenssen et al. (2004) to suggest that saucer shaped sills result from a mechanical interaction with the deformable free surface during sill growth.

Galland et al. (2009) and Galland (2012) tested this hypothesis by using models made of silica flour and vegetable oil (Fig. 15b). The oil was injected directly along a flexible net that simulated a horizontal sedimentary layer. The oil initially formed a sub-circular sill along the layer. The model surface subtly lifted up above the sill, forming a smooth sub-circular dome, or forced fold (Hansen and Cartwright 2006b; Jackson et al. 2013; Magee et al. 2014). Finally, the oil erupted, always at the edge of the dome. After solidification, a saucer-shaped intrusion was excavated (Fig. 15b), the flat inner sill being under the dome centre, and the inclined sheets being under the dome edges. Galland et al. (2009) showed that the diameter of the inner sill correlated well with the depth of injection, i.e. the transition from horizontal to inclined intrusion is depth-controlled (Fig. 15b). In good

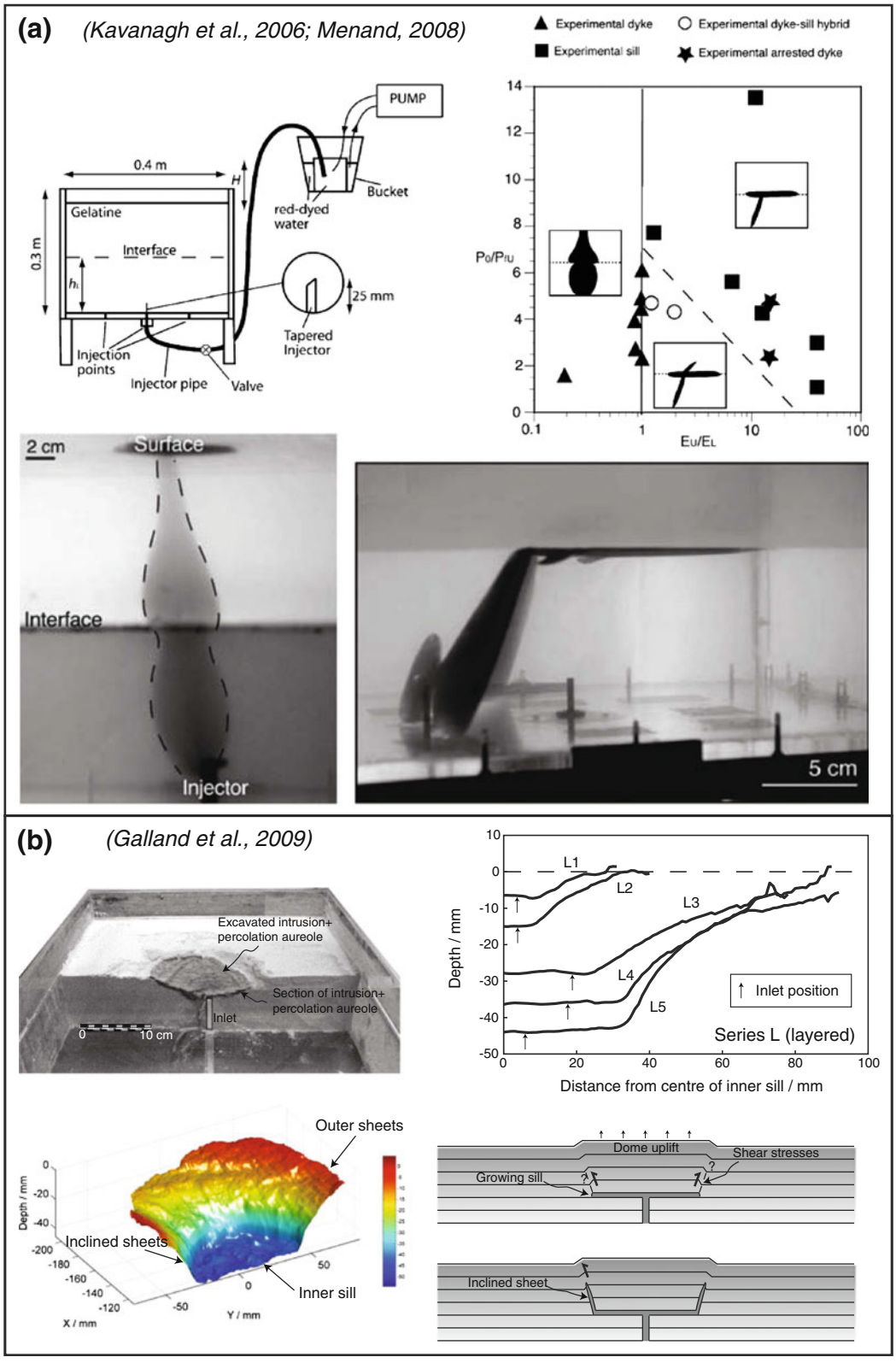
(a)
(Kavanagh et al., 2006; Menand, 2008)
Experimental dyke
Experimental dyke-sill hybrid
Experimental sill
Experimental arrested dyke
PUMP
0.4 m
H
Bucket
red-dyed water
Gelatine
Interface
0.3 m
h
25 mm
Tapered Injector
Injection points
Injector pipe
Valve
P0/PfU
EU/EL
2 cm
Surface
Interface
Injector
5 cm
(b)
(Galland et al., 2009)
Excavated intrusion+ percolation aureole
Section of intrusion+ percolation aureole
Inlet
0
10 cm
Depth / mm
L1
L2
L3
L4
L5
Inlet position
Series L (layered)
Distance from centre of inner sill / mm
Outer sheets
Inclined sheets
Inner sill
X / mm
Y / mm
Dome uplift
Shear stresses
Growing sill
Inclined sheet

◀ **Fig. 15** **a** Experimental study of Kavanagh et al. (2006) and Menand (2008) on sill emplacement in layered media, here made of gelatine. Setup for pressure-controlled intrusion (*upper left*), characteristic experimental dyke (*lower left*) and dyke-fed sill (*lower right*), and experimental phase diagram showing the parameters controlling the formation of dykes, sills, hybrid dyke-sills, or arrested dykes in layered media (*upper right*). Here E_U and E_L denote the Young modulus of the upper and lower layers, respectively, and P_0 and P_{fU} denote the water overpressure and the fracture pressure (i.e. the strength) of the upper layer. **b** Experimental study of Galland et al. (2009) and Galland (2012) on the emplacement of saucer-shaped sills, using silica flour and vegetable oil. The experimental setup is displayed in Fig. 14. Experimental box exhibiting excavated solidified intrusion (*upper left*), 3D model of an excavated experimental saucer-shaped sill (*lower left*), averaged profiles of experimental saucer-shaped sills emplaced at various depths (*upper right*), and conceptual model of saucer-shaped sill emplacement (*lower left*). The averaged profiles show that saucer-shaped sills are larger when they are deeper

agreement with the numerical results of Malthe-Sørenssen et al. (2004) and the theoretical analysis of Goulty and Schofield (2008) and Galland and Scheibert (2013), these experiment results demonstrate how shallow intrusions dynamically interact with the free surface. As a shallow sill grows laterally, it deforms its overburden by doming. When the sill reaches a critical diameter, shear stresses at the edges of the dome deflect the crack tip and so initiate an inclined sheet (Fig. 15b). This scenario illustrates that the free surface exerts a positive mechanical feedback on a growing intrusion.

While some saucer-shaped sills are perfectly circular, others are markedly elliptical (Chevallier and Woodford 1999). Galerne et al. (2011) tested the hypothesis that elliptical saucer-shaped sills result from the planar geometry of a feeder dyke. They performed experiments with either pipe-like or planar injection inlets, and found that the former leads to sub-circular sills, whereas the latter leads to elliptical sills. The long axis of the elliptical sills is superimposed on the trace of the planar feeder dyke, in very good agreement with geological observations (Galerne et al. 2011). The 3-dimensional form of saucer-shaped sills therefore reflects the geometry of their feeders.

4.3.3 Effects of Cooling on Sill Emplacement

As for dykes, cooling effects are neglected in most past studies of sill emplacement. However, Chanceaux and Menand (2014) recently adopted Taisne and Tait's (2011) approach (see #4.1.8 above) to investigate thermal controls on sill initiation. In these experiments, a molten vegetable oil was injected at a controlled temperature into a gelatine host made of two layers. The experiments highlight various behaviours of the intruding oil according to the dimensionless temperature, $\theta = (T_s - T_g)/(T_i - T_g)$, where T_s is the solidification temperature of the intruding fluid, T_g is the temperature of the host and T_i is the temperature of the injected fluid. When both θ and injection flux are low, solidification effects are extreme and so intrusion is inhibited. When θ and injection flux are high, solidification effects are limited and dykes pass through the interface between the two layers of gelatine. For intermediate values of θ and injection flux, either dykes terminate at the interface (high solidification effect) or else sills form along it (moderate solidification effect).

4.4 Laccoliths, Stocks and Cryptodomes

Laccoliths are igneous intrusions exhibiting a flat lower margin and a domed, convex upper margin. The Henry Mountains of Utah are the classic type locality (Gilbert 1877; Johnson and Pollard 1973; Pollard and Johnson 1973; Jackson and Pollard 1990; de Saint-Blanquat et al. 2006; Morgan et al. 2008), where multiple stacks of laccoliths have developed in individual magmatic centres. Laccoliths in Elba, Tuscany and in Central Europe are other good examples (Rocchi et al. 2002; Breitkreuz and Mock 2004; Westerman et al. 2004). In most cases, laccoliths are intrusions emplaced at shallow depth into layered sedimentary rocks. Laccoliths tend to be thick in relation to their width, compared with sills and saucer-, or cup-shaped intrusions (Corry 1988; Bunger and Cruden 2011). The host rock around a laccolith is typically

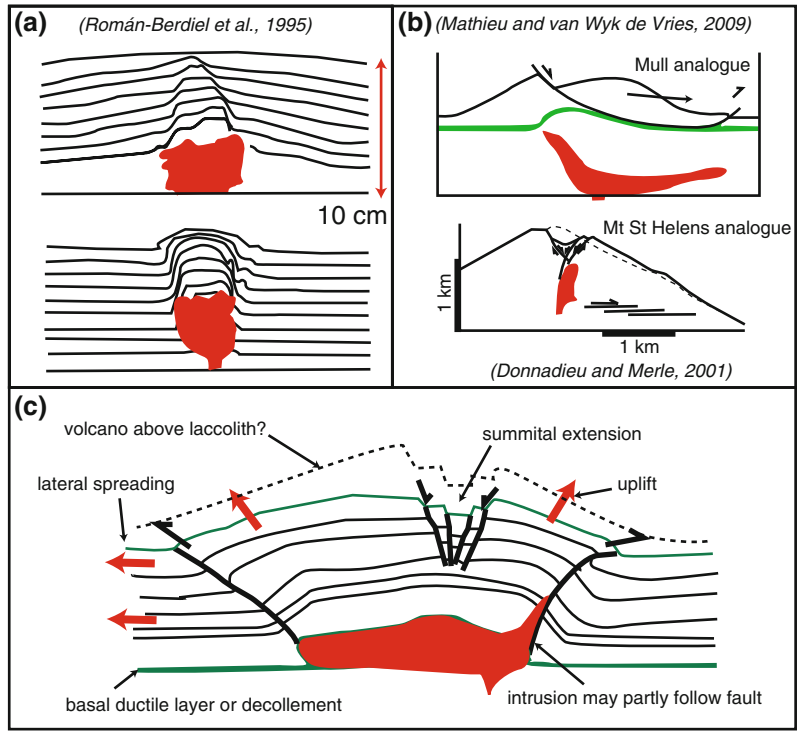

Fig. 16 **a** Analogue model cross sections of a laccolith from Román-Berdiel et al. (1995). **b** Laccolith-like intrusion schematic cross-section from Mathieu and van Wyk de Vries (2009) and steep cryptodome intrusion modelled by Donnadieu and Merle (2001) for Mt. St. Helens. **c** Cross-section of the generalised features of a laccolith intrusion developed from analogue models studies, showing the uplift caused by the intrusion and possible lateral spreading

domed, and often at least one, usually steep, side of the laccolith exhibits faulting that also accommodates uplift of the host rock (Fig. 16).

Stocks are steep sided, vertically-elongated intrusions that have roughly equal horizontal dimensions and that truncate any mechanical stratigraphy in the host rock. The term cryptodome refers to a viscous laccolithic or stock-like intrusion that remains hidden below the updomed overburden. The development of cryptodomes may culminate in eruption of typically highly viscous silicic lava, either effusively as in the Showa-Shinzan uplift and dome at Usu Volcano, Japan (Corry 1988; Breitkreuz and Mock 2004) or explosively as in the 1980 eruption of Mt. St. Helens, U.S.A (Lipman et al. 1981).

4.4.1 General Development of Laccolith Emplacement and Controls from Host Rock Layering

The first systematic experimental investigation of laccolith emplacement was carried out by Dixon and Simpson (1987). Their experiments ran in a centrifuge; the model magma was silicone putty, which was injected at the base of elastoplatic parafin layers. The experiments allowed for reconstructing the time sequence of laccolith emplacement: (i) a sill forms between two layers; (ii) the sill spreads and thickens as the overburden bends upward; (iii) the overburden kinks above the laccolith tip and eventually fails. Dixon and Simpson (1987) showed that the bending phase is enhanced by thicker and stronger overburden, as expected by theory (e.g. Pollard and Johnson 1973; Galland and Scheibert 2013).

The experiments of Román-Berdiel et al. (1995), who simulated the emplacement of a laccolith along a ductile layer below a brittle overburden, produced similar results (Fig. 16a). Using silicone for both magma and the ductile layer, and sand for the brittle overburden, they found that: (i) a critical thickness of ductile layer for laccolith formation was reduced with increasing overburden thickness; (ii) laccolith height to width ratio decreased with increasing thickness of overburden (i.e. deeper laccoliths are flatter); (iii) and the laccolith diameter was also linked to overburden

thickness. They also noted that asymmetric laccoliths could be linked to synchronous gravitational sliding along the ductile layer. Intrusion of silicone in the absence of a ductile layer produced piercing, stock-like intrusions, rather than laccoliths (see also Acocella et al. 2001).

4.4.2 Controls of Regional Tectonics or Gravitational Spreading on Laccolith Emplacement

Benn et al. (1998, 2000) modelled granitic intrusion within a transpressive tectonic regime by using similar materials to Román-Berdiel et al. (1995). Their models also produced laccoliths on which thrust faults nucleated to accommodate both the intrusion-related inflation and the regional-tectonic deformation. They again found that laccoliths formed at greater depths were flatter. Using different materials (cohesive silica flour and vegetable oil), Galland (2005) produced laccoliths at the interface between two brittle layers of different cohesions, without requiring a ductile layer like in the experiments of Román-Berdiel et al. (1995). The laccoliths in the above three studies all have a domed overburden that is uplifted on a shear zone that surrounds the intrusion and has a reverse slip sense. This doming leads to extension and normal faulting on the apex of the dome (Fig. 16b, c). In addition, the experiments of Galland et al. (2007a) show that compressional tectonics are likely to enhance the uplift of the laccolith's roof, and so greatly control the final thickness of laccoliths.

If the surface and overburden can move laterally to accommodate intrusion, as in a volcano flank or in gravitational spreading, then a laccolith can also easily develop. This association of intrusion with large-scale lateral deformation was studied by Merle and Vendeville (1995). They injected silicone putty into a sand pack contained between glass walls and constrained by a fixed wall on one side. The models produced extensive lateral movement and thrusting that accommodated magma emplacement far from the point of intrusion. Subsequently, Mathieu et al. (2008) and Delcamp et al. (2012b) explicitly modelled magma intrusion into spreading volcanic edifices (Fig. 16b). In their models, a basal silicone layer below the volcanic edifice was intruded by a Golden syrup magma analogue. These models produced laccolith-like intrusion shapes, as would be predicted for these conditions by Román-Berdiel et al. (1995), and were characterised by considerable edifice and substrata deformation. These models raise the possibility that some laccoliths may propagate by lateral spreading as well as by vertical uplift.

4.4.3 Formation of Stocks or Cryptodomes

Donnadieu and Merle (1998) intruded silicone putty into sand cones, and produced cryptodomes or stocks that caused considerable surface deformation (see Fig. 22a). In these models, and in those of Román-Berdiel et al. (1995), Román-Berdiel (1999), Mathieu et al. (2008) and Galland (2005), there was no ductile stratum to intrude into and the viscosity of injected silicone was high relative to the host material strength. As a result, the intrusions formed in a viscous indenter style on reverse and normal faults that developed synchronously with intrusion into the edifice.

4.4.4 The Roles of Magma Viscosity and Host Rock Strength in the Formation of Laccoliths, Stocks and Cryptodomes

The scaled viscosity in which the analogue laccolith or stock-like intrusions have been formed is significantly higher than those of sills and saucer-shaped intrusions. Equally, in natural cases laccoliths are overwhelmingly produced with intermediate to felsic magmas. Thus, viscosity is a critical controlling factor on the type of intrusion (see Galland et al. 2014a). If the magma is of low viscosity it will tend to form a thin sill, and then it will intrude fractures climbing towards the surface to create saucers (Galland et al. 2009). If the magma is of high viscosity, it will tend to propagate less rapidly along décollements and fractures, and will tend to uplift the host rock. If this uplift predominates over lateral or included injection, a laccolith or a stock like intrusion will

develop. In addition, magma cooling at the margins may seal the edges, increasing uplift, and multiple pulses may be trapped below or within the growing intrusion (e.g. Torres del Paine Laccolith; Michel et al. 2008).

In addition to a relatively viscous magma, the general conditions for the formation of laccoliths and stock-like (cryptodome) intrusions, as established by analogue modelling, include a relatively weak host rock and a shallow emplacement depth (a few hundred metres to a few kilometres below the surface). The key condition controlling which intrusion type forms is the presence (or absence) of mechanical layering of the host rock, with laccoliths favoured by the presence of weak interfaces or ductile layers of sufficient thickness. Both intrusion types develop by roof uplift.

4.5 Caldera-Related Structures and Intrusions

Collapse calderas are enclosed volcano-related topographic depressions of >1 km diameter that have typically sharply-defined, steep walls and nearly flat bottoms (Lipman 1997) (e.g. Fig. 17). They occur in all volcanic settings on Earth and other planets and with all magma types (e.g. Crumpler et al. 1996; Geyer and Martí 2008; Hansen and Olive 2010). Both ancient geological evidence and recent observations from active volcanoes indicate that calderas form through subsidence of the roof of a sub-surface magma body, as a consequence of magma withdrawal from that body (Fouqué 1879; Verbeek 1884; Clough et al. 1909; Williams 1941; Smith and Bailey 1968; Druitt and Sparks 1984; Lipman 1984, 1997; McBirney 1990; Geshi et al. 2002; Cole et al. 2005; Michon et al. 2011). Subsidence usually occurs along a ring fault; magma may intrude this fault to form a ring dyke and may ultimately erupt from it. Caldera collapse may thus lead to the partial or complete destruction of the volcanic edifice and to a dramatic alteration of the shallow plumbing system. Moreover, post-collapse magmatic plumbing systems may become controlled by caldera-related structures.

Analogue studies have mainly aimed to study the nature of caldera fault structures, which are thought to provide the primary pathways for syn-and post-collapse intrusion and eruption, and how they relate to the attributes of the underlying magma body. Their results have contributed substantially to our current understanding of the process of caldera collapse and its impact on sub-volcanic plumbing systems.

4.5.1 Generalised Geometry and Kinematics of Ring-Fault Related to Caldera Subsidence

The vast majority of past studies have primarily addressed the question of how caldera subsidence is structurally accommodated. One motivation for this is a so-called ‘space problem’ arising from many field reports of ring faults that only dip inward, toward the caldera centre (Lipman 1984, 1997; Branney 1995; Cole et al. 2005), in contrast with only a few reports of ring faults that dip outward, at least partly (Clough et al. 1909; Mori and McKee 1987). While subsidence along an outward-dipping fault represents a kinematically reasonable geometry, and one predicted from analytical solutions (Anderson 1936), subsidence accommodated only by an entirely inward-dipping fault is kinematically unfeasible.

Analogue experiments have helped resolve this ‘space problem’ by showing that subsidence into a depleted reservoir is typically accommodated by a ring-fault system that consists of outward-dipping and inward-dipping faults or fault segments (Fig. 17) (Komuro 1987; Martí et al. 1994; Branney 1995; Roche et al. 2000). The outward-dipping faults usually form further toward the central part of the reservoir roof than the inward-dipping faults. Their position and geometry means that outward-dipping faults have a poorer preservation potential, which may account for their under reportage in field studies (Branney 1995).

In terms of kinematics, the outward-dipping (reverse) faults always form first in experiment. Analytical solutions and numerical models show that this is a consequence of ‘arching’ of the

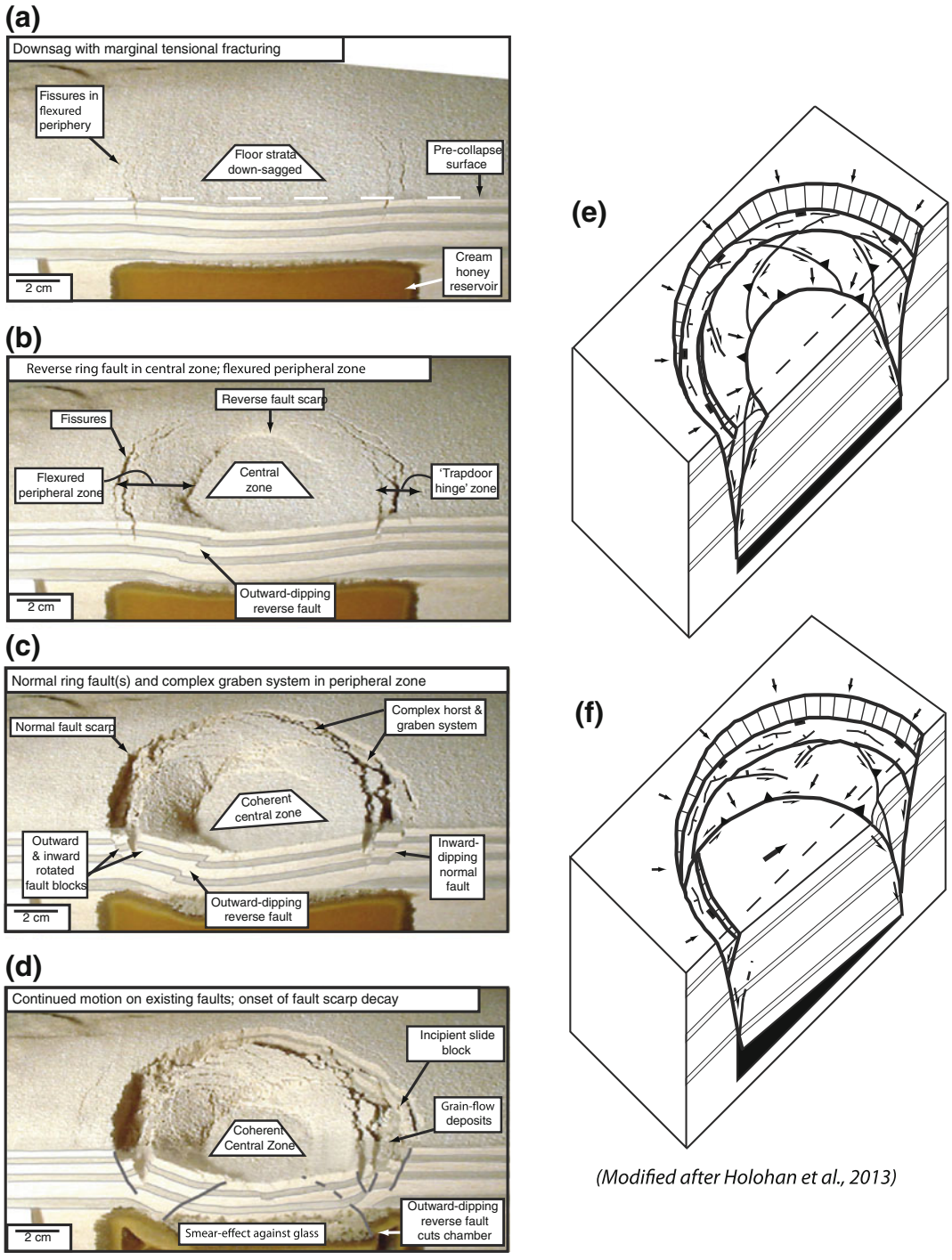

(Modified after Holohan et al., 2013)

◀ **Fig. 17 a–d** Structural evolution of a representative experimental caldera collapse. The experiment was conducted against a glass pane to gain simultaneous access to the structural development both in cross-section and in plan-view. The analogue magma reservoir is a sill-like half-cylinder of cream honey that is 10 cm in diameter and has 3.5 cm thick roof with an initially flat ceiling. This model hence has a reservoir roof thickness/diameter ratio of 0.3. The sand/gypsum cohesion is a little higher than ideal here (for illustration), and so marginal tensile fracturing is a slightly exaggerated. In addition, the sticky honey causes some smearing effects against the glass that become more pronounced with greater subsidence. However, the geometry, kinematics, and complexity of structures are overall very similar to most past analogue studies (cf. Martí et al. 1994; Branney 1995; Roche et al. 2000; Walter and Troll 2001; Kennedy et al. 2004). Note the formation of outward- and inward-dipping ring faults. Note also that in this example the sense of subsidence 'asymmetry' has reversed in later subsidence phases. **e** Block diagrams showing 3D fault geometry and slip-sense of experimental caldera centred ('symmetric') subsidence. **f** Block diagrams showing 3D fault geometry and slip-sense of experimental caldera off-centred ('asymmetric' or 'trapdoor') subsidence. In both cases, *half arrows* show fault slip sense; full arrows schematically show horizontal movements. The horizontal movements during collapse are directed radially-inward throughout the roof if collapse is centred, but may show a significant bulk translation in the roof centre if collapse is off-centred. These horizontal motions give rise to strike-slip components of fault slip-sense. Note that in the off-centred case, the strong horizontal motion toward the area of maximum subsidence favours the development of a normal ring fault (or ring-fault segment) in the 'hinge-zone' area on the opposite side of the roof. Modified after Holohan et al. (2013)

principal stress trajectories above the deflating reservoir (Anderson 1936; Sanford 1959; Holohan et al. 2011, 2013). The inward-dipping (normal) faults form later as the hanging-wall of the outward-dipping ring fault becomes gravitationally unstable (e.g. Martí et al. 1994; Roche et al. 2000) and/or if the subsidence becomes off-centred reservoir (trapdoor-like or 'asymmetric'; e.g. Holohan et al. 2011, 2013) (Fig. 17c). Slip sense on these faults may not be entirely dip-slip (Holohan et al. 2013) (Fig. 17e–f). As subsidence progresses, retreat of the ring fault scarps widens the model caldera diameter and forms a funnel-shaped caldera margin containing topographic embayments—as in nature (Branney 1995; Lipman 1997; Geshi et al. 2012).

4.5.2 Effects of Initial Geometric Parameters on Collapse

Two key geometric parameters in the structural evolution of collapse are: (i) the *ratio of reservoir roof thickness to roof diameter (T/D)* in cross-section (Roche et al. 2000; Kennedy et al. 2004; Geyer et al. 2006) and (ii) the *ratio of roof long axis to roof short axis* (*A/B*) in plan-view (Roche et al. 2000; Holohan et al. 2008a).

T/D ratio affects the structural style of roof subsidence (Fig. 18). At very low T/D ratios (<0.3), sagging of the roof, and not just ring faulting, plays an important role in accommodating subsidence (Roche et al. 2000; Kennedy et al. 2004; Holohan et al. 2013) (Fig. 18a). As T/D increases, sagging diminishes. At intermediate T/D ratios (0.3 < T/D < 1.0), the roof typically subsides along one main outward-dipping fault and one main inward-dipping fault. At high T/D (>1), the roof subsides via a complex system of mainly outward-dipping, but also locally inward-dipping, fractures (Fig. 18b, c). These fractures form in a sequence that migrates upward from the reservoir to the surface (Burchardt and Walter 2010). A sub-surface column of multiple fault blocks hence develops; the complexity of this column increases with increasing T/D ratio (Roche et al. 2000). Once deformation reaches the surface, the usual pattern of central outward-dipping faults and peripheral inward-dipping faults is established there (Roche et al. 2000; Burchardt and Walter 2010). This upward migration of faulting in experiments with high T/D ratios is remarkably similar to an apparent upward migration of seismicity recorded prior to the collapse of Miyakejima caldera, Japan, in 2000 (Geshi et al. 2002; Burchardt and Walter 2010; Ruch et al. 2012).

T/D ratio also affects the percentage of reservoir depletion required to develop collapse. For a given reservoir shape and size, higher T/D necessitates greater reservoir depletion to cause the onset of collapse and to attain each stage in the structural evolution thereafter (Geyer et al. 2006). These findings are similar to those of analytical

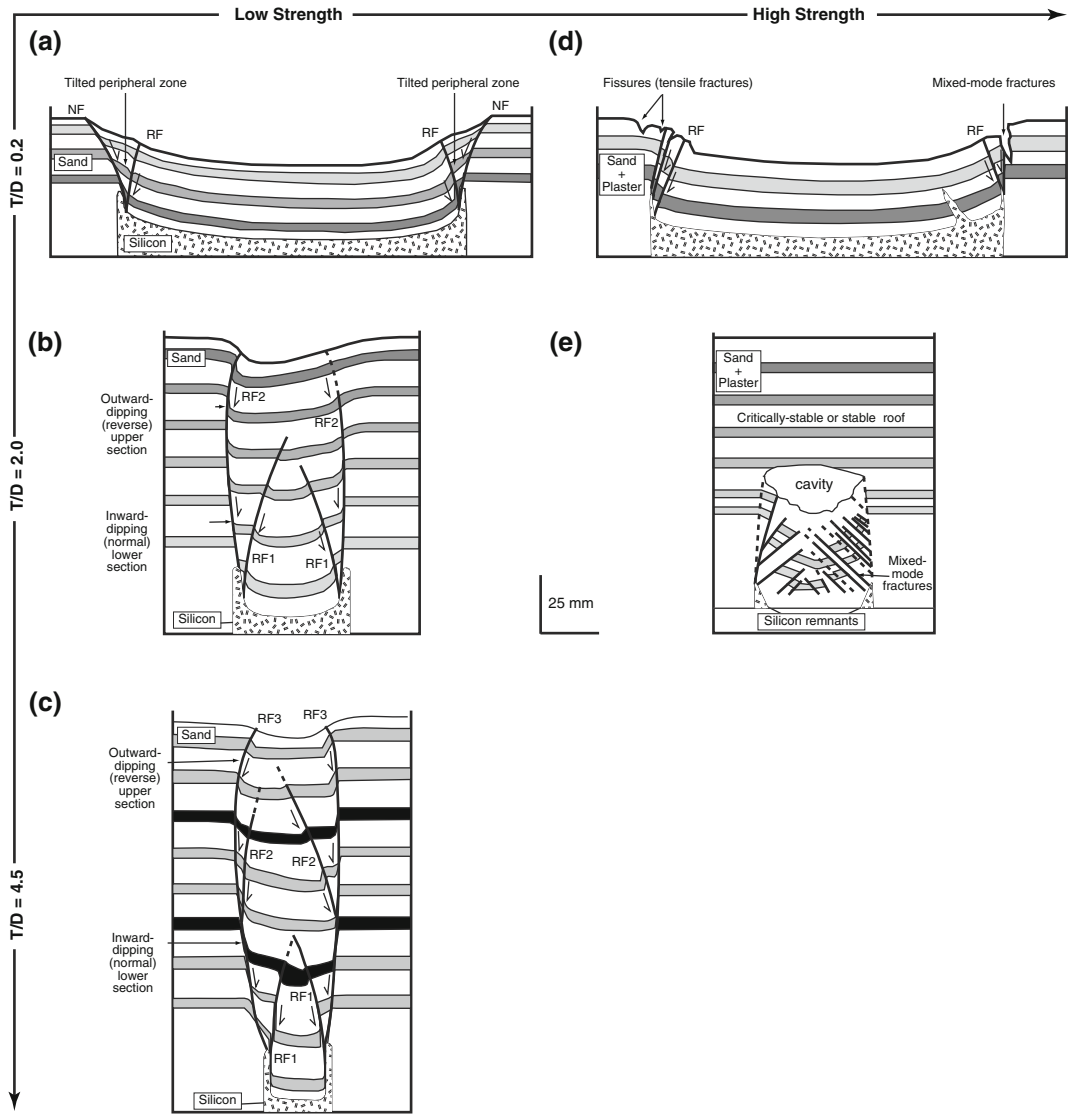

Fig. 18 How varying roof thickness/diameter (T/D) ratio and material strength may influence caldera collapse structure. To the *left* are results of analogue models with low-cohesion sand and with: **a** T/D = 0.2; **b** T/D = 2.0; **c** T/D = 4.0 (modified from Roche et al. 2000). To the *right* are results of models with a higher cohesion sand/plaster mix and with: **d** T/D = 0.2; **e** T/D = 2.0 (modified from Roche et al. 2001). NF = Normal fault; RF = Reverse fault. If present, numbers indicate order of fault localisation. All drawings are to the same scale. Note that the models in parts **a, b**, and **c** were run in '2D' between two glass panes, whereas those in **d** and **e** were run in '3D'. Low cohesion models run in '3D' produce very similar structural developments to the 2D ones (cf. Roche et al. 2000), however, and so the variations in the results shown here stem mainly from differing roof geometry and strength

studies (e.g. Roche and Druitt 2001) and numerical models (Holohan et al. 2011, 2013).

A/B ratio affects the three-dimensional collapse structure and the lateral propagation of ring faults (Fig. 19). At high A/B ratios, and for a uniform roof thickness, the T/D ratio is at a maximum along the short axis and a minimum along the long axis. The structural style in cross-section can thus be more fault-controlled along the short axis and more sagging-affected along the long axis

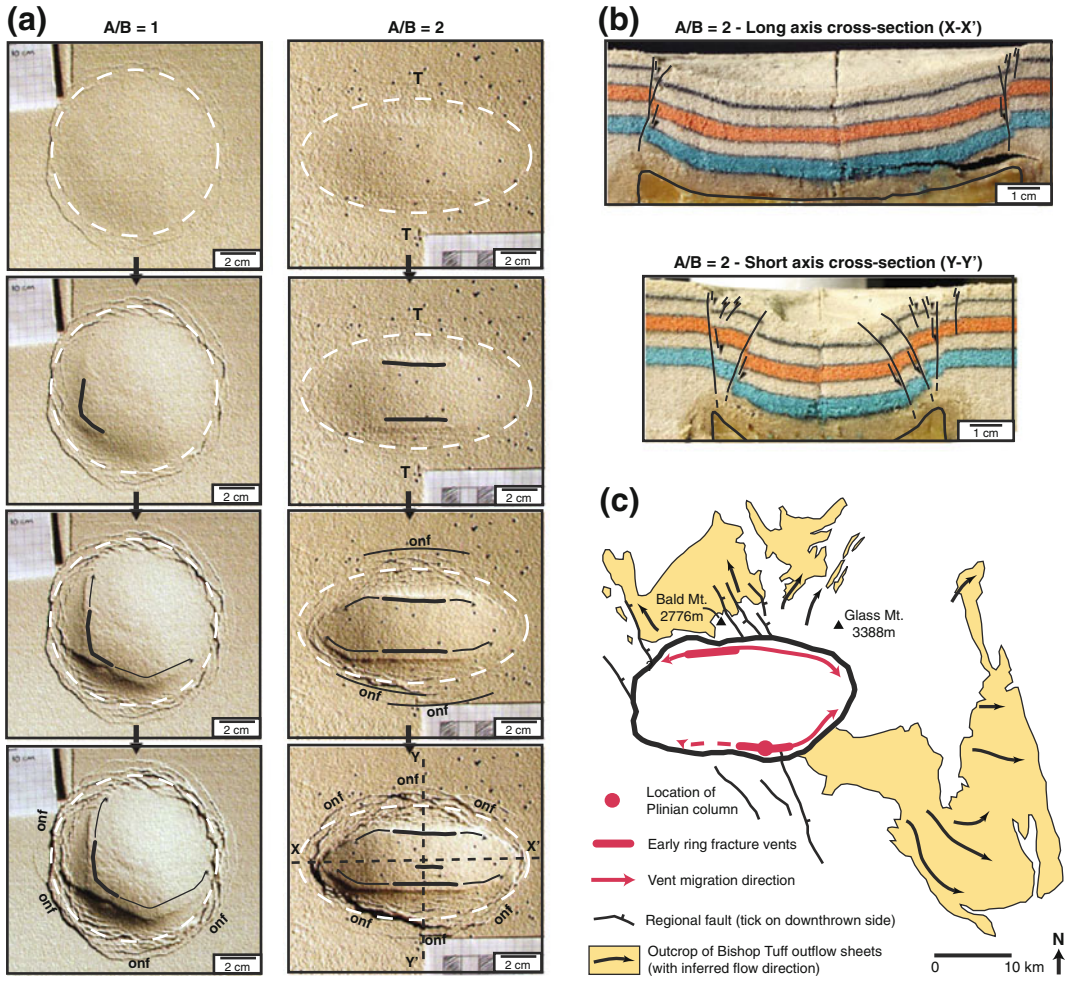

Fig. 19 How varying magma chamber's plan-view long to short axis (A/B) ratio may influence caldera collapse structure. **a** Evolutions of collapse into a cream honey reservoir with A/B = 1.0 (i.e., circular in plan-view) in the left-hand column and with A/B = 2.0 (i.e., highly elliptical in plan-view) in the right-hand column. **b** Cross-sections through the long and short axes of the model with A/B = 2.0 in part **a**. Note the greater roles played by sagging versus faulting in accommodating vertical displacement on the long and short axes, respectively. This reflects the variation in T/D along either axis in a roof that is elongate in plan-view. **c** Outline map of Long Valley caldera with inferred migration of vents feeding syn-collapse outflow ignimbrite sheets. Modified from Wilson and Hildreth (1997) and Holohan et al. (2008a)

(Holohan et al. 2008a) (Fig. 19b). For a reservoir that is circular in plan-view (A/B = 1), ring faults typically localise at one random point in the reservoir roof and then propagate bi-directionally around the reservoir circumference (Roche et al. 2000; Holohan et al. 2008a). For a reservoir that is highly elliptical in plan-view (A/B ≥ 2), and has a relatively low T/D ratio (T/D < 0.4), the ring faults systematically localise as separate segments near the opposite ends of the reservoir roof's short axis. Each fault segment then propagates bi-directionally toward the roof's long axis, where they link to form a single ring fault. This experimental ring fault propagation pattern at high A/B results from a higher shear strain along the short axis during reservoir depletion, as here the same vertical displacement is accommodated over a shorter horizontal distance than on the long axis.

This effect of roof geometry may explain the emplacement mechanism inferred for the highly elliptical Slaufrudalur pluton, Iceland (Burchardt et al. 2012) and the vent migration pattern inferred during the formation of the highly elliptical Long Valley caldera, USA (Wilson and Hildreth 1997; Holohan et al. 2008a) (Fig. 19c).

4.5.3 Effects of Host-Rock Cohesion on Collapse

As in the case of intrusions, host-rock strength affects the nature of collapse structures (Roche et al. 2000, 2001) (Fig. 18). At low material strength, peripheral extension near the surface is accommodated only by shear fracturing (normal faults), but at high material strength, and especially at low T/D ratios, opening-mode or mixed-mode fractures play more of a role (Fig. 18d). Changing the material strength also alters the sub-surface fracturing process seen at high T/D ratios (T/D > 1.2). At low material strength, the multiple sub-surface blocks are delimited by shear fractures. At high strength, however, near-horizontal opening-mode fractures may form in the centre of the roof and grow to form quasi-stable, sub-surface cavities (Fig. 18e). Detachment of material from a cavity roof forms numerous smaller blocks and causes the cavity to migrate upward. Consequently, the high-strength reservoir roofs may disintegrate into a column of coarse, loosely-fitting, rubble. In some cases, the roof above a sub-surface cavity may remain stable, in which case the collapse process halts underground.

These strength-related effects in experiments are remarkably similar to those reported in studies of mining-induced collapse (Reddish and Whittaker 1989), and have been observed at basaltic volcanoes (Rymer et al. 1998; Carter et al. 2006). Moreover, the experimental results support Anderson's (1936) postulate that high rock strength is required to develop the near-horizontal, opening-mode 'cross-fracture' that defines the upper cap of a complete subterranean 'ring dyke' (Clough et al. 1909; Richey 1932) formed in the case of magma emplacement by cauldron subsidence.

4.5.4 Effects of Topography and Regional Tectonics on Collapse Structures

Pre-collapse topography has little or no effect on experimental collapse structures when a magma reservoir resides inside, and is thus smaller than, a conical edifice (Walter and Troll 2001). On the other hand, when the reservoir is centred below and is significantly larger than a conical edifice, the topographic load causes steepening of the outward-dipping faults and more focussed subsidence (Lavallée et al. 2004). Where regional faults formed in pre-collapse extensional or strike-slip tectonic regimes are near to or coincide with the reservoir margins in experiments, they are at least partly reactivated as subsidence-guiding faults, thereby deflecting or even halting the propagation of caldera-related ring faults (Acocella et al. 2004; Holohan et al. 2005, 2008b). These results provide insight into how regional-tectonic faults may act as conduits and venting sites during caldera-forming eruptions, as inferred at, e.g., Glencoe caldera, Scotland (Moore and Kokelaar 1998).

4.5.5 Effects of Caldera Collapse on Magma Chamber Dynamics and Ring-Dyke Intrusion

Kennedy et al. (2008) modelled the effects of caldera collapse on magma chamber dynamics and ring-dyke intrusion through laboratory experiments of a rigid, cylindrical piston sinking into a slightly larger cylinder filled with corn syrup (Fig. 20a). The process can be described by two dimensionless geometrical parameters, describing subsidence and tilt of the subsiding magma reservoir roof, and by one dimensionless parameter, the Reynolds number, describing the influence of inertial and viscous forces on flow, mixing, and stirring (Fig. 20b–d). The experimental results illustrate how caldera collapse likely causes magma in the reservoir to mix and overturn and to have complex flow paths (hence emplacement directions) within a ring dyke. These effects account for compositional zonation of many ignimbrites (Hildreth and Wilson 2007),

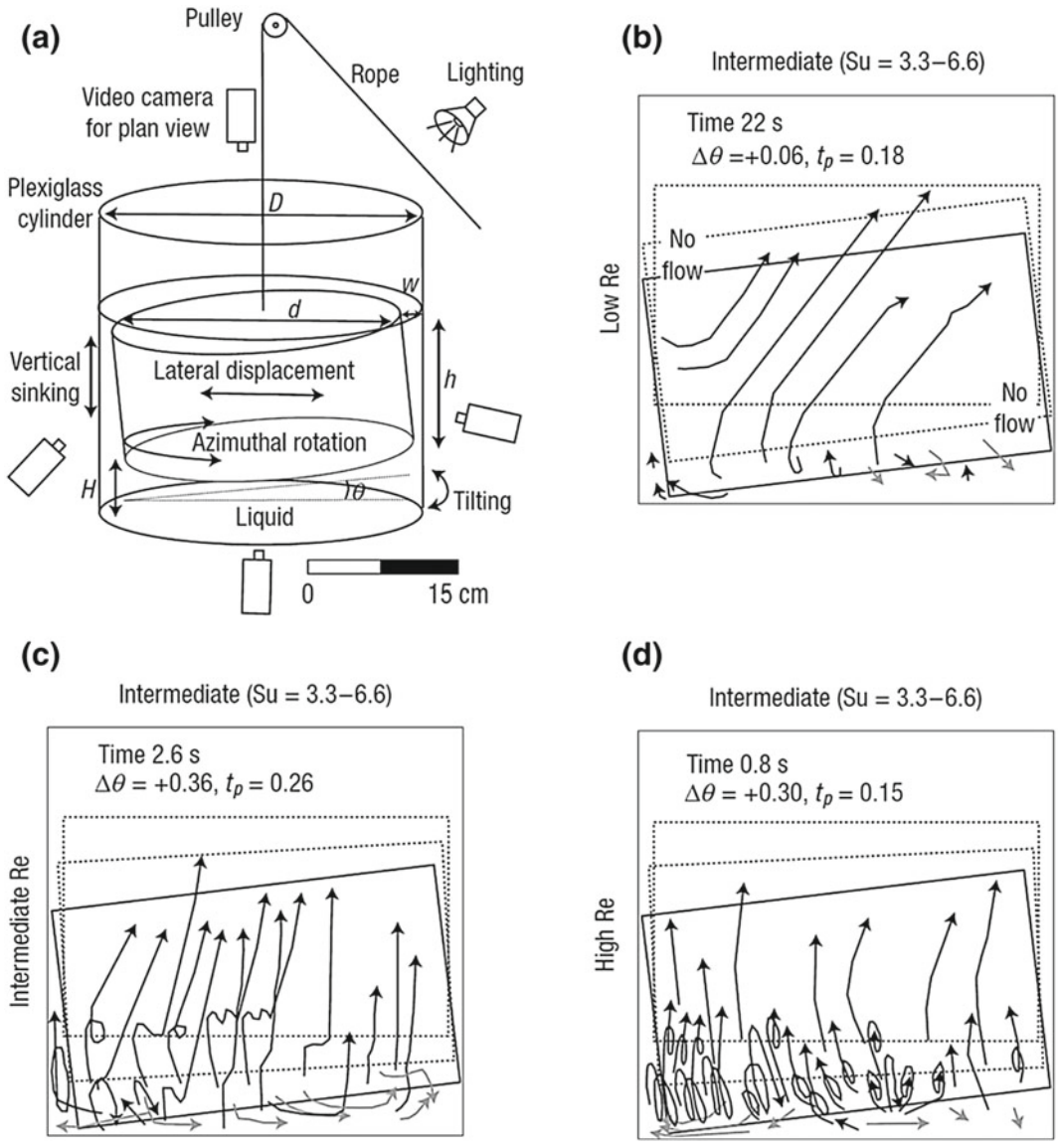

Fig. 20 How variation in the Reynolds number (*Re*) may affect magma flow dynamics in a reservoir and ring conduit during caldera collapse. **a** Sketch of experimental set-up involving the sinking of a cylindrical block into a cylindrical reservoir of larger diameter. The liquid in the reservoir contains neutrally buoyant marker particles that enable tracking of the liquid flow paths. **b** Results for low Re. Flow is predominantly laminar, but involves a large lateral component within the dyke due to the tilting of the downgoing block. **c** Results for intermediate *Re*. Some kinking and local overturning of flow paths are observed. Flow in the ring conduit tends to be more vertical overall. **d** Results for high *Re*. Flow paths show multiple and much tighter overturns. Onset of such turbulent behaviour occurs as the liquid transitions from reservoir into the ring conduit. All results shown here are representive and for an intermediate subsidence stage as denoted by the subsidence number (*Su*), which is the block diameter normalised to block subsidence. Some further variations, e.g. in ring conduit flow directions, are also seen as Su increases. From Kennedy et al. (2008)

and for mingled magmas observed in many exposed ring dykes (Sparks 1988).

4.5.6 Kinematics of Pre-collapse 'Tumescence' and Post-collapse Caldera 'Resurgence'

For many large (>c. 10 km diameter) silicic magmatic systems, caldera formation is one of three main stages in their evolution (Smith and Bailey 1968; Lipman 1984, 1997). In *Stage 1,* voluminous intrusion of less-evolved magmas into the crust eventually leads to the development of a larger, more-evolved magma reservoir (Fig. 21a). As the magma-reservoir grows, the overlying host rocks may be uplifted, a phenomenon termed 'tumescence'. In *Stage 2,* a caldera forms when the magma reservoir roof subsides rapidly during eruption (Fig. 21b). During *Stage 3,* renewed intrusion of magma rejuvenates the sub-caldera plumbing system. Growth of a new or remobilised sub-caldera pluton may cause uplift of the overlying caldera floor and infill, a phenomenon termed 'resurgence' (Fig. 21c; Kennedy et al. 2012).

Analogue modelling studies that superimposed deformation of some or all of these three stages indicate that structures inherited from previous stages affect the kinematics of later stages. Low-cohesion models showed that an initial uplift phase generates peripheral *inward-dipping reverse ring faults* (Martí et al. 1994) (Fig. 21a). With large uplift relative to reservoir diameter, central *outward-dipping normal faults* may also form (Acocella et al. 2000, 2001). During the collapse phase, these reactivate

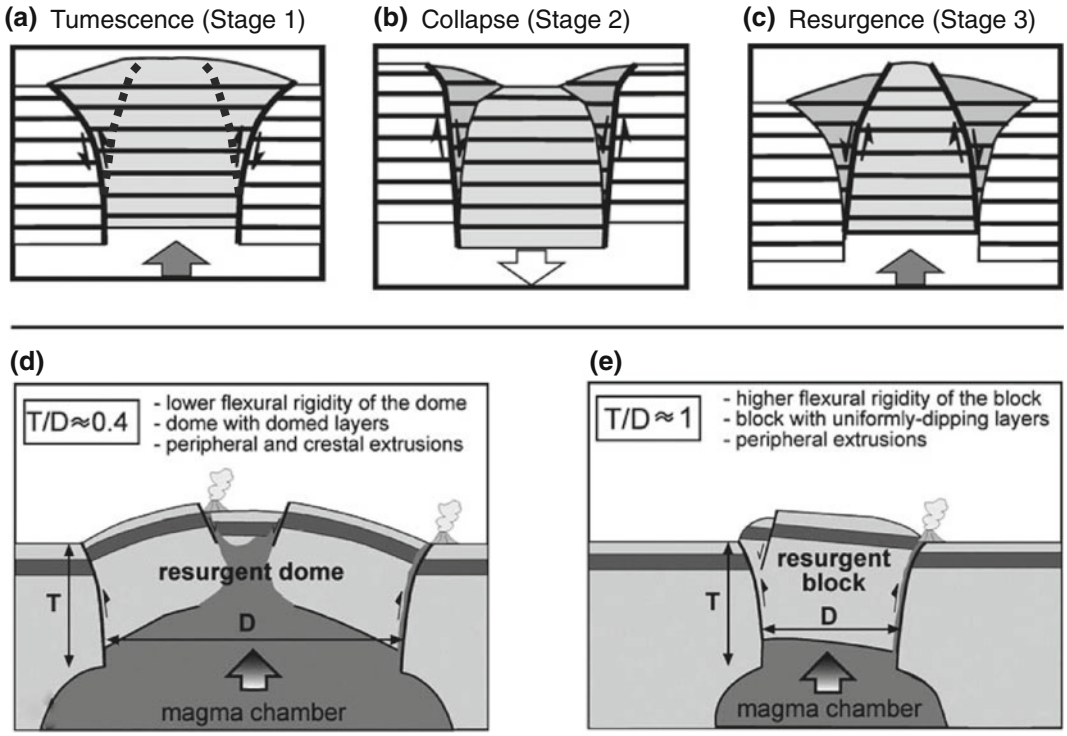

Fig. 21 Schematically-drawn section-view results of analogue models illustrating the three stages in caldera development. **a** Geometry and slip-sense of ring faults formed during pre-collapse tumescence. **b** Reactivation (inversion) of tumescence-related ring fault(s) during collapse. c Further inversion of collaspe-related ring faulting during post-collapse resurgence. Note the greater basal displacement here compared to that in part **a**. Also shown here are the effects of d low T/D ratio and **e** high T/D ratio on the structural style of resurgence. Similar effects are seen for the collapse stage (see Fig. 18). Modified from Acocella et al. (2000, 2001)

(Fig. 21b). Further uplift during resurgence may lead to complete inversion of the movements during the collapse phase (Fig. 21c). Structural relationships very similar to those in such models exist at the exhumed Rum caldera volcano, Scotland, where evidence for pre-collapse uplift is atypically clear (Holohan et al. 2009). Higher-cohesion models superimposing multiple cycles of tumescence, collapse and resurgence developed a complex 'piecemeal' jigsaw of roof blocks delimited by intersecting radial and concentric faults (Walter and Troll 2001). Structural relationships similar to these occur at Tejeda caldera, Gran Canaria (Troll et al. 2002).

Acocella et al. (2000, 2001) show that the T/D ratio affects the structural development of resurgence similarly to that of collapse. At low T/D ratios, upwarping plays a major role in roof uplift and forms an apical graben (Fig. 21d), a structural style comparable to that at Valles caldera, New Mexico. At high T/D ratios, the roof uplift is accommodated by a more piston-like inversion of the collapse-related ring faults (Fig. 21e), a style comparable to block-like resurgence at Ischia Island, Italy.

4.5.7 Limitations of Caldera-Related Experiments

Although past experiments have simulated the development of fracture systems that likely act as magma pathways, magma intrusion into these systems, as well as interaction between fracturing and intrusion, were not simulated. Where fluid analogue reservoirs were employed, viscosities were too high to allow fluid intrusion into dilating faults. Where a balloon or a solid piston was used, such intrusion was impossible. To our knowledge, only one study (Kennedy et al. 2008) has directly simulated coupled collapse and intrusion into caldera-related faults, albeit under highly predefined conditions.

A second common limitation is that fluid withdrawal from the analogue reservoir was not through the roof and so did not result in eruption at surface. Consequently, effects of synchronous in-filling of the caldera by erupted material are unaccounted for. The experimental procedure instead more closely approximates caldera collapse triggered by lateral withdrawal and occurring without much in-fill by erupted material—as has occurred at e.g., Katmai caldera, Alaska (Hildreth and Fierstein 2000) and Miyakejima caldera, Japan (Geshi et al. 2002).

A third limitation is that the fluids used are single phase (liquid) only. Gas exsolution during magma intrusion and eruption may strongly affect collapse dynamics, especially with more evolved magma compositions (Stix and Kobayashi 2008; Michon et al. 2011). Such effects remain to be examined experimentally.

It should be noted that the fixed balloons or piston-like set-ups in studies of resurgence enforce a complete remobilisation of the pre-caldera magma reservoir, rather than allowing for the generation of new intrusion geometry. As a consequence, ring faults formed during a preceding phase were commonly inverted entirely along their circumferences during the succeeding phase. While this may be valid for some resurgent calderas, such a close, reactivation-based relationship between collapse- and resurgence-related structures is not so apparent at others (e.g. Long Valley caldera, California—Wilson and Hildreth 1997). 'Resurgence' in the latter cases may take the form of newly-generated sub-caldera intrusion geometries, which require a less constrained model set up to develop.

4.6 Ground Deformation Induced by Intrusions

Ground displacements measured at volcanoes have become very important for unravelling the dynamics of active volcano plumbing systems. This is because the monitored ground deformation patterns reflect the shape and dynamics of the underlying volcano plumbing system. Ground displacements measured during magma intrusion can range from a few centimetres, such as those induced by the emplacement of dykes and sills (e.g. Amelung et al. 2000; Sigmundsson et al. 2010), to several hundred meters, such as that induced by the emplacement of cryptodomes (e.g., the 1980 Mount St. Helens eruption; Lipman et al. 1981).

Geodetic monitoring systems that measure such displacements have become very important and increasingly sophisticated tools for monitoring and unravelling the dynamics of volcano plumbing systems. Geodetic measurement methods such as GPS, InSAR, photogrammetry, tilt, and precise levelling, now provide accurate and high-resolution time-series maps of displacements at many active volcanoes. They are able to detect even subtle ground movements induced by changes in magma pressure or distribution at depth. Data from these methods are widely used to (i) forecast that an eruption is imminent (Sigmundsson et al. 2010) and (ii) infer the geometry of volcanic plumbing system components, such as dykes (Wright et al. 2006 Fukushima et al. 2010), cone sheets (Chadwick et al. 2011), sills (Amelung et al. 2000; Sigmundsson et al. 2010) and magma reservoirs (Chang et al. 2007).

Geodetic data is routinely analysed by fitting displacement data predicted from analytical or numerical models to the measured data. The best fit thus provides insights into the depth, shape and orientation of underlying magma body responsible for the observed ground movements. Such deformation sources are usually interpreted in terms of magma bodies or pathways. These analyses have several limitations: (i) The modelled sources usually have highly simplified shapes to make inversion of observed displacements computationally tractable and efficient. Field observations show that the shapes of natural magma intrusions are more diverse and complex. (ii) The source models are consequently also a highly simplified representation of the geological process(es) and their development, and of how these affect ground displacements. (iii) Many source modelling studies only take into account the elastic response of the host rock, while plastic deformation, such as faulting, may play a major role in nature.

The interpretation of the underlying cause(s) of ground displacements at volcanoes in terms of the plumbing system attributes is a challenge that also can be addressed by laboratory models. Firstly, as shown in the preceding sections (see above), analog models are capable of reproducing the complex geometries of various kinds of igneous intrusion. Secondly, they are capable of simulating more complex elasto-plastic host-rock rheology. Thirdly, a range of photogrammetric and other techniques (e.g. laser scanning, structured light) for measuring surface displacements, can be applied to laboratory models. Therefore, if they are set up appropriately (see below), such models carry the advantage of being a geologically representative physical system in which both the shape of the plumbing system and the resulting pattern of free surface displacement are known.

4.6.1 Surface Deformation Related to Dykes

The first laboratory study addressing surface deformation induced by dykes considered a pseudo-2-dimensional, vertically-elongated cell filled with a cohesive flour-sugar mix; the "dyke" was modelled by two moving rigid sleeves, the distance between which was increased by inserting sheets of cardboard (Mastin and Pollard 1988). Very similar experiments with ground sand have been conducted recently in three dimensions by Trippanera et al. (2014). In agreement with the theoretical results of Pollard and Holzhausen (1979), geodetic data and field observations (e.g. Pallister et al. 2010), these laboratory experiments produce a surface depression above the tip of the opening dyke. In addition, a broad area of surface uplift occurs marginal to the depression as the dyke opens. The laboratory models show that subsidence to form the depression is accommodated by central sagging, block rotation and/or reverse faulting, as well as by tension fractures (crevasse) or normal faults that bound the depression.

The experiments of Mastin and Pollard (1988) and Trippanera et al. (2014), like the corresponding analytical or numerical models, represent the inflation of an already emplaced dyke, rather than a full consideration of dyke propagation.

In order to simulate and measure the surface deformation associated with dyke propagation, Abdelmalak et al. (2012) and Galland (2012) designed 2-dimensional and 3-dimensional experiments, respectively, in which dyke emplacement

is simulated by the injection of a viscous fluid into cohesive granular material. Surface uplift is induced by the emplacement of a dyke, but the character and cause of the uplift is drastically different with respect to that in the experiments of Trippanera et al. (2014). The uplifted area is much narrower and is focussed directly above the tip of the propagating dyke; no depression forms. Like the 2-D experiments of Mathieu et al. (2008), this dyke-induced uplift results from a viscous indenter process of propagation. The models show that reverse faults steply dipping toward the dyke tip accommodate the uplift.

These differing models of dyke-related surface displacement results hence form a basis for discriminating dyke inflation versus viscous indentation from geodetic data sets. Future work might consider analysis of surface displacements induced in gelatine models, which offer the possibility of quantifying such behaviour for a more elasticity-dominated dyke propagation process.

4.6.2 Surface Deformation Related to Saucer-Shaped Sills or Cone Sheets

Galland (2012) used silica flour and végétaline oil models (Fig. 22a) to quantify a time series of 3D surface displacement related to the emplacement of cone sheets of saucer-shaped sills. Intrusion of the oil triggered subtle deformation of the flat model surface, which was monitored by using a structured light-based system, combining a video-projector and a CCD camera (Brèque et al. 2004; Galland 2012). This system allows fast (<1.5 s) and accurate measurements of the model surface, and produced topographic maps through time.

After the experiments were run, the oil solidified in the models, and the intrusion was excavated. If the intrusion was flat-lying, the shape of its upper surface was also measured with the same system, such that the ground deformation pattern could be directly compared to its associated underlying magma conduit.

The experiment results show a remarkable correlation between the asymmetry of the ground deformation pattern and the asymmetry of the underlying intrusion (Fig. 22a). In particular, the steepest edges of the uplifted zones at the model surface were always located above the shallowest parts of the underlying intrusion. Given that the asymmetry of the ground deformation developed relatively early during the experiments, it was thus possible to detect well before the eruption where the oil was rising towards the surface (see also the 2D dyke results of Abdelmalak et al. 2012). These experiments thus show that real-time analysis of asymmetrical development of ground deformation patterns in volcanoes could be used as a predictive tool to forecast the location of an impending volcanic eruption.

4.6.3 Surface Deformation Related to Cryptodomes

Cryptodome-induced deformation has been studied in the laboratory by Donnadieu and Merle (1998, 2001), who used silicone as model magma and a cohesive pack of granular material to simulate a volcanic edifice (Fig. 22b). They show that the early emplacement of the cryptodome generates curved inward-dipping major shear zones that affect the flanks of the edifice. As intrusion proceeds, the magma deviates toward the flanks by following these shear zones, such that it grows laterally and leads to a bulge on the flank of the edifice. Merle and Donnadieu (2000) and Donnadieu et al. (2003) applied digital photogrammetry to their experiments in order to quantify the horizontal displacements of the flanks of a volcanic edifice intruded by a cryptodome. They show that the expected displacement is clearly asymmetrical, such that most of the flank is affected by a substantial bulging (Fig. 22b). These results are in very good agreement with the geodetic observations collected before the 1980 eruption of Mount St. Helens (Lipman et al. 1981). In addition, these results explain how the processes controlling the emplacement of cryptodomes also govern lateral volcanic blasts resulting from a volcano flank collapse. As for the other intrusions types described above, such quantitative laboratory model results therefore provide a basis for linking ground displacements at volcanoes to an underlying physical process and so can assist in real time hazard assessment.

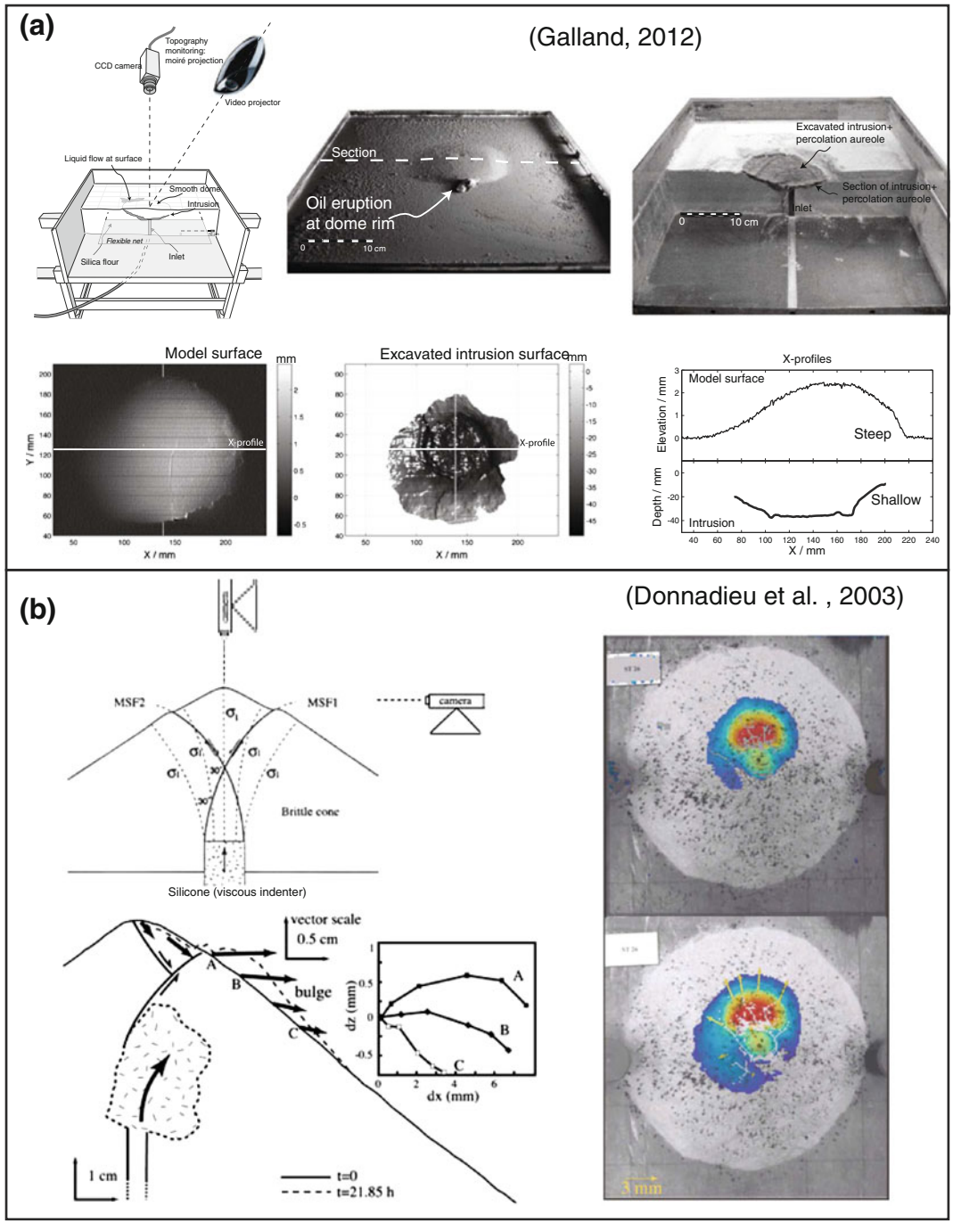
(a)
(Galland, 2012)
Topography monitoring: moiré projection
CCD camera
Video projector
Liquid flow at surface
Smooth dome
Intrusion
Flexible net
Silica flour
Inlet
Section
Oil eruption at dome rim
0
10 cm
Excavated intrusion+ percolation aureole
Section of intrusion+ percolation aureole
Inlet
0
10 cm
Model surface
mm
X-profile
Y / mm
X / mm
Excavated intrusion surface
mm
X-profile
X / mm
X-profiles
Model surface
Elevation / mm
Steep
Depth / mm
Shallow
Intrusion
X / mm
(b)
(Donnadieu et al. , 2003)
MSF2
MSF1
camera
Brittle cone
Silicone (viscous indenter)
vector scale
0.5 cm
A
B
C
bulge
dz (mm)
dx (mm)
1 cm
t=0
t=21.85 h
3 mm

◀ **Fig. 22** Characteristic experimental studies of ground deformation induced by magma intrusions. **a** Experimental study of Galland (2012). *Upper left* Drawing of experimental setup. *Upper central* Oblique photograph of model surface at the end of an experiment. *Upper right* Intrusion partly excavated after oil solidification. *Lower left* Topographic map of model surface during an experiment, made by using a moiré projection device (Brèque et al. 2004). *Lower central* Topographic map of top surface of excavated intrusion, again made by using the moiré projection device. *Lower right* Comparison between corresponding profiles of the model surface (*top*) and underlying intrusion (*bottom*). The positions of the profiles are indicated with the white lines on the maps to the right (X-profile). **b** Experimental study of Donnadieu et al. (2003). *Upper left* Drawing of experimental setup, silicone putty being injected at the base of a cone made of sand. The deformation of the cone can be monitored from a side camera or a top camera. *Lower left* Results from side observations of volcanic edifice deformation in experiments (Donnadieu and Merle 1998; Merle and Donnadieu 2000). *Right* Horizontal displacement maps of volcanic edifice deformation at two time steps of an experiment, computed using digital photogrammetry (Donnadieu et al. 2003)

4.7 Magma Intrusions in Deforming Crust (Magma-Fault Interactions)

Volcanic activity concentrates at tectonic plate boundaries, where the Earth's crust is actively deforming. Good examples are active margins, which host 75 % of volcanic eruptions and 90 % of earthquakes. Understanding how magmatic intrusions are affected, or interact, with tectonic deformation of the crust is thus a key aspect of the dynamics of volcanic plumbing systems.

To address this aspect, the experimental set-ups need to properly simulate both the mechanical behaviour of the magma and the deforming host rocks. In particular, a major challenge is to account for faulting. Gelatine, for example, is not suitable, as the high strength of the gelatine does not allow shear failure under the low stresses applied in the models. Gelatine only enables to simulate a stressed crust (Hubbert and Willis 1957; Watanabe et al. 2002; Kervyn et al. 2009; Menand et al. 2010; Daniels and Menand 2015) or a crust with pre-existing fracture planes (Le Corvec et al. 2013).

In contrast, granular materials are suitable for addressing the interactions between faults and magmatic intrusion. Sand/silicone models, for example, have been extensively used to constrain the emplacement of high viscosity magma in the brittle crust in any kind of tectonic settings, from pure extension (Fig. 23a) (Román-Berdiel 1999; Bonini et al. 2001; Corti et al. 2003), transtension (Corti et al. 2001), strike-slip faulting (Fig. 23b) (Román-Berdiel et al. 1997; Román-Berdiel 1999; Corti et al. 2005; Holohan et al. 2008b), transpression (Benn et al. 1998, 2000), to pure compression (Fig. 23c, d) (Musumeci et al. 2005; Mazzarini et al. 2010; Montanari et al. 2010a, b). All these models produced two fundamental findings: (i) the shapes of magma intrusions are controlled by the deformation, and (ii) vice versa the development of the deformation patterns is perturbed by the presence of a viscous heterogeneity.

These studies demonstrate that the elongation (i.e. orientation) of magma bodies is governed by the far field principal components of the deformation field. In extension, the model intrusions are elongated such that the short axis is perpendicular to the direction of extension. In strike-slip and compressional settings, the intrusions are also elongated, but in contrast to the extensional case, the short axis is perpendicular to the main shortening direction. This implies that in strike-slip and transpressional regimes, intrusions are elongated oblique to the main strike-slip faults. In these models, it is noticeable that faults exert only a very local effect on intrusions, which develop small sharp edges at the roots of faults. Conversely, faults tend to nucleate at the edges of intrusions, which represent rheological discontinuities that localise strain in the models.

Sand/silicone models, however, suffer from some limitations. The scaling of these experiments is such that: (i) the silicones only simulates very high viscosity magmas, i.e. between 10^{16} and 10^{17} Pa s, which is way above the range of common basaltic to rhyolitic magmas between 100 and 10^{8} Pa s; and (ii) sand is too loose and only simulates shear failure (faulting), but not

tensile or mixed-mode fracturing that may arise as magmas interact with a pre-existing failure surface (Fig. 23b, c). Consequently, these models do not simulate the formation of magmatic sheet intrusions such as dykes and sills, which are fundamental magma pathways, and their ability to simulate the effects of the faults on intrusions are rather limited.

In order to overcome these limitations, other materials are required. Model magmas need to have lower viscosities than silicone putty, and the model crust needs to be more cohesive than dry sand. As noted in previous sections (Sects. 2.1.2 and 2.2.3), suitably low viscosity model magmas include Golden Syrup, molten vegetable oil, and RTV silicone, while suitable rock analogues include sieved ignimbrite, fined-grained silica flour and diatomite powder (Galland et al. 2006; Mathieu et al. 2008; Gressier et al. 2010; Abdelmalak et al. 2012).

In contrast to sand-silicone models, the models with these alternative materials clearly highlight the prominent effects of faults on magma transport (Fig. 23a, d). The experiments of Galland et al. (2007a) and Ferré et al. (2012), for instance, show that thrust faults localise magma transport both when the faults are active and inactive. These models highlight that gently-dipping faults facilitate substantial horizontal transport of magma in compressional settings, with important implications for magma plumbing systems in active margins, which are currently still considered as simplistic sub-vertical pathways.

Similarly to sand-silicone models, silica flour-vegetable oil models also show that intrusions greatly affect the tectonic pattern, as they correspond to weak heterogeneities that concentrate stresses and nucleate deformation, in a similar manner to a velocity discontinuity (Barrier et al. 2002). Consequently, intrusions locally perturb regional tectonic structures (Fig. 23d) (Galland et al. 2007a). These experimental results are corroborated by geological examples of orogenic fronts curved around batholiths (e.g., Boulder Batholith, Montana, USA; Kalakay et al. 2001; Lageson et al. 2001) and volcanoes, such as Tromen Volcano, Northern Patagonia, Argentina (Marques and Cobbold 2006; Galland et al. 2007b; Llambías et al. 2011), Guagua Pichincha Volcano, Ecuador (Legrand et al. 2002), and El Reventador Volcano, Ecuador (Tibaldi 2005; Tibaldi et al. 2010).

4.8 Explosive Volcanic Vents

All the experimental studies described above deal with magma transport and emplacement at depth. To ultimately feed a volcanic eruption, however, the volcano plumbing system must intersect the Earth's surface. Therefore, understanding how magma flows through and exits the plumbing system to reach the Earth's surface is a critical factor for assessing volcanic hazards. Laboratory experiments have been also designed to study the dynamics of the shallowest parts of volcano plumbing systems—i.e. the part leading into the eruptive vent.

Most vent-related experiments address the dynamics of explosive processes that arise from large magma overpressures and that result in piercement structures, such as diatremes and breccia pipes. These overpressures can result from: (i) gas exsolution during magma ascent and decompression, leading to the development of kimberlites (Sparks et al. 2006; Brown et al. 2007); (ii) phreatomagmatism due to explosive magma—water interactions, leading to the formation of maar-diatremes (Lorenz and Kurszlaukis 2007; White and Ross 2011); or (iii) rapid generation of gas due to accelerated maturation of organic-rich rocks in the surrounding of magma intrusions, producing hydrothermal vent complexes (Svensen et al. 2004, 2006; Aarnes et al. 2011b, 2012).

The first qualitative laboratory study of piercement structures was conducted by Daubrée (1891) to investigate the formation of diatremes. These pioneering experiments did not address fluidisation processes, however, which geological observations suggest is prominent during diatreme and breccia pipe formation. In contrast, the later experiments of Woolsey et al. (1975) and McCallum (1985) did so. These authors used granular materials of various grain sizes (clay to gravels) and cohesions to simulate the behaviour

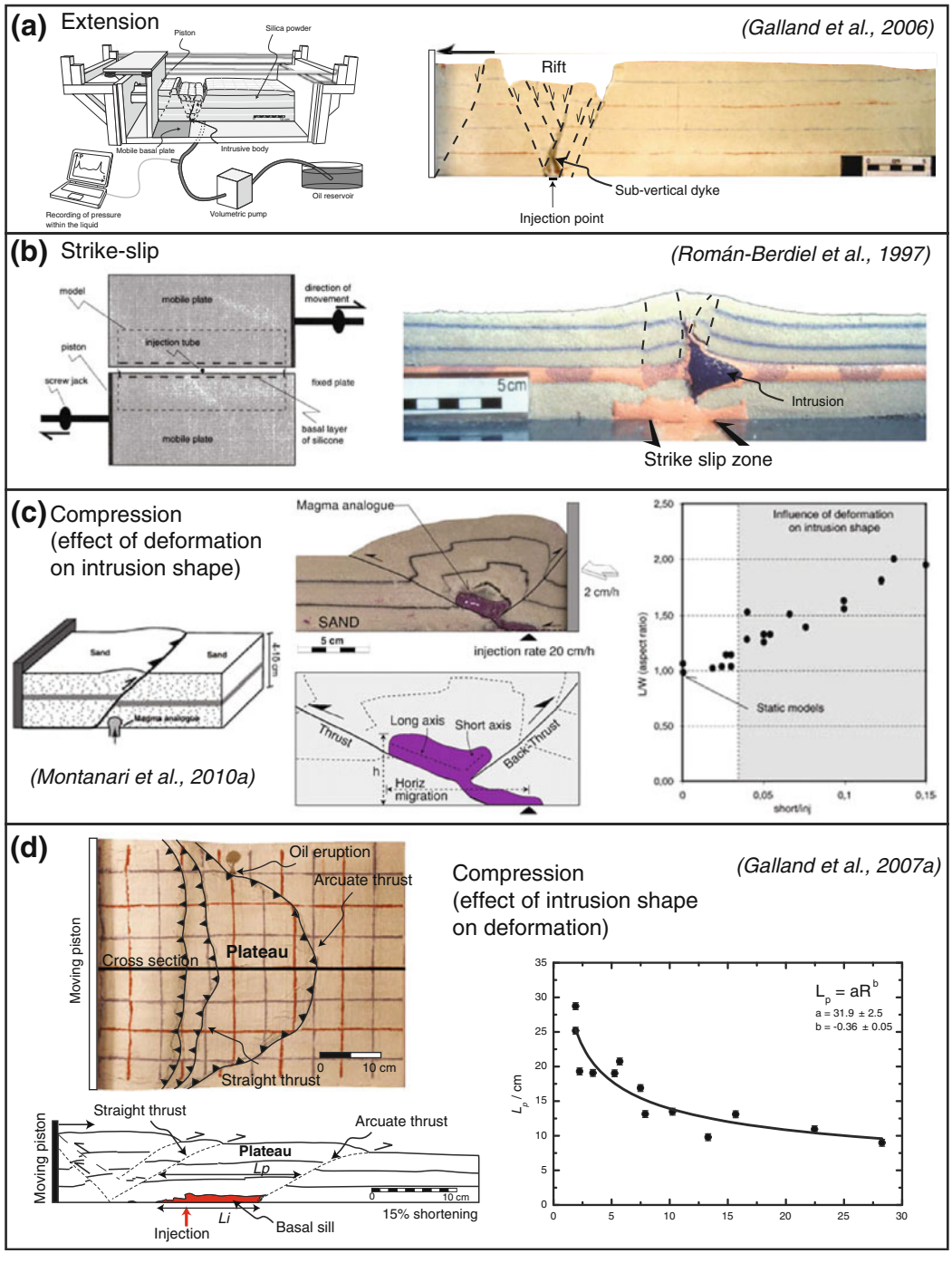
(a) Extension
(Galland et al., 2006)
Piston
Silica powder
Mobile basal plate
Intrusive body
Recording of pressure within the liquid
Volumetric pump
Oil reservoir
Rift
Sub-vertical dyke
Injection point
(b) Strike-slip
(Román-Berdiel et al., 1997)
model
mobile plate
direction of movement
injection tube
piston
screw jack
fixed plate
basal layer of silicone
mobile plate
5cm
Intrusion
Strike slip zone
(c) Compression (effect of deformation on intrusion shape)
Magma analogue
2 cm/h
SAND
5 cm
injection rate 20 cm/h
Sand
Sand
Magma analogue
4-10 cm
Long axis
Short axis
Thrust
Back-Thrust
h
Horiz migration
Influence of deformation on intrusion shape
LW (aspect ratio)
Static models
short/inj
(Montanari et al., 2010a)
(d)
Oil eruption
Arcuate thrust
Moving piston
Cross section
Plateau
0
10 cm
Straight thrust
Straight thrust
Arcuate thrust
Moving piston
Plateau
Lp
Li
Injection
Basal sill
15% shortening
Compression (effect of intrusion shape on deformation)
(Galland et al., 2007a)
$L_p = aR^b$
a = 31.9 ± 2.5
b = -0.36 ± 0.05
L_p / cm

◀ **Fig. 23** Characteristic experimental studies of magma-fault interactions in various tectonic settings. **a** Experimental study of magma intrusion in extension (Galland et al. 2006). *Left* Experimental setup. *Right* Typical longitudinal cross section, displaying the normal fault pattern and the intrusion. The latter is a dyke that follows a normal fault. **b** Experimental study of magma intrusion in strike slip (Román-Berdiel et al. 1997). *Left* Drawing of experimental setup viewed from above. *Right* Typical cross section perpendicular to the strike slip fault. **c** Experimental study of magma intrusion in compression made by using sand/silicone models (Montanari et al. 2010a). *Left* Experimental setup. *Centre* Photograph (*top*) and corresponding drawing (*bottom*) of a typical longitudinal cross section, on which the faults and the length (L) of the intrusion can be observed. Serial cross sections can also be made to reconstruct the intrusion in 3D, and so to estimate its width (W). *Right*: Correlation between the length-to-width (L/W) aspect ratio of the intrusion and the shortening velocity-to-injection velocity ratio. The plot demonstrates that the shape of the intrusion is controlled by this dynamic ratio. **d** Experimental study of magma intrusion in compression made of silica flour/vegetable oil models (Galland et al. 2007a). *Left* View of the model surface, displaying the fault trace pattern. A strongly arcuate thrust forms when oil is injected in the models. The *black straight line* locates the drawing (*bottom*) of a typical longitudinal cross section, displaying the oil intrusion and the faults. Note that the arcuate thrust is rooted at the tip of the intrusion. A non-deformed plateau lies between the arcuate thrust and the thrusts rooted at the bottom of the moving piston. Both the length of the intrusion (L_i) and of the plateau (L_p) can be measured. *Right* Correlation between the length of the plateau (L_p) and the dynamic ratio R quantifying the ratio between the shortening and injection rates. It demonstrates that the deformation pattern is strongly influenced by the occurrence of magma injection

of different rock types. They performed both 3D and 2D experiments, in which pressurised air was injected at the bottom of a pack of granular material. The initial stages of the models consisted of a bulging of the model surface and associated uplift of the granular material above the pressure source along reverse shear fractures. Following the initial doming, the pressurised air broke through to surface and fluidised the material. This produced a maar-type crater. During fluidization, material convected upward in the middle of the conduits and downward along their sides. The latter movement resulted in inward-dipping layers along the sides of the conduits. With layers of different materials, fluidization caused complex mixing of the materials and led to secondary segregation along the walls of the conduits. The top part of the model conduits exhibits a funnel shape. Although these experiments look simple, they managed to reproduce most of the first-order geological features observed in maar-diatremes and hydrothermal vent complexes, and so suggest that fluidization processes are likely to be important in the shallow parts of volcano plumbing systems.

Similar experiments addressed aspects of the formation and evolution of kimberlite pipes. Walters et al. (2006) studied the complex distribution of fluid flow across pipes filled with a mixture of granular materials. A detailed analysis of the experimental conduit morphologies shows that the fluid velocity maximised in the conduit centre and decreased towards the conduit sides following a Gaussian law. In addition, reducing the fluid flow rate reduced the size of the fluidizing conduits, leading to complex pipes-within-pipes structures, as observed in natural kimberlite pipes.

The results of Walters et al. (2006) suggest that the shape of the fluidised conduits control the complex distribution of fluid pressure and flow rate. Gernon et al. (2008) quantified this effect of conduit morphology in a series of fluidization experiments with (i) confined vertical walls, and (ii) tapered walls of varying dip angle (Fig. 24a). They show that the fluidization in vertical conduits is homogeneous, whereas fluidization in tapered conduits is heterogeneous and mainly confined to the conduit centre. In these latter experiments, the width of the fluidised region is positively correlated to the fluid flow rate. The results of Gernon et al. (2008) also show that fluctuating fluid flow during kimberlite pipe formation can produce complex internal boundaries, as observed in the field.

Analyses of kimberlite volcaniclastic deposits show that they are made of mixtures of fragments of very different sizes (from 10 mm to several cm; e.g. Walters et al. 2006). Gernon et al. (2009), and Nermoen et al. (2010b) studied the complex fluidization processes of mixtures of fine-grained and coarse-grained granular

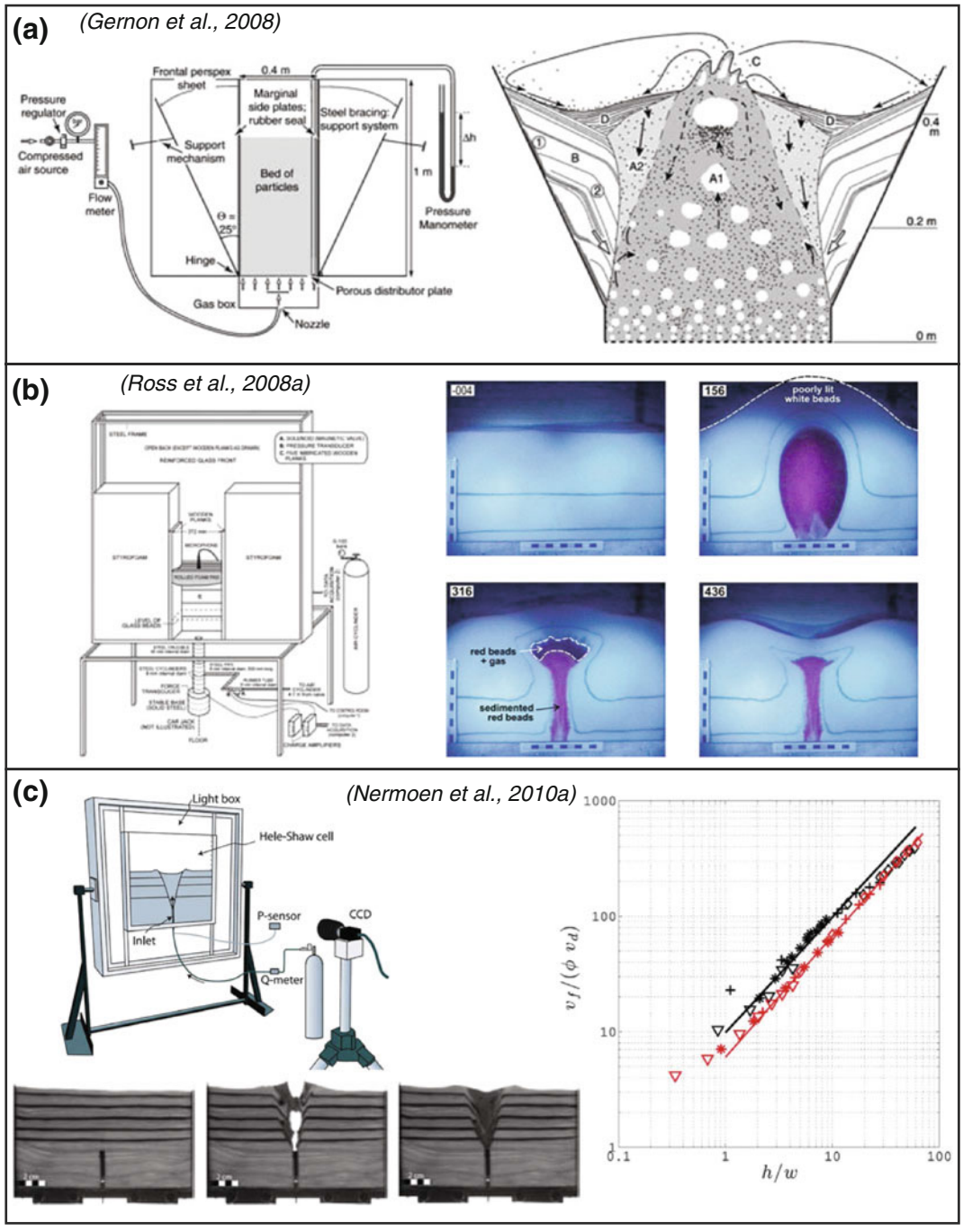
(a)
(Gernon et al., 2008)
Pressure regulator
Compressed air source
Flow meter
Frontal perspex sheet
0.4 m
Marginal side plates; rubber seal
Steel bracing; support system
Support mechanism
Bed of particles
Θ = 25°
Hinge
Gas box
Nozzle
Porous distributor plate
1 m
Δh
Pressure Manometer
C
D
D
B
A2
A1
0.4 m
0.2 m
0 m
(b)
(Ross et al., 2008a)
004
156
poorly lit white beads
316
red beads + gas
sedimented red beads
436
(c)
(Nermoen et al., 2010a)
Light box
Hele-Shaw cell
P-sensor
CCD
Inlet
Q-meter
1000
100
10
1
0.1
1
10
100
$v_f/(\phi\, v_d)$
h/w

◀ **Fig. 24** Characteristic experiments of explosive volcanic vents. **a** Experiments of Gernon et al. (2008). *Left* Drawing of experimental setup. *Right* Schematic diagram of the general behaviour of a tapered fluidised bed. The fluidised region, A is divided into (A1) a central core of dilute flow and upward particle transport, and (A2) a region dominated by the net downward movement of particles. B is the unfluidised or static region, where (1) frictional drag, and (2) shear occur at high flow rates. Particles are elutriated at C, and deposit on the surface, both at D, and the top of zone B. **b** Experiments of Ross et al. (2008a). *Left* Drawing of experimental setup. *Right* Time series of photographs of a characteristic experiment. The *upper left image* shows initial conditions. After 156 ms (*upper right image*), a 'bubble' grows, the density of the gas-particle mixture decreases as more gas arrives, and the base of the 'bubble' starts to pinch noticeably because of inward movement of granular host (*white beads*). After 316 ms (*lower left image*), *red beads* setting forms a vertical cylindrical body. After 436 ms (*lower right image*), the model exhibits the final "crater" aspect of the surface, due to subsidence of particles into the crucible underlying the rectangular container of the host (cf. Ross et al. 2008a). **c** Experiments of Nermoen et al. (2010a). *Upper left* Drawing of the experimental setup. *Lower left* Time series of photographs of an experiment, from initial state (*left*) to final state (*right*). *Right* Dimensionless plot of the critical fluid velocity at onset of fluidization v_f, scaled by the Darcy velocity of the model granular medium, against the inlet depth-to-width ratio (h/w). The graph displays experimental results (*black*) and results from analytical model (*red*), and shows a linear relationship between v_f and h/w (cf. Nermoen et al. 2010a)

materials. Their results show that fluidization of the granular mixture triggers local segregation and a concentration of coarser grains. Consequently, this locally produces a higher permeability anomaly, which focuses further fluid flow and fluidization. This self-focusing fluidization process likely explains the strong textural variations observed within kimberlite pipes.

Similar experiments with gas and granular material have been used to study the formation of phreatomagmatic underground explosions and their associated deposits. Such explosive processes have been simulated by injecting a mixture of overpressurised gas and red glass beads into a model made of white glass beads (Ross et al. 2008a, b). A high-speed camera was necessary to monitor the evolution of the models. In the early stages of the experiments, a bubble rose towards the surface, entrained the injected and host materials, and domed the surface of the models (Fig. 24b). The injected material sometimes erupted at the surface, but other times did not. The experiments show that eruption is favoured if: (i) the initial fluid pressure is high; and (ii) the thickness and the permeability of the bed into which the material is injected are low, which is in good agreement with the theoretical analysis of Jamtveit et al. (2004). In all experiments, after the fluid escaped, the red injected material appeared as a steep-sided conduit, similar to those observed in the field.

In all of the experiments mentioned above, the pressures applied to the models were large enough to form piercement structures, whether the surface was breached or not. Many volcanic conduits do not exhibit piercement structures, however. A key question is thus: what is the critical pressure required to form piercement structures? To answer this question, Nermoen et al. (2010a) injected pressurised air at the base of a bed of glass beads through an injector of variable depth (h) and width (w) (Fig. 24c). The air's pressure and velocity were gradually increased until fluidization of the bed occurred. By independently varying h and w, Nermoen et al. (2010a) established that the critical pressure for fluidization, scaled by the intrinsic permeability of the material, is a linear function of h/w. Given that the experimental results were presented in dimensionless form, they are applicable to piercement structures of different scales, from small pockmarks to kimberlite pipes.

Field studies highlight that explosive volcanic vents exhibit various shapes, regardless the origin of the explosion (magmatic, phreatomagmatic or phreatic): these shapes include vertical pipes and V-shaped vents (Jamtveit et al. 2004; Sparks et al. 2006; Svensen et al. 2007; White and Ross 2011). The integrated laboratory and numerical study of Galland et al. (2014b) demonstrates that the shape of explosive vents is governed by two dimensionless parameters, (1) the fluid pressure-to-gravitational stress ratio ($P/\rho gh$) and (2) the fluid pressure-to-host rock strength ratio (P/C). Through dimensionless phase diagrams, Galland et al. (2014b) show that

vertical vents correspond to a high-energy physical regime (high values of $P/\rho gh$ and P/C), whereas the V-shaped vents correspond to a lower-energy regime (lower values of $P/\rho gh$ and P/C). In addition, numerical simulations show that the vertical vents in the experiments result from plasticity-dominated yielding of the host rock, whereas the V-shaped vents result from elasticity-dominated failure of the overburden. In other words, V-shaped vents form as a result of obliquely propagating fractures (low energy regime), whereas vertical vents form as a result of plastic indenting (high energy regime). Though these experiments and simulations are 2-dimensional, this latter mechanism significantly differs from fracturing and is likely to explain the 3-dimensional circular shapes of vertical pipes.

5 Conclusions and Perspectives

Analogue models conducted over the past few decades have yielded a wealth of insights into most aspects of the geometric and kinematic development of sub-volcanic plumbing systems. Most works have, for practical reasons, focussed on one type of intrusion, be it dyke, sill or laccolith, but the ensemble of works allows us to make some statements on the general conditions that control intrusion type and processes. The models, taken together, have shown how the growth and final geometries of sub-volcanic intrusions are largely governed by an interplay between several key factors that include:

- the mechanical properties of the host rocks, in particular strength and elastic modulus;
- the presence or absence of heterogeneities or discontinuities, such as mechanical layering, weak interfaces or faults, within the host rocks;
- the depth of magma emplacement;
- the shape and relief of surface topography and the proximity of related topographic loads;
- the physical properties of the intruding magma(s), in particular magma viscosity and density relative to those of the surrounding host rocks.

Analogue models also show how many of the same parameters often play similar roles in the disruption and reorganisation of the plumbing system that occurs during the course of caldera collapse, related ring fault intrusion, and the re-establishment of a ‘resurgent’ magmatic system. Lastly, analogue models have also helped to unravel the complex structural and geometric effects of fluidisation and explosion that occur where magmas and magmatic fluids pass through and exit the shallowest part of the plumbing system and finally reach the surface.

(1) Despite advances from the numerous existing laboratory studies, this chapter highlights the future key challenges of experimental modelling of volcano plumbing systems. These are:
(2) A rigorous mechanical characterisation of some of the model magmas and model rocks. The properties of, e.g. ignimbrite powder, cream honey and sand-gypsum mixtures, are poorly constrained. Model magma characterisation is usually focussed on viscosity and density, but other magma properties like shear thinning, compressibility and multiphase behaviour are rarely considered.
(3) The use of model materials of complex, and more geologically relevant rheologies. Good examples are elasto-plastic cohesive granular materials, which have demonstrated their suitability and adaptability for simulating rocks of the brittle crust. In addition, currently used materials do not enable the modelling of magma—host rock interactions, such as fluidisation, fine scale fracturing, and margin cooling that may be important in developing intrusions. Thus, magma advance by fingering and/or fluidisation are currently not modelled (cf. e.g. Schofield et al. 2010), nor is the possibility of multiple injections (Menand 2008).

(4) The design of models accounting for two-phase or even three-phase magmas. The rheology of such complex materials is drastically different than those of the model magmas commonly used in the literature, which can appear somewhat simplistic.
(5) A better integration of laboratory modelling results in multidisciplinary research on volcano plumbing systems (e.g. Galland et al. 2013). This step requires rigorous dimensional analysis of the modelled processes, such that the experimental results are displayed in dimensionless form to overcome the scale problem often highlighted for laboratory models.
(6) A more quantitative description (measurements) of experimental results in order to better constrain the physics of the modelled processes and the physical laws identified from the dimensional analysis. Modern tools, such as Digital Image Correlation (White et al. 2003; Leever et al. 2011) and X-CT scanners (Adam et al. 2013) produce quantitative kinematic data sets that prove essential to unravel the complex processes simulated for the host rock (Leever et al. 2014). For better quantifying magma flow in growing or inflating intrusions more complex models, such as those of Závada et al. (2006, 2009, 2011), which used magnetic particles to track magma flow in a progressively solidifying laccolith analogue, are required. In addition, these data make the integration of laboratory models with numerical models and geological/geophysical data more quantitative.
(7) The prediction of the type and geometry of plumbing system components (e.g. dykes, sills, laccoliths, plutons, etc.). While they are mostly addressed through separate models, they all result from the intrusion of a viscous magma into a solid rock of complex rheology. The next challenge of laboratory models will be to establish a unified mechanical model of magma emplacement in the Earth's crust that predicts under which conditions intrusions of given shapes form (Galland et al. 2014a), although, as the geological system is highly variable and very complicated, this final goal will be no simple task.

References

Aarnes I, Fristad K, Planke S, Svensen H (2011a) The impact of host-rock composition on devolatilization of sedimentary rocks during contact metamorphism around mafic sheet intrusions. G3 12(10):Q10019. doi:10.1029/2011gc003636

Aarnes I, Svensen H, Polteau S, Planke S (2011b) Contact metamorphic devolatilization of shales in the Karoo Basin, South Africa, and the effects of multiple sill intrusions. Chem Geol 281(3–4):181–194. doi:10.1016/j.chemgeo.2010.12.007

Aarnes I, Podladchikov YY, Svensen H (2012) Devolatilization-induced pressure build-up: implications for reaction front movement and breccia pipe formation. Geofluids 12(4):265–279. doi:10.1111/j.1468-8123.2012.00368.x

Abdelmalak MM, Mourgues R, Galland O, Bureau D (2012) Fracture mode analysis and related surface deformation during dyke intrusion: results from 2D experimental modelling. Earth Planet Sci Lett 359–360:93–105. doi:10.1016/j.epsl.2012.10.008

Acocella V, Cifelli F, Funiciello R (2000) Analogue models of collapse calderas and resurgent domes. J Volcanol Geotherm Res 104(1–4):81–96

Acocella V, Cifelli F, Funiciello R (2001) The control of overburden thickness on resurgent domes: insights from analogue models. J Volcanol Geotherm Res 111(1–4):137–153

Acocella V, Funiciello R, Marotta E, Orsi G, de Vita S (2004) The role of extensional structures on experimental calderas and resurgence. J Volcanol Geotherm Res 129(1–3):199–217

Adam J, Klinkmüller M, Schreurs G, Wieneke B (2013) Quantitative 3D strain analysis in analogue experiments simulating tectonic deformation: integration of X-ray computed tomography and digital volume correlation techniques. J Struct Geol 55:127–149. doi:10.1016/j.jsg.2013.07.011

Algar CK, Boudreau BP, Barry MA (2011) Initial rise of bubbles in cohesive sediments by a process of viscoelastic fracture. J Geophys Res 116(B4):B04207. doi:10.1029/2010jb008133

Amelung F, Jonsson S, Zebker H, Segall P (2000) Widespread uplift and "trapdoor" faulting on Galápagos volcanoes observed with radar interferometry. Nature 407(6807):993–996. doi:10.1038/35039604

Ancochea E, Brändle JL, Huertas MJ, Cubas CR, Hernan F (2003) The felsic dikes of La Gomera (Canary Islands): identification of cone sheet and radial dike swarms. J Volcanol Geotherm Res 120(3–4):197–206

Anderson EM (1936) The dynamics of the formation of cone sheets, ring dykes and cauldron subsidences. Proc R Soc Edin 56:128–163

Barenblatt GI (2003) Scaling. Cambridge University Press, Cambridge

Barrier L, Nalpas T, Gapais D, Proust JN, Casas A, Bourquin S (2002) Influence of syntectonic sedimentation on thrust geometry. Field examples from the Iberian Chain (Spain) and analogue modelling. Sediment Geol 146(1–2):91–104

Battaglia J (2001) Quantification sismique des phénomènes magmatiques sur le Piton de la Fournaise entre 1991 et 2000. PhD thesis, Université Paris, 7 Denis Diderot, Paris

Beckett FM, Mader HM, Phillips JC, Rust AC, Witham F (2011) An experimental study of low-Reynolds-number exchange flow of two Newtonian fluids in a vertical pipe. J Fluid Mech 682:652–670. doi:10.1017/jfm.2011.264

Benn K, Odonne F, de Saint Blanquat M (1998) Pluton emplacement during transpression in brittle crust: new views from analogue experiments. Geology 26 (12):1079–1082

Benn K, Odonne F, Lee SKY, Darcovich K (2000) Analogue scale models of pluton emplacement during transpression in brittle and ductile crust. Trans R Soc Edin Earth Sci 91:111–121

Berndt C, Skogly OP, Planke S, Eldholm O, Mjelde R (2000) High-velocity breakup-related sills in the Vøring Basin, off Norway. J Geophys Res 105 (B12):28443–28454

Bonini M, Sokoutis D, Mulugeta G, Boccaletti M, Corti G, Innocenti F, Manetti P, Mazzarini F (2001) Dynamics of magma emplacement in centrifuge models of continental extension with implications for flank volcanism. Tectonics 20(6):1053–1065

Bons PD, Dougherty-Page J, Elburg MA (2001) Stepwise accumulation and ascent of magmas. J Metamorphic Geol 19(5):625–631

Boutelier D, Schrank C, Cruden A (2008) Power-law viscous materials for analogue experiments: new data on the rheology of highly-filled silicone polymers. J Struct Geol 30(3):341–353. doi:10.1016/j.jsg.2007.10.009

Branney MJ (1995) Downsag and extension at calderas: new perspectives on collapse geometries from ice-melt, mining, and volcanic subsidence. Bull Volcanol 57(5):303–318. doi:10.1007/bf00301290

Breitkreuz C, Mock A (2004) Are laccolith complexes characteristic of transtensional basin systems? Examples from the permo-carboniferous of Central Europe. Geol Soc London Spec Pub 234(1):13–31. doi:10.1144/gsl.sp.2004.234.01.03

Brèque C, Dupré J-C, Brémand F (2004) Calibration of a system of projection moiré for relief measuring: biomechanical applications. Opt Las Engin 41 (2):241–260

Brown RJ, Kavanagh J, Sparks RSJ, Tait M, Field M (2007) Mechanically disrupted and chemically weakened zones in segmented dike systems cause vent localization: evidence from kimberlite volcanic systems. Geology 35(9):815–818

Bunger AP, Cruden AR (2011) Modeling the growth of laccoliths and large mafic sills: role of magma body forces. J Geophys Res 116(B2):B02203. doi:10.1029/2010jb007648

Burchardt S, Walter TR (2010) Propagation, linkage, and interaction of caldera ring-faults: comparison between analogue experiments and caldera collapse at Miyakejima, Japan, in 2000. Bull Volcanol 72(3):297–308. doi:10.1007/s00445-009-0321-7

Burchardt S, Tanner DC, Troll VR, Krumbholz M, Gustafsson LE (2011) Three-dimensional geometry of concentric intrusive sheet swarms in the Geitafell and the Dyrföll volcanoes, eastern Iceland. G3 12(7): Q0AB09. doi:10.1029/2011gc003527

Burchardt S, Tanner D, Krumbholz M (2012) The Slaufrudalur pluton, southeast Iceland—an example of shallow magma emplacement by coupled cauldron subsidence and magmatic stoping. Geol Soc Am Bull 124(1–2):213–227. doi:10.1130/b30430.1

Burchardt S, Troll VR, Mathieu L, Emeleus HC, Donaldson CH (2013) Ardnamurchan 3D cone-sheet architecture explained by a single elongate magma chamber. Sci Rep 3. doi:10.1038/srep02891. http://www.nature.com/srep/2013/131008/srep02891/abs/srep02891.html-supplementary-information

Cagnard F, Brun J-P, Gapais D (2006) Modes of thickening of analogue weak lithospheres. Tectonophysics 421(1–2):145–160

Cañón-Tapia E, Merle O (2006) Dyke nucleation and early growth from pressurized magma chambers: insights from analogue models. J Volcanol Geotherm Res 158(3–4):207–220. doi:10.1016/j.jvolgeores.2006.05.003

Carter A, Wyk Van, de Vries B, Bachèlery P, Briole P (2006) Pits, rifts and slumps: the summit structure of Piton de la Fournaise. Bull Volc 67:741–756

Chadwick WWJ, Howard KA (1991) The pattern of circumferential and radial eruptive fissures on the volcanoes of Fernandina and Isabela islands. Galápagos. Bull Volcanol 53(4):259–275. doi:10.1007/bf00414523

Chadwick WWJ, Dieterich JH (1995) Mechanical modeling of cirumferential and radial dike intrusion on Galápagos volcanoes. J Volcanol Geotherm Res 66:37–52

Chadwick WWJ, Jonsson S, Geist DJ, Poland M, Johnson DJ, Batt S, Harpp KS, Ruiz A (2011) The May 2005 eruption of Fernandina volcano, Galápagos: the first circumferential dike intrusion observed by GPS and InSAR. Bull Volcanol 73(6):679–697. doi:10.1007/s00445-010-0433-0

Chanceaux L, Menand T (2014) Solidification effects on sill formation: an experimental approach. Earth Planet Sci Lett 403:79–88. doi:10.1016/j.epsl.2014.06.018

Chang W-L, Smith RB, Wicks C, Farrell JM, Puskas CM (2007) Accelerated uplift and magmatic intrusion of the Yellowstone caldera, 2004 to 2006. Science 318 (5852):952–956. doi:10.1126/science.1146842

Chevallier L, Woodford A (1999) Morpho-tectonics and mechanism of emplacement of the dolerite rings and sills of the western Karoo, South Africa. South Afr J Geol 102(1):43–54

Clough CT, Maufe HB, Bailey EB (1909) The cauldron subsidence of glencoe and the associated igneous phenomena. J Geol Soc London 65:611–678

Cobbold PR, Jackson MPA (1992) Gum rosin (colophony): a suitable material for thermomechanical modelling of the lithosphere. Tectonophysics 210(3–4):255–271. doi:10.1016/0040-1951(92)90325-Z

Cole JW, Milner DM, Spinks KD (2005) Calderas and caldera structures: a review. Earth-Sci Rev 69(1–2):1–26. doi:10.1016/j.earscirev.2004.06.004

Corry CE (1988) Laccoliths; mechanisms of emplacement and growth, vol 220. Geological Society of America Special Paper

Corti G, Bonini M, Innocenti F, Manetti P, Mulugeta G (2001) Centrifuge models simulating magma emplacement during oblique rifting. J Geodyn 31:557–576

Corti G, Bonini M, Conticelli S, Innocenti F, Manetti P, Sokoutis D (2003) Analogue modelling of continental extension: a review focused on the relations between the patterns of deformation and the presence of magma. Earth-Sci Rev 63(3–4):169–247

Corti G, Moratti G, Sani F (2005) Relations between surface faulting and granite intrusions in analogue models of strike-slip deformation. J Struct Geol 27 (9):1547–1562

Crumpler LS, Head JW, Aubele JC (1996) Calderas on Mars: characteristics, structure, and associated flank deformation. Geol Soc Lond Spec Pub 110(1):307–348. doi:10.1144/gsl.sp.1996.110.01.24

Dahm T (2000) Numerical simulations of the propagation path and the arrest of fluid-filled fractures in the Earth. Geophys J Int 141(3):623–638

Daniels KA, Menand T (2015) An experimental investigation of dyke injection under regional extensional stress. J Geophys Res: Solid Earth JB011627. doi:10.1002/2014jb011627

Daniels KA, Kavanagh JL, Menand T, R. Stephen JS (2012) The shapes of dikes: evidence for the influence of cooling and inelastic deformation. Geol Soc Am Bull 124(7–8):1102–1112. doi:10.1130/b30537.1

Daubrée A (1891) Recherches expérimentales sur le rôle possible des gaz à hautes températures doués de très fortes pressions et animés d'un mouvement fort rapide dans divers phénomènes géologiques. Bulletin de la Société géologique de France 19:313–354

de Bremond d'Ars J, Arndt NT, Hallot E (2001) Analog experimental insights into the formation of magmatic sulfide deposits. Earth Planet Sci Lett 186(3–4):371–381. doi:10.1016/S0012-821X(01)00254-0

de Saint-Blanquat M, Habert G, Horsman E, Morgan SS, Tikoff B, Launeau P, Gleizes G (2006) Mechanisms and duration of non-tectonically assisted magma emplacement in the upper crust: the Black Mesa pluton, Henry Mountains, Utah. Tectonophysics 428 (1–4):1–31. doi:10.1016/j.tecto.2006.07.014

Delaney PT, Pollard DD (1981) Deformation of host rocks and flow of magma during growth of Minette dikes and breccia-bearing intrusions near Ship Rock, New Mexico, vol 1202. U.S. Geological Survey Professional Paper

Delcamp A, Troll VR, Wyk de Vries B, Carracedo JC, Petronis MS, Pérez-Torrado FJ, Deegan FM (2012a) Dykes and structures of the NE rift of Tenerife, Canary Islands: a record of stabilisation and destabilisation of ocean island rift zones. Bull Volcanol 74 (5):963–980. doi:10.1007/s00445-012-0577-1

Delcamp A, Wyk de Vries B, James MR, Gailler LS, Lebas E (2012b) Relationships between volcano gravitational spreading and magma intrusion. Bull Volcanol 74(3):743–765. doi:10.1007/s00445-011-0558-9

Di Giuseppe E, Funiciello F, Corbi F, Ranalli G, Mojoli G (2009) Gelatins as rock analogs: a systematic study of their rheological and physical properties. Tectonophysics 473(3–4):391–403. doi:10.1016/j.tecto.2009.03.012

Dingwell DB, Bagdassarov NS, Bussov GY, Webb SL (1993) Magma rheology. In: Luth RW (ed) Experiments at high pressure and applications to the Earth's mantle, vol 21. Mineralogists Association of Canada Short Course Handbook, pp 131–196

Dixon JM, Simpson DG (1987) Centrifuge modelling of laccolith intrusion. J Struct Geol 9:87–103

Djabourov M, Leblond J, Papon P (1988a) Gelation of aqueous gelatin solutions. I. Structural investigation. J Phys France 49(2):319–332

Djabourov M, Leblond J, Papon P (1988b) Gelation of aqueous gelatin solutions. II. Rheology of the sol-gel transition. J Phys France 49(2):333–343

Donnadieu F, Kelfoun K, van Wyk de Vries B, Cecchi E, Merle O (2003) Digital photogrammetry as a tool in analogue modelling: applications to volcano instability. J Volcanol Geotherm Res 123(1–2):161–180. doi:10.1016/s0377-0273(03)00034-9

Donnadieu F, Merle O (1998) Experiments on the indentation process during cryptodome intrusions: new insights into Mount St. Helens deformation. Geology 26(1):79–82

Donnadieu F, Merle O (2001) Geometrical constraints of the 1980 Mount St. Helens intrusion from analogue models. Geophys Res Lett 28(4):639–642. doi:10.1029/2000gl011869

Druitt TH, Sparks RSJ (1984) On the formation of calderas during ignimbrite eruptions. Nature 310:679–681

Dupré JC, Lagarde A (1997) Photoelastic analysis of a three-dimensional specimen by optical slicing and digital image processing. Exp Mech 37(4):393–397. doi:10.1007/bf02317303

Dupré JC, Valle V, Jarny S, Monnet P (2010) Fringe analysis by phase shifting technique for birefringent fluid studies. Opt Las Engin 48(1):37–42. doi:10.1016/j.optlaseng.2009.07.015

Einstein A (1906) Eine neue Bestimmung der Moleküldimensionen. Ann Phys 324(2):289–306. doi:10.1002/andp.19063240204

Ferré E, Galland O, Montanari D, Kalakay T (2012) Granite magma migration and emplacement along thrusts. International J Earth Sci 1–16. doi:10.1007/s00531-012-0747-6

Fiske RS, Jackson ED (1972) Orientation and growth of Hawaiian volcanic rifts: the effect of regional structure and gravitational stresses. Proc R Soc Lond Ser A (Math Phys Sci) 329(1578):299–326

Fouqué F (1879) Santorin et ses éruptions. G. Masson

Francis EH (1982) Magma and sediment—I. Emplacement mechanism of late Carboniferous tholeiite sills in northern Britain. J Geol Soc London 139(1):1–20

Fukushima Y, Cayol V, Durand P, Massonnet D (2010) Evolution of magma conduits during the 1998–2000 eruptions of Piton de la Fournaise volcano, Réunion Island. J Geophys Res 115(B10):B10204. doi:10.1029/2009jb007023

Galerne CY, Galland O, Neumann ER, Planke S (2011) 3D relationships between sills and their feeders: evidence from the Golden Valley Sill Complex (Karoo Basin) and experimental modelling. J Volcanol Geotherm Res 202(3–4):189–199. doi:10.1016/j.jvolgeores.2011.02.006

Galland O (2005) Interactions mécaniques entre la tectonique compressive et le magmatisme: expériences analogiques et exemple naturel. PhD thesis, Université de Rennes1, Mémoires de Géosciences-Rennes, n°116

Galland O (2012) Experimental modelling of ground deformation associated with shallow magma intrusions. Earth Planet Sci Lett 317–318:145–156. doi:10.1016/j.epsl.2011.10.017

Galland O, Scheibert J (2013) Analytical model of surface uplift above axisymmetric flat-lying magma intrusions: implications for sill emplacement and geodesy. J Volcanol Geotherm Res 253:114–130. doi:10.1016/j.jvolgeores.2012.12.006

Galland O, de Bremond d'Ars J, Cobbold PR, Hallot E (2003) Physical models of magmatic intrusion during thrusting. Terra Nova 15:405–409

Galland O, Cobbold PR, Hallot E, de Bremond d'Ars J, Delavaud G (2006) Use of vegetable oil and silica powder for scale modelling of magmatic intrusion in a deforming brittle crust. Earth Planet Sci Lett 243:786–804

Galland O, Cobbold PR, de Bremond d'Ars J, Hallot E (2007a) Rise and emplacement of magma during horizontal shortening of the brittle crust: Insights from experimental modeling. J Geophys Res 112. doi:10.1029/2006JB004604

Galland O, Hallot E, Cobbold PR, Ruffet G, de Bremond d'Ars J (2007b) Volcanism in a compressional Andean setting: a structural and geochronological study of Tromen volcano (Neuquén province, Argentina). Tectonics 26:TC4010. doi:10.1029/2006TC002011

Galland O, Cobbold PR, Hallot E, De Bremond d'Ars J (2008) Magma-controlled tectonics in compressional settings: insights from geological examples and experimental modelling. Bolletino della Società Geologica Italiana 127(2):205–208

Galland O, Planke S, Neumann ER, Malthe-Sørenssen A (2009) Experimental modelling of shallow magma emplacement: application to saucer-shaped intrusions. Earth Planet Sci Lett 277(3–4):373–383

Galland O, Burchardt S, Troll VR (2013) Volcanic and igneous plumbing systems: state-of-the-art and future developments. Eos, Trans Am Geophys Union 94 (18):169. doi:10.1002/2013eo180008

Galland O, Burchardt S, Hallot E, Mourgues R, Bulois C (2014a) Dynamics of dikes versus cone sheets in volcanic systems. J Geophys Res: Solid Earth JB011059. doi:10.1002/2014jb011059

Galland O, Gisler GR, Haug ØT (2014b) Morphology and dynamics of explosive vents through cohesive rock formations. J Geophys Res 119. doi:10.1002/2014JB011050

Gernon TM, Gilbertson MA, Sparks RSJ, Field M (2008) Gas-fluidisation in an experimental tapered bed: insights into processes in diverging volcanic conduits. J Volcanol Geotherm Res 174(1–3):49–56. doi:10.1016/j.jvolgeores.2007.12.034

Gernon TM, Gilbertson MA, Sparks RSJ, Field M (2009) The role of gas-fluidisation in the formation of massive volcaniclastic kimberlite. Lithos 112 Supplement 1(0):439–451. doi:10.1016/j.lithos.2009.04.011

Geshi N, Acocella V, Ruch J (2012) From structure- to erosion-controlled subsiding calderas: evidence thresholds and mechanics. Bull Volcanol 74 (6):1553–1567. doi:10.1007/s00445-012-0617-x

Geshi N, Shimano T, Chiba T, Nakada S (2002) Caldera collapse during the 2000 eruption of Miyakejima Volcano, Japan. Bull Volcanol 64(1):55–68. doi:10.1007/s00445-001-0184-z

Geyer A, Folch A, Martí J (2006) Relationship between caldera collapse and magma chamber withdrawal: an experimental approach. J Volcanol Geotherm Res 157 (4):375–386. doi:10.1016/j.jvolgeores.2006.05.001

Geyer A, Martí J (2008) The new worldwide collapse caldera database (CCDB): a tool for studying and understanding caldera processes. J Volcanol Geotherm Res 175(3):334–354. doi:10.1016/j.jvolgeores.2008.03.017

Gilbert GK (1877) Report on the geology of the Henry Mountains. U.S. Geographical and Geological Survey, Rocky Mountain Region (Powel)

Girard G, van Wyk de Vries B (2005) The Managua Graben and Las Sierras-Masaya volcanic complex (Nicaragua); pull-apart localization by an intrusive complex: results from analogue modeling. J Volcanol Geotherm Res 144(1–4):37–57. doi:10.1016/j.jvolgeores.2004.11.016

Goulty NR, Schofield N (2008) Implications of simple flexure theory for the formation of saucer-shaped sills. J Struct Geol 30(7):812–817

Gressier JB, Mourgues R, Bodet L, Matthieu JY, Galland O, Cobbold PR (2010) Control of pore fluid pressure on depth of emplacement of magmatic sills: an experimental approach. Tectonophysics 489(1–4): 1–13

Grosse P, van Wyk de Vries B, Euillades PA, Kervyn M, Petrinovic IA (2012) Systematic morphometric characterization of volcanic edifices using digital elevation models. Geomorphology 136(1):114–131. doi:10.1016/j.geomorph.2011.06.001

Grout FF (1945) Scale models of structures related to batholiths. Am J Sci 243A:260–284

Hailemariam H, Mulugeta G (1998) Temperature-dependent rheology of bouncing putties used as rock analogs. Tectonophysics 294(1–2):131–141. doi:10.1016/S0040-1951(98)00124-3

Hall J (1815) II. On the Vertical Position and Convolutions of certain Strata, and their relation with Granite. Earth Environ Sci Trans R Soc Edinburgh 7(1):79–108. doi:10.1017/S0080456800019268

Hallot E, Auvray B, de Bremond d'Ars J, Martin H, Davy P (1994) New injection experiments in non-Newtonian fluids. Terra Nova 6(3):274–281. doi:10.1111/j.1365-3121.1994.tb00495.x

Hallot E, Davy P, de Bremond d'Ars J, Auvray B, Martin H, Van Damme H (1996) Non-Newtonian effects during injection in partially crystallised magmas. J Volcanol Geotherm Res 71(1):31–44

Hansen DM, Cartwright JA (2006a) Saucer-shaped sill with lobate morphology revealed by 3D seismic data: implications for resolving a shallow-level sill emplacement mechanism. J Geol Soc London 163:509–523

Hansen DM, Cartwright JA (2006b) The three-dimensional geometry and growth of forced folds above saucer-shaped igneous sills. J Struct Geol 28(8):1520–1535

Hansen DM, Redfern J, Federici F, di Biase D, Bertozzi G (2008) Miocene igneous activity in the Northern Subbasin, offshore Senegal, NW Africa. Mar Pet Geol 25(1):1–15

Hansen VL, Olive A (2010) Artemis, Venus: the largest tectonomagmatic feature in the solar system? Geology 38(5):467–470

Haug ØT, Galland O, Gisler GR (2013) Experimental modelling of fragmentation applied to volcanic explosions. Earth Planet Sci Lett 384:188–197. doi:10.1016/j.epsl.2013.10.004

Hayashi Y, Morita Y (2003) An image of a magma intrusion process inferred from precise hypocentral migrations of the earthquake swarm east of the Izu Peninsula. Geophys J Int 153(1):159–174. doi:10.1046/j.1365-246X.2003.01892.x

Hildreth W, Fierstein J (2000) Katmai volcanic cluster and the great eruption of 1912. Geol Soc Am Bull 112 (10):1594–1620. doi:10.1130/0016-7606(2000)112<1594:kvcatg>2.0.co;2

Hildreth W, Wilson CJN (2007) Compositional Zoning of the Bishop Tuff. J Petrol 48(5):951–999. doi:10.1093/petrology/egm007

Holland M, Urai JL, Martel S (2006) The internal structure of fault zones in basaltic sequences. Earth Planet Sci Lett 248(1–2):301–315

Holohan EP, Troll VR, Walter TR, Munn S, McDonnell S, Shipton ZK (2005) Elliptical calderas in active tectonic settings: an experimental approach. J Volcanol Geotherm Res 144(1–4):119–136

Holohan EP, Troll VR, van Wyk de Vries B, Walsh JJ, Walter TR (2008a) Unzipping Long Valley: an explanation for vent migration patterns during an elliptical ring fracture eruption. Geology 36(4):323–326. doi:10.1130/g24329a.1

Holohan EP, Wyk de Vries B, Troll VR (2008b) Analogue models of caldera collapse in strike-slip tectonic regimes. Bull Volcanol 70(7):773–796. doi:10.1007/s00445-007-0166-x

Holohan EP, Troll VR, Errington M, Donaldson CH, Nicoll GR, Emeleus CH (2009) The Southern Mountains Zone, Isle of Rum, Scotland: volcanic and sedimentary processes upon an uplifted and subsided magma chamber roof. Geol Mag 146(3):400

Holohan EP, Schöpfer MPJ, Walsh JJ (2011) Mechanical and geometric controls on the structural evolution of pit crater and caldera subsidence. J Geophys Res 116 (B7):B07202. doi:10.1029/2010jb008032

Holohan EP, Walter TR, Schöpfer MPJ, Walsh JJ, van Wyk de Vries B, Troll VR (2013) Origins of oblique-slip faulting during caldera subsidence. J Geophys Res 118(4):1778–1794. doi:10.1002/jgrb.50057

Hubbert MK (1937) Theory of scale models as applied to the study of geologic structures. Geol Soc Am Bull 48:1459–1520

Hubbert MK, Willis DG (1957) Mechanics of hydraulic fracturing. In: Hubbert MK (ed) Structural geology. Hafner Publishing Company, New York, pp 175–190

Hyndman DW, Alt D (1987) Radial dikes, laccoliths, and gelatin models. J Geol 95:763–774

Ito G, Martel SJ (2002) Focusing of magma in the upper mantle through dike interaction. J Geophys Res 107 (B10):2223. doi:10.1029/2001jb000251

Jackson CAL, Schofield N, Golenkov B (2013) Geometry and controls on the development of igneous sill-related forced-folds: a 2D seismic reflection case study from offshore southern Australia. Geol Soc Am Bull 125(11–12):1874–1890

Jackson MD, Pollard DD (1990) Flexure and faulting of sedimentary host rocks during growth of igneous domes, Henry Mountains, Utah. J Struct Geol 12 (2):185–206

Jaeger JC, Cook NGW, Zimmerman RW (2009) Fundamentals of rock mechanics. Blackwell Publishing Ltd., Oxford

Jamtveit B, Svensen H, Podladchikov YY, Planke S (2004) Hydrothermal vent complexes associated with sill intrusions in sedimentary basins. In: Breitkreuz C, Petford N (eds) Physical geology of high-level magmatic systems, vol 234. Geological Society, London, Special Publication, London, pp 233–241

Johnson AM (1970) Physical processes in geology. Freeman, Cooper & Company, San Francisco

Johnson AM, Pollard DD (1973) Mechanics of growth of some laccolithic intrusions in the Henry Mountains, Utah, I. Field observations, Gilbert's model, physical properties and flow of the magma. Tectonophysics 18:261–309

Kalakay TJ, John BE, Lageson DR (2001) Fault-controlled pluton emplacement in the Sevier fold-and-thrust belt of southern Montana. J Struct Geol 23:1151–1165

Kavanagh JL, Menand T, Daniels KA (2013) Gelatine as a crustal analogue: determining elastic properties for modelling magmatic intrusions. Tectonophysics 582:101–111. doi:10.1016/j.tecto.2012.09.032

Kavanagh JL, Menand T, Sparks RSJ (2006) An experimental investigation of sill formation and propagation in layered elastic media. Earth Planet Sci Lett 245(3–4): 799–813

Kavanagh JL, Sparks RSJ (2011) Insights of dyke emplacement mechanics from detailed 3D dyke thickness datasets. J Geol Soc London 168(4):965–978. doi:10.1144/0016-76492010-137

Kennedy B, Stix J, Vallance JW, Lavallée Y, Longpré M-A (2004) Controls on caldera structure: results from analogue sandbox modeling. Geol Soc Am Bull 116 (5–6):515–524. doi:10.1130/b25228.1

Kennedy BM, Jellinek AM, Stix J (2008) Coupled caldera subsidence and stirring inferred from analogue models. Nature Geo 1(6):385–389

Kennedy B, Wilcock J, Stix J (2012) Caldera resurgence during magma replenishment and rejuvenation at Valles and Lake City calderas. Bull Volcanol 74 (8):1833–1847. doi:10.1007/s00445-012-0641-x

Kervyn M, Boone MN, van Wyk de Vries B, Lebas E, Cnudde V, Fontijn K, Jacobs P (2010) 3D imaging of volcano gravitational deformation by computerized X-ray micro-tomography. Geosphere 6(5):482–498. doi:10.1130/ges00564.1

Kervyn M, Ernst GGJ, van Wyk de Vries B, Mathieu L, Jacobs P (2009) Volcano load control on dyke propagation and vent distribution: insights from analogue modeling. J Geophys Res 114(B3):B03401. doi:10.1029/2008jb005653

Kettermann M, Urai JL (2015) Changes in structural style of normal faults due to failure mode transition: first results from excavated scale models. J Struct Geol 74:105–116. doi:10.1016/j.jsg.2015.02.013

Klausen MB (2004) Geometry and mode of emplacement of the Thverartindur cone sheet swarm, SE Iceland. J Volcanol Geotherm Res 138(3–4):185–204

Komuro H (1987) Experiments on cauldron formation: a polygonal cauldron and ring fractures. J Volcanol Geotherm Res 31(1–2):139–149

Komuro H, Fujita Y, Kodama K (1984) Numerical and experimental models on the formation mechanism of collapse basins during the Green Tuff orogenesis of Japan. Bull Volcanol 47(3):649–666. doi:10.1007/bf01961233

Koyaguchi T, Takada A (1994) An experimental study on the formation of composite intrusions from zoned magma chambers. J Volcanol Geotherm Res 59 (4):261–267. doi:10.1016/0377-0273(94)90081-7

Lageson DR, Schmitt JG, Horton BK, Kalakay TJ, Burton BR (2001) Influence of Late Cretaceous magmatism on the Sevier orogenic wedge, western Montana. Geology 29:723–726

Lavallée Y, Stix J, Kennedy B, Richer M, Longpré M-A (2004) Caldera subsidence in areas of variable topographic relief: results from analogue modeling. J Volcanol Geotherm Res 129(1–3):219–236. doi:10.1016/S0377-0273(03)00241-5

Le Corvec N, Menand T, Lindsay J (2013) Interaction of ascending magma with pre-existing crustal fractures in monogenetic basaltic volcanism: an experimental approach. J Geophys Res: Solid Earth 118(3):968–984. doi:10.1002/jgrb.50142

Leever KA, Gabrielsen RH, Sokoutis D, Willingshofer E (2011) The effect of convergence angle on the kinematic evolution of strain partitioning in transpressional brittle wedges: insight from analog modeling and high-resolution digital image analysis. Tectonics 30(2):TC2013. doi:10.1029/2010tc002823

Leever KA, Galland O, Acocella V (2014) The Science behind laboratory-scale models of the earth. Eos, Trans Am Geophys Union 95(3):30. doi:10.1002/2014eo030008

Legrand D, Calahorrano A, Guillier B, Rivera L, Ruiz M, Villagomez D, Yepes H (2002) Stress tensor analysis of the 1998-1999 tectonic swarm of northern Quito related to the volcanic swarm of Guagua Pichincha volcano, Ecuador. Tectonophysics 344(1–2):15–36

Lipman PW (1984) The roots of ash flow calderas in western North America: windows into the tops of granitic batholiths. J Geophys Res 89(B10):8801–8841. doi:10.1029/JB089iB10p08801

Lipman PW (1997) Subsidence of ash-flow calderas: relation to caldera size and magma-chamber geometry. Bull Volcanol 59(3):198–218. doi:10.1007/s004450050186

Lipman PW, Moore JG, Swanson DA (1981) bulging of the north flank before the May 18 eruption: geodetic data. US Geol Surv Prof Pap 1250:143–156

Lister JR, Kerr RC (1991) Fluid-mechanical models of crack propagation and their application to magma transport in dykes. J Geophys Res 96(B6):10049–10077

Llambías EJ, Leanza HA, Galland O (2011) Agrupamiento volcánico Tromen-Tilhue. Paper presented at the Geologia y recursos naturales de la Provincia del Neuquén, XVIII Congreso Geologico Argentino, Relatorio, Neuquén, Argentina

Lohrmann J, Kukowski N, Adam J, Onken O (2003) The impact of analogue materials properties on the geometry, kinematics, and dynamics of convergent sand wedges. J Struct Geol 25:1691–1711

Lorenz V, Kurszlaukis S (2007) Root zone processes in the phreatomagmatic pipe emplacement model and consequences for the evolution of maar-diatreme volcanoes. J Volcanol Geotherm Res 159(1–3):4–32. doi:10.1016/j.jvolgeores.2006.06.019

Maaløe S (1987) The generation and shape of feeder dykes from mantle sources. Contr Mineral and Petrol 96(1):47–55. doi:10.1007/bf00375524

Magee C, Jackson CAL, Schofield N (2014) Diachronous sub-volcanic intrusion along deep-water margins:

insights from the Irish Rockall Basin. Basin Res 26 (1):85–105. doi:10.1111/bre.12044
Maillot B (2013) A sedimentation device to produce uniform sand packs. Tectonophysics 593:85–94. doi:10.1016/j.tecto.2013.02.028
Malthe-Sørenssen A, Planke S, Svensen H, Jamtveit B (2004) Formation of saucer-shaped sills. In: Breitkreuz C, Petford N (eds) Physical geology of high-level magmatic systems, vol 234. Geological Society of London Special Publication, London, pp 215–227
Marques FO, Cobbold PR (2006) Effects of topography on the curvature of fold-and-thrust belts during shortening of a 2-layer model of continental lithosphere. Tectonophysics 415(1–4):65–80
Martí J, Ablay GJ, Redshaw LT, Sparks RSJ (1994) Experimental studies of collapse calderas. J Geol Soc London 151(6):919–929. doi:10.1144/gsjgs.151.6.0919
Mastin LG, Pollard DD (1988) Surface deformation and shallow dike intrusion processes at Inyo craters, Long Valley, California. J Geophys Res 93(B11):13221–13235
Mathieu L, van Wyk de Vries B (2009) Edifice and substrata deformation induced by intrusive complexes and gravitational loading in the Mull volcano (Scotland). Bull Volcanol 71(10):1133–1148. doi:10.1007/s00445-009-0295-5
Mathieu L, van Wyk de Vries B (2011) The impact of strike-slip, transtensional and transpressional fault zones on volcanoes. Part1: scaled experiments. J Struct Geol 33(5):907–917. doi:10.1016/j.jsg.2011.03.002
Mathieu L, van Wyk de Vries B, Holohan EP, Troll VR (2008) Dykes, cups, saucers and sills: analogue experiments on magma intrusion into brittle rocks. Earth Planet Sci Lett 271(1–4):1–13
Mathieu L, van Wyk de Vries B, Pilato M, Troll VR (2011) The interaction between volcanoes and strike-slip, transtensional and transpressional fault zones: analogue models and natural examples. J Struct Geol 33(5):898–906. doi:10.1016/j.jsg.2011.03.003
Mazzarini F, Musumeci G, Montanari D, Corti G (2010) Relations between deformation and upper crustal magma emplacement in laboratory physical models. Tectonophysics 484(1–4):139–146
Mazzini A, Nermoen A, Krotkiewski M, Podladchikov Y, Planke S, Svensen H (2009) Strike-slip faulting as a trigger mechanism for overpressure release through piercement structures. Implications for the Lusi mud volcano, Indonesia. Mar Pet Geol 26(9):1751–1765
McBirney AR (1990) An historical note on the origin of calderas. J Volcanol Geotherm Res 42(3):303–306
McCallum ME (1985) Experimental evidence for fluidization processes in breccia pipe formation. Econ Geol 80(6):1523–1543. doi:10.2113/gsecongeo.80.6.1523
McClay KR (1976) The rheology of plasticine. Tectonophysics 33(1–2):T7–T15. doi:10.1016/0040-1951(76)90047-0
McGuire WJ, Pullen AD (1989) Location and orientation of eruptive fissures and feeder dykes at Mount Etna; influence of gravitational and regional tectonic stress regimes. J Volcanol Geotherm Res 38(3–4):325–344
McLeod P, Tait S (1999) The growth of dykes from magma chambers. J Volcanol Geotherm Res 92:231–245
Menand T (2008) The mechanics and dynamics of sills in layered elastic rocks and their implications for the growth of laccoliths and other igneous complexes. Earth Planet Sci Lett 267(1–2):93–99
Menand T, Daniels KA, Benghiat P (2010) Dyke propagation and sill formation in a compressive tectonic environment. J Geophys Res 115. doi:10.1029/2009JB006791
Menand T, Tait S (2001) A phenomenological model for precursor volcanic eruptions. Nature 411:678–680
Menand T, Tait S (2002) The propagation of a buoyant liquid-filled fissure from a source under constant pressure: an experimental approach. J Geophys Res 107(B11):2306
Merle O, Borgia A (1996) Scaled experiments of volcanic spreading. J Geophys Res 101(B6):13, 805–813, 817
Merle O, Donnadieu F (2000) Indentation of volcanic edifices by the ascending magma. Geol Soc London Spec Pub 174(1):43–53. doi:10.1144/gsl.sp.1999.174.01.03
Merle O, Vendeville B (1995) Experimental modelling of thin-skinned shortening around magmatic intrusions. Bull Volcanol 57:33–43
Michel J, Baumgartner L, Putlitz B, Schaltegger U, Ovtcharova M (2008) Incremental growth of the Patagonian Torres del Paine laccolith over 90 k.y. Geology 36(6):459–462. doi:10.1130/g24546a.1
Michon L, Massin F, Famin V, Ferrazzini V, Roult G (2011) Basaltic calderas: collapse dynamics, edifice deformation, and variations of magma withdrawal. J Geophys Res 116(B3):B03209. doi:10.1029/2010jb007636
Montanari D, Corti G, Sani F, Ventisette CD, Bonini M, Moratti G (2010a) Experimental investigation on granite emplacement during shortening. Tectonophysics 484(1–4):147–155
Montanari D, Corti G, Simakin A (2010b) Magma chambers and localization of deformation during thrusting. Terra Nova 22(5):390–395. doi:10.1111/j.1365-3121.2010.00962.x
Moore I, Kokelaar P (1998) Tectonically controlled piecemeal caldera collapse: a case study of Glencoe volcano. Scotland. Geol Soc Am Bull 110(11):1448–1466. doi:10.1130/0016-7606(1998)110<1448:tcpcca>2.3.co;2
Morgan SS, Stanik A, Horsman E, Tikoff B, de Saint Blanquat M, Habert G (2008) Emplacement of multiple magma sheets and wall rock deformation: Trachyte Mesa intrusion, Henry Mountains, Utah. J Struct Geol 30(4):491–512. doi:10.1016/j.jsg.2008.01.005
Mori J, McKee C (1987) Outward-dipping ring-fault structure at Rabaul Caldera as shown by earthquake locations. Science 235(4785):193–195. doi:10.1126/science.235.4785.193

Mourgues R, Bureau D, Bodet L, Gay A, Gressier JB (2012) Formation of conical fractures in sedimentary basins: experiments involving pore fluids and implications for sandstone intrusion mechanisms. Earth Planet Sci Lett 313–314:67–78. doi:10.1016/j.epsl.2011.10.029

Mourgues R, Cobbold PR (2003) Some tectonic consequences of fluid overpressures and seepage forces as demonstrated by sandbox modelling. Tectonophysics 376:75–97

Muller JR, Ito G, Martel SJ (2001) Effects of volcano loading on propagation in an elastic half-space. J Geophys Res 106:11101–11113

Musumeci G, Mazzarini F, Corti G, Barsella M, Montanari D (2005) Magma emplacement in a thrust ramp anticline: the Gavorrano Granite (northern Apennine, Italy). Tectonics 24. doi:10.1029/2005TC001801

Nakamura K (1977) Volcanoes as possible indicators of tectonic stress orientation–principle and proposal. J Volcanol Geotherm Res 2(1):1–16

Nermoen A, Galland O, Jettestuen E, Fristad K, Podladchikov YY, Svensen H, Malthe-Sørenssen A (2010a) Experimental and analytic modeling of piercement structures. J Geophys Res 115(B10):B10202. doi:10.1029/2010jb007583

Nermoen A, Raufaste C, deVilliers SD, Jettestuen E, Meakin P, Dysthe DK (2010b) Morphological transitions in partially gas-fluidized granular mixtures. Phys Rev E 81(6):061305

Norini G, Acocella V (2011) Analogue modeling of flank instability at Mount Etna: understanding the driving factors. Journal of Geophysical Research: Solid Earth 116(B7):B07206. doi:10.1029/2011jb008216

O'Driscoll B, Troll VR, Reavy RJ, Turner P (2006) The Great Eucrite intrusion of Ardnamurchan, Scotland: reevaluating the ring-dike concept. Geology 34 (3):189–192

Odé H (1957) Mechanical analysis of the dike pattern of the Spanish Peaks area, Colorado. Geol Soc Am Bull 68:567–576

Pallister JS, McCausland WA, Jonsson S, Lu Z, Zahran HM, Hadidy SE, Aburukbah A, Stewart ICF, Lundgren PR, White RA, Moufti MRH (2010) Broad accommodation of rift-related extension recorded by dyke intrusion in Saudi Arabia. Nature Geosci 3 (10):705–712. doi:http://www.nature.com/ngeo/journal/v3/n10/abs/ngeo966.html#supplementary-information

Panien M, Schreurs G, Pfiffner A (2006) Mechanical behaviour of granular materials used in analogue modelling: insights from grain characterisation, ring-shear tests and analogue experiments. J Struct Geol 28(9):1710–1724. doi:10.1016/j.jsg.2006.05.004

Paquet F, Dauteuil O, Hallot E, Moreau F (2007) Tectonics and magma dynamics coupling in a dyke swarm of Iceland. J Struct Geol 29(9):1477–1493. doi:10.1016/j.jsg.2007.06.001

Phillips WJ (1974) The dynamic emplacement of cone sheets. Tectonophysics 24:69–84

Pinel V, Jaupart C (2000) The effect of Edifice load on magma ascent beneath a volcano. Philos Trans: Math Phys Eng Sci 358(1770):1515–1532

Pinel V, Jaupart C (2004) Magma storage and horizontal dyke injection beneath a volcanic edifice. Earth Planet Sci Lett 221(1–4):245–262

Planke S, Rasmussen T, Rey SS, Myklebust R (2005) Seismic characteristics and distribution of volcanic intrusions and hydrothermal vent complexes in the Vøring and Møre basins. In: Doré AG, Vining BA (eds) Proceedings of 6th Petroleum Geology Conference. Geological Society, London

Pollard DD (1987) Elementary fracture mechanics applied to the structural interpretation of dikes. In: Halls HC, Fahrig WF (eds) Mafic dyke swarms, vol 34. Geological Association of Canada Special Paper, pp 5–24

Pollard DD, Holzhausen G (1979) On the mechanical interaction between a fluid-filled fracture and the Earth's surface. Tectonophysics 53(1–2):27–57

Pollard DD, Johnson AM (1973) Mechanics of growth of some laccolithic intrusions in the Henry Mountains, Utah, II. Bending and failure of overburden layers and sill formation. Tectonophysics 18:311–354

Polteau S, Ferré EC, Planke S, Neumann E-R, Chevallier L (2008a) How are saucer-shaped sills emplaced? Constraints from the Golden Valley Sill, South Africa. J Geophys Res 113

Polteau S, Mazzini A, Galland O, Planke S, Malthe-Sørenssen A (2008b) Saucer-shaped intrusions: occurrences, emplacement and implications. Earth Planet Sci Lett 266(1–2):195–204

Ramberg H (1967) Gravity, deformation and the Earth's crust as studied by centrifuge models. Academic Press, New York

Ramberg H (ed) (1970) Model studies in relation to intrusion of plutonic bodies, vol 2. Mechanism of igneous intrusion, Geol J Spec Iss

Ramberg H (1981) Gravity, deformation and the Earth's crust. Academic Press, New York

Ramos O, Altshuler E, Måløy KJ (2009) Avalanche prediction in a self-organized pile of beads. Phys Rev Lett 102(7):078701

Reber JE, Galland O, Cobbold PR, Carlier Le, de Veslud C (2013) Experimental study of sheath fold development around a weak inclusion in a mechanically layered matrix. Tectonophysics 586:130–144. doi:10.1016/j.tecto.2012.11.013

Reddish DJ, Whittaker BN (1989) Subsidence: occurrence, prediction and control, vol 56. Elsevier, Amsterdam

Richards RJ, Mark R (1966) Gelatin models for photoelastic analysis of gravity structures. Exp Mech 6 (1):30–38. doi:10.1007/bf02327111

Richey JE (1932) The tertiary ring complex of Slieve Gullion (Ireland), with petrological notes by Herbert Henry Thomas. Q J Geol Soc 88(1–4):776–849

Richey JE, Thomas HH, Radley EG, Dixon BE (1930) The geology of Ardnamurchan, North-West Mull and Coll: a description of Sheet 51 and part of sheet 52 of

the Geological Map. Printed under the authority of HM Stationery Office
Rivalta E (2010) Evidence that coupling to magma chambers controls the volume history and velocity of laterally propagating intrusions. J Geophys Res 115 (B7):B07203. doi:10.1029/2009jb006922
Rivalta E, Böttinger M, Dahm T (2005) Buoyancy-driven fracture ascent: experiments in layered gelatine. J Volcanol Geotherm Res 144:273–285
Rivalta E, Dahm T (2006) Acceleration of buoyancy-driven fractures and magmatic dikes beneath the free surface. Geophys J Int 166(3):1424–1439. doi:10.1111/j.1365-246X.2006.02962.x
Rocchi S, Westerman DS, Dini A, Innocenti F, Tonarini S (2002) Two-stage growth of laccoliths at Elba Island, Italy. Geology 30(11):983–986. doi:10.1130/0091-7613(2002)030<0983:tsgola>2.0.co;2
Roche O, Druitt TH (2001) Onset of caldera collapse during ignimbrite eruptions. Earth Planet Sci Lett 191 (3–4):191–202. doi:10.1016/S0012-821X(01)00428-9
Roche O, Druitt TH, Merle O (2000) Experimental study of caldera formation. J Geophys Res: Solid Earth 105 (B1):395–416. doi:10.1029/1999jb900298
Roche O, van Wyk de Vries B, Druitt TH (2001) Sub-surface structures and collapse mechanisms of summit pit craters. J Volcanol Geotherm Res 105(1–2):1–18. doi:10.1016/S0377-0273(00)00248-1
Rodriguez Monreal F, Villar HJ, Baudino R, Delpino D, Zencich S (2009) Modeling an atypical petroleum system: a case study of hydrocarbon generation, migration and accumulation related to igneous intrusions in the Neuquén Basin, Argentina. Mar Pet Geol 26(4):590–605. doi:10.1016/j.marpetgeo.2009.01.005
Román-Berdiel T (1999) Geometry of granite emplacement in the upper crust: contribution of analogue modelling. In: Castro A, Fernández C, Vigneresse JL (eds) Understanding granites: integrating new and classical techniques, vol 174. Geological Society of London,Special Publications, London, pp 77–94
Román-Berdiel T, Gapais D, Brun J-P (1995) Analogue models of laccolith formation. J Struct Geol 17 (9):1337–1346
Román-Berdiel T, Gapais D, Brun JP (1997) Granite intrusion along strike-slip zones in experiment and nature. Am J Sci 297(6):651–678. doi:10.2475/ajs.297.6.651
Rosenau M, Nerlich R, Brune S, Oncken O (2010) Experimental insights into the scaling and variability of local tsunamis triggered by giant subduction megathrust earthquakes. J Geophys Res 115(B9): B09314. doi:10.1029/2009jb007100
Ross PS, White JDL, Zimanowski B, Büttner R (2008a) Multiphase flow above explosion sites in debris-filled volcanic vents: insights from analogue experiments. J Volcanol Geotherm Res 178(1):104–112. doi:10.1016/j.jvolgeores.2008.01.013
Ross PS, White JDL, Zimanowski B, Büttner R (2008b) Rapid injection of particles and gas into non-fluidized granular material, and some volcanological implications. Bull Volcanol 70(10):1151–1168. doi:10.1007/s00445-008-0230-1
Rossello EA, Cobbold PR, Diraison M, Arnaud N (2002) Auca Mahuida (Neuquén basin, Argentina): a quaternary shield volcano on a hydrocarbon-producing substrate. Paper presented at the 5th ISAG, Extended Abstracts, Toulouse
Rossi D, Storti F (2003) New artificial granular materials for analogue laboratory experiments: aluminium and siliceous microspheres. J Struct Geol 25:1893–1899
Rubin AM (1995) Propagation of magma-filled cracks. Annu Rev Earth Planet Sci 23:287–336
Ruch J, Acocella V, Geshi N, Nobile A, Corbi F (2012) Kinematic analysis of vertical collapse on volcanoes using experimental models time series. J Geophys Res: Solid Earth 117(B7):B07301. doi:10.1029/2012jb009229
Ruzicka B, Zaccarelli E (2011) A fresh look at the Laponite phase diagram. Soft Matter 7(4):1268–1286
Rymer H, Wyk Van, de Vries B, Stix J (1998) Pit Crater structure and persistent volcanic activity at Masaya, Nicaragua. Bull Volcanol 59:345–355
Sanford AR (1959) Analytical and experimental study of simple geologic structures. Geol Soc Am Bull 70 (1):19–52. doi:10.1130/0016-7606(1959)70[19:aaesos]2.0.co;2
Scaillet B, Holtz F, Pichavant M (1997) Rheological Properties of Granitic Magmas in Their Crystallization Range. In: Bouchez JL, Hutton DHW, Stephens WE (eds) Granite: from segregation of melt to emplacement Fabrics, vol 8. Petrology and structural geology. Springer, Netherlands, pp 11–29. doi:10.1007/978-94-017-1717-5_2
Schellart WP (2000) Shear test results for cohesion and friction coefficients for different materials: scaling implications for their usage in analogue modelling. Tectonophysics 324:1–16
Schellart WP (2011) Rheology and density of glucose syrup and honey: determining their suitability for usage in analogue and fluid dynamic models of geological processes. J Struct Geol 33(6):1079–1088. doi:10.1016/j.jsg.2011.03.013
Schirnick C, van den Bogaard P, Schmincke H-U (1999) Cone sheet formation and intrusive growth of an oceanic island—yhe Miocene Tejeda complex on Gran Canaria (Canary Islands). Geology 27(3):207–210. doi:10.1130/0091-7613(1999)027<0207:csfaig>2.3.co;2
Schofield N, Stevenson CT, Reston T (2010) Magma fingers and host rock fluidization in the emplacement of sills. Geology 38(1):63–66. doi:10.1130/g30142.1
Schreurs G, Buiter SJH, Boutelier D, Corti G, Costa E, Cruden AR, Daniel JM, Hoth S, Koyi HA, Kukowski N, Lohrmann J, Ravaglia A, Schlische RW, Withjack MO, Yamada Y, Cavozzi C, Del Ventisette C, Brady JAE, Hoffmann-Rothe A, Mengus JM, Montanari D, Nilforoushan F (2006) Analogue benchmarks of shortening and extension experiments. Geol Soc London Spec Pub 253(1):1–27. doi:10.1144/gsl.sp.2006.253.01.01

Schultz RA (1996) Relative scale and the strength and deformability of rock masses. J Struct Geol 18 (9):1139–1149. doi:10.1016/0191-8141(96)00045-4

Schweiger A, Zimmermann I (1999) A new approach for the measurement of the tensile strength of powders. Powder Technol 101(1):7–15. doi:10.1016/S0032-5910(98)00117-X

Sibson RH (2003) Brittle-failure controls on maximum sustainable overpressure in different tectonic regimes. AAPG Bull 87(6):901–908

Sigmundsson F, Hreinsdottir S, Hooper A, Arnadottir T, Pedersen R, Roberts MJ, Oskarsson N, Auriac A, Decriem J, Einarsson P, Geirsson H, Hensch M, Ofeigsson BG, Sturkell E, Sveinbjornsson H, Feigl KL (2010) Intrusion triggering of the 2010 Eyjafjallajökull explosive eruption. Nature 468(7322):426–430. doi:10.1038/nature09558

Smith RL, Bailey RA (1968) Resurgent Cauldrons. Geological Society of America Memoirs 116:613–662. doi:10.1130/MEM116-p613

Sparks RSJ (1988) Petrology and geochemistry of the Loch Ba ring-dyke, Mull (N.W. Scotland): an example of the extreme differentiation of tholeiitic magmas. Contr Mineral and Petrol 100(4):446–461. doi:10.1007/bf00371374

Sparks RSJ, Baker L, Brown RJ, Field M, Schumacher J, Stripp G, Walters A (2006) Dynamical constraints on kimberlite volcanism. J Volcanol Geotherm Res 155 (1–2):18–48. doi:10.1016/j.jvolgeores.2006.02.010

Stix J, Kobayashi T (2008) Magma dynamics and collapse mechanisms during four historic caldera-forming events. J Geophys Res: Solid Earth 113(B9):B09205. doi:10.1029/2007jb005073

Svensen H, Corfu F, Polteau S, Hammer Ø, Planke S (2012) Rapid magma emplacement in the Karoo Large Igneous Province. Earth Planet Sci Lett 325–326:1–9. doi:10.1016/j.epsl.2012.01.015

Svensen H, Jamtveit B, Planke S, Chevallier L (2006) Structure and evolution of hydrothermal vent complexes in the Karoo Basin, South Africa. J Geol Soc London 163:671–682

Svensen H, Planke S, Chevallier L, Malthe-Sorenssen A, Corfu F, Jamtveit B (2007) Hydrothermal venting of greenhouse gases triggering Early Jurassic global warming. Earth Planet Sci Lett 256(3–4):554–566

Svensen H, Planke S, Malthe-Sorenssen A, Jamtvelt B, Myklebust R, Eldem TR, Rey SS (2004) Release of methane from a volcanic basin as a mechanism for initial Eocene global warming. Nature 429 (6991):542–545

Taisne B, Jaupart C (2011) Magma expansion and fragmentation in a propagating dyke. Earth Planet Sci Lett 301(1–2):146–152. doi:10.1016/j.epsl.2010.10.038

Taisne B, Tait S (2009) Eruption versus intrusion? Arrest of propagation of constant volume, buoyant, liquid-filled cracks in an elastic, brittle host. J Geophys Res: Solid Earth 114(B6):B06202. doi:10.1029/2009jb006297

Taisne B, Tait S (2011) Effect of solidification on a propagating dike. J Geophys Res: Solid Earth 116 (B1):B01206. doi:10.1029/2009jb007058

Taisne B, Tait S, Jaupart C (2011) Conditions for the arrest of a vertical propagating dyke. Bull Volcanol 73 (2):191–204. doi:10.1007/s00445-010-0440-1

Takada A (1990) Experimental study on propagation of liquid-filled crack in gelatin: shape and velocity in hydrostatic stress condition. J Geophys Res 95 (B6):8471–8481

Takada A (1994a) Accumulation of magma in space and time by crack interaction. In: Michael PR (ed) International geophysics, vol 57. Academic Press, New York, pp 241–257. doi:10.1016/S0074-6142(09)60099-1

Takada A (1994b) Development of a subvolcanic structure by the interaction of liquid-filled cracks. J Volc Geothermal Res 62:207–224

Takada A (1999) Variations in magma supply and magma partitioning: the role of tectonic settings. J Volcanol Geotherm Res 93(1–2):93–110. doi:10.1016/S0377-0273(99)00082-7

ten Grotenhuis SM, Piazolo S, Pakula T, Passchier CW, Bons PD (2002) Are polymers suitable rock analogs? Tectonophysics 350(1):35–47. doi:10.1016/S0040-1951(02)00080-X

Thomson K (2007) Determining magma flow in sills, dykes and laccoliths and their implications for sill emplacement mechanisms. Bull Volcanol 70(2):183–201

Thomson K, Hutton D (2004) Geometry and growth of sill complexes: insights using 3D seismic from the North Rockall Trough. Bull Volcanol 66(4):364–375

Tibaldi A (1995) Morphology of pyroclastic cones and tectonics. J Geophys Res: Solid Earth 100 (B12):24521–24535. doi:10.1029/95jb02250

Tibaldi A (2005) Volcanism in compressional tectonic settings: is it possible? Geophys Res Lett 32(L06309)

Tibaldi A, Bonali FL, Corazzato C (2014) The diverging volcanic rift system. Tectonophysics 611:94–113. doi:10.1016/j.tecto.2013.11.023

Tibaldi A, Pasquarè F, Tormey D (2010) Volcanism in Reverse and Strike-Slip Fault Settings. In: Cloetingh S, Negendank J (eds) New frontiers in integrated solid earth sciences. Springer, Netherlands, pp 315–348. doi:10.1007/978-90-481-2737-5_9

Trippanera D, Acocella V, Ruch J (2014) Dike-induced contraction along oceanic and continental divergent plate boundaries. Geophys Res Lett GL061570. doi:10.1002/2014gl061570

Troll VR, Walter TR, Schmincke HU (2002) Cyclic caldera collapse: piston or piecemeal subsidence? Field and experimental evidence. Geology 30(2):135–138

Trude J, Cartwright J, Davies RJ, Smallwood J (2003) New technique for dating igneous sills. Geology 31 (9):813–816

Turcotte DL, Schubert G (2002) Geodynamics –, 2nd edn. Cambridge Unversity Press, Cambridge

van Wyk de Vries B, Marques A, Herrera R, Granjas JL, llanes P, Delcamp (2014) Craters of elevation revisited: forced folds, bulges and uplift of volcanoes (2014) Bull Volcanol. doi:10.1007/s00445-014-0875-x

Verbeek R (1884) The Krakatoa eruption. Nature 30:10–15

Walker GL, Skelhorn RR (1966) Some associations of acid and basic igneous rocks. Earth-Sci Rev 2:93–109. doi:10.1016/0012-8252(66)90024-9

Walker GPL (1999) Volcanic rift zones and their intrusion swarms. J Volcanol Geotherm Res 94(1–4):21–34

Walter TR, Troll VR (2001) Formation of caldera periphery faults: an experimental study. Bull Volcanol 63:191–203

Walter TR, Troll VR (2003) Experiments on rift zone evolution in unstable volcanic edifices. J Volcanol Geotherm Res 127(1–2):107–120

Walters AL, Phillips JC, Brown RJ, Field M, Gernon T, Stripp G, Sparks RSJ (2006) The role of fluidisation in the formation of volcaniclastic kimberlite: grain size observations and experimental investigation. J Volcanol Geotherm Res 155(1–2):119–137. doi:10.1016/j.jvolgeores.2006.02.005

Watanabe T, Masuyama T, Nagaoka N, Tahara T (2002) Analog experiments on magma-filled cracks: competition between external stresses and internal pressure. Earth Planets Space 54:1247–1261

Weijermars R (1986) Flow behaviour and physical chemistry of bouncing putties and related polymers in view of tectonic laboratory applications. Tectonophysics 124(3–4):325–358. doi:10.1016/0040-1951(86)90208-8

Westerman DS, Dini A, Innocenti F, Rocchi S (2004) Rise and fall of a nested Christmas-tree laccolith complex, Elba Island, Italy. Geol Soc London Spec Pub 234 (1):195–213. doi:10.1144/gsl.sp.2004.234.01.12

White DJ, Take WA, Bolton MD (2003) Soil deformation measurement using particle image velocimetry (PIV) and photogrammetry. Géotechnique 53 (7):619–631. doi:10.1680/geot.2003.53.7.619

White JDL, Ross PS (2011) Maar-diatreme volcanoes: a review. J Volcanol Geotherm Res 201(1–4):1–29. doi:10.1016/j.jvolgeores.2011.01.010

White RS, Drew J, Martens HR, Key J, Soosalu H, Jakobsdóttir SS (2011) Dynamics of dyke intrusion in the mid-crust of Iceland. Earth Planet Sci Lett 304(3–4):300–312. doi:10.1016/j.epsl.2011.02.038

Williams H (1941) Calderas and their origin 25:239-346

Wilson CJN, Hildreth W (1997) The Bishop Tuff: new insights from eruptive stratigraphy. J Geol 105 (4):407–440

Witte J, Bonora M, Carbone C, Oncken O (2012) Fracture evolution in oil-producing sills of the Rio Grande Valley, northern Neuquén Basin, Argentina. AAPG Bull 96(7):1253–1277. doi:10.1306/10181110152

Woolsey TS, McCallum ME, Schumm SA (1975) Modeling of diatreme emplacement by fluidization. Phys Chem Earth 9:29–42

Wright TJ, Ebinger C, Biggs J, Ayele A, Yirgu G, Keir D, Stork A (2006) Magma-maintained rift segmentation at continental rupture in the 2005 Afar dyking episode. Nature 442(7100):291–294. doi:10.1038/nature04978

Závada P, Dedecek P, Mach K, Lexa O, Potuzák M (2011) Emplacement dynamics of phonolite magma into maar-diatreme structures—correlation of field, thermal modeling and AMS analogue modeling data. J Volcanol Geotherm Res 201(1–4):210–226

Závada P, Kratinová Z, Kusbach V, Hrouda F (2006) Analogue modeling of AMS development during emplacement of shallow level volcanic bodies (Extrusive Domes and Laccoliths). Geolines 206(5):136–137

Závada P, Kratinová Z, Kusbach V, Schulmann K (2009) Internal fabric development in complex lava domes. Tectonophysics 466(1–2):101–113. doi:10.1016/j.tecto.2008.07.005